

Diss. ETH Nr. 14353

**Electro-Optic Effects and Their Application in Indium
Phosphide Waveguide Devices for Fibre Optic Access
Networks**

A dissertation submitted to the
Swiss Federal Institute of Technology Zürich
for the degree of
Doctor of Natural Sciences

submitted by

GERHARD HAGN
Dipl. Phys. ETH
born 07. February 1971
in Feldkirch (Vorarlberg), Austria

accepted on the recommendation of

Prof. Dr. H. Melchior, examiner
Prof. Dr. P. Günter, co-examiner

2001

CONTENTS

<i>Abstract</i>	iii
<i>Zusammenfassung</i>	v
1. Introduction	1
1.1 History and state of the art of modern telecommunications	2
1.2 Motivation and goals of this thesis	3
2. Electro-optical switching	7
2.1 Concepts of optical switches	8
2.1.1 Applications of optical space switches	8
2.1.2 Layout of optical space switches	9
2.2 Structure and layout of the electro-optic switches implemented	12
2.3 Optical ridge waveguides	13
2.4 Electric field in a reverse biased p-i-n double-heterojunction waveguide	17
2.5 Electro-optic effects in InP/InGaAsP	18
2.5.1 Phase shift change in a p-i-n double heterojunction waveguide	21
3. Electro-optic Effects	23
3.1 Introduction	24
3.2 Model of the carrier effect	24
3.3 Model of the Pockels effect	27
3.4 Model of the Franz Keldysh effect	30
3.4.1 The imaginary part of the dielectric constant	31
3.4.2 The real part of the dielectric constant	35
3.5 Electro-optic effects in waveguides on (100) InP	39
3.5.1 Pockels Effect in (100) InGaAsP/InP	39

3.5.2	Franz–Keldysh Effect in (100) InGaAsP/InP	39
4.	<i>Measurement of the electro–optical Effects</i>	41
4.1	Introduction	42
4.1.1	The refractive and the absorption index	42
4.2	Measurement of the field dependency of the absorption index	45
4.3	Measurement of the field dependency of the refractive index	48
4.3.1	Pockels effect	48
4.3.2	Franz–Keldysh and carrier effect	51
4.4	Discussion	54
4.5	Summary and Conclusion	55
5.	<i>Design and Layout of a transceiver chip for passive optical networks</i>	59
5.1	Introduction	60
5.1.1	Optical Networks	60
5.1.2	Passive optical networks (PONs)	61
5.1.3	Terminal equipment in passive optical networks	62
5.2	Concept and design of the transceiver chip	64
5.2.1	Ridge waveguides and electro–optic modulators	65
5.2.2	Optical mode size adapters	67
5.2.3	Optical 3dB power splitters	68
5.2.4	Optical 1:9 power splitters	70
5.2.5	Waveguide photodetectors	72
5.3	Fabrication process sequence	73
5.3.1	Definition of the layer structure	73
5.3.2	Structuring of the waveguides	76
5.3.3	Photodetectors	80
5.3.4	Passivation, final metallisation and coatings	80
5.4	Experimental results	82
5.4.1	Photodetector	82
5.4.2	Modulator	83
5.5	Conclusion	86
6.	<i>Summary and Outlook</i>	89
6.1	Summary	89
6.2	Outlook	90
	<i>Bibliography</i>	92

ABSTRACT

Integrated electro-optic space switches are key components in modern telecommunication systems. They are required to route data packets to their destination or modulate information onto an optical carrier. Mach-Zehnder type space switches, based on the InP/InGaAsP material system and using reverse biased pin-diodes as phase shifters, allow polarisation insensitive operation, very high switching speeds and low losses.

In order to optimise electro-optical space switches it is necessary to understand the electro optical effects involved. Electro-optic space switches are very well suited to determine the electro-optic effects very accurately by measuring the optical response to an applied electric field.

In this thesis the electro-optical effects, caused by the electric field in a reversed biased p-i-n diode, realised in quaternary InGaAsP lattice matched to (100) InP substrates, are analysed. Furthermore the integrability of space switches with photodetectors and mode-size adapters is demonstrated.

The main effects occurring in the field of a reverse biased p-i-n diode are the Pockels effect, the Franz-Keldysh effect and the "free carrier" effect. Models of these effects are presented.

As a contribution to the physics of the Franz-Keldysh effect it was possible to determine the coefficients R_{11} and R_{12} in InGaAsP for the first time. For an energy detuning of 154 meV R_{11} and R_{12} were found to be $18 \cdot 10^{-20} \frac{m^2}{V^2}$ and $12 \cdot 10^{-20} \frac{m^2}{V^2}$ respectively. The Franz-Keldysh effect depends only on the polarisation while the Pockels effect depends on polarisation and crystal orientation.

To determine the contribution of the Franz Keldysh, Pockels and free carrier effects to the refractive index change experimentally. A chip featuring switches under different angles φ with respect to the $[0\bar{1}1]$ cleavage plane was manufactured. The refractive index change caused by the electric field $\Delta n(E)$ and the related absorption $\Delta\alpha(E)$ was measured and the different electro

optical effects isolated and analysed as a function of the wavelength, state of polarisation and direction to the crystallographic axes. The contribution of the electro-optic effects to the refractive index change agrees well with the theoretical predictions.

As a demonstration of the useful combination of these switches with other functions, the feasibility of monolithic integration of switches based on the effects mentioned above, mode size adapters and photodetectors was demonstrated. As an example for practical applications a transceiver chip intended for use in subscriber terminals of passive optical access networks has been manufactured. Due to the monolithic integration of a photodetector for the reception of downstream data, a reflective Mach-Zehnder interferometric switch for transmitting upstream data and beam splitters to separate the up- and downstream data were monolithically integrated into a single chip, only a single expensive fibre to chip interface is necessary. Furthermore mode size adapters were integrated to reduce fibre to chip coupling losses and to ease alignment tolerances. A special process had to be developed to manufacture the mode size adapters all over the wafer with sufficient homogeneity.

Experimental results show fibre to fibre losses as low as 8dB. The modulator is capable of an on-off ratio of 15dB over a optical wavelength range of 30nm and a bandwidth of several hundred megabits per second.

ZUSAMMENFASSUNG

Integrierte elektro-optische Raumschalter sind Schlüsselkomponenten in modernen Telekommunikationssystemen. Sie werden benötigt um Datenpakete zu ihrem Ziel zu leiten oder um Information auf einen optisch Träger aufzomodulieren. Mach-Zehnder Raumschalter, in denen rückwärtsgespannte pin-Dioden als Phasenschieber verwendet werden, und die auf dem InP / InGaAsP Materialsystem basieren, können polarisationsunabhängig betrieben werden, erreichen sehr schnelle Schaltgeschwindigkeiten und weisen niedere optische Verluste auf.

Um elektro-optische Raumschalter optimieren zu können ist ein gutes Verständnis der beteiligten elektro-optischen Effekte unbedingt notwendig. Elektro-optische Raumschalter eignen sich auch sehr gut zur Bestimmung der elektro-optischen Effekte, indem man die optische Antwort auf ein angelegtes elektrisches Feld misst.

In dieser Arbeit elektro-optische Effekte untersucht, die von einem elektrischen Feld einer rückwärtsgespannten pin-Diode hervorgerufen worden sind. Die pin-Diode basiert auf an (100) InP Substraten gitterangepassten InGaAsP. Ausserdem wird die Integrierbarkeit von Raumschaltern mit Photodetektoren und Modenadaptern demonstriert

Die wichtigsten Effekte, die im elektrischen Feld einer rückwärtsgespannten pin-Diode auftreten, sind der Pockels Effekt, der Franz-Keldysh Effekt und der „Freie Ladungsträger“ Effekt. Modelle dieser Effekte werden in dieser Arbeit vorgestellt.

Als Beitrag zur Physik des Franz-Keldysh Effekts konnten die Koeffizienten R_{11} und R_{12} zum ersten mal in InGaAsP bestimmt werden. Bei einem Energieabstand der Photonenenergie zur Bandlücke von 154 meV beträgt der Wert für R_{11} $18 \cdot 10^{-20} \frac{\text{m}^2}{\text{V}^2}$ und für R_{12} $12 \cdot 10^{-20} \frac{\text{m}^2}{\text{V}^2}$. Der Franz-Keldysh Effekt hängt in der (100) Ebene von InP/InGaAsP nur von der Polarisation ab. Der Pockels Effekt hingegen hängt von der Polarisation und der Kristallorientierung ab.

Um die Beiträge des Franz-Keldysh, Pockels und Ladungsträgereffekts zu der Änderung des Brechungsindex experimentell zu bestimmen wurde ein Chip hergestellt, auf dem Schalter deren Elektroden verschiedene Winkel φ bezüglich der $[0\bar{1}1]$ Ebene angeordnet worden sind. Die durch ein angelegtes elektrisches Feld verursachte Brechungsindexänderung $\Delta n(E)$ und die Änderung des Absorptionsindex $\Delta\alpha(E)$ wurden gemessen, die verschiedenen elektro-optischen Effekte isoliert und deren Abhängigkeit von der Wellenlänge, Polarisation und Richtung zu den Kristallachsen bestimmt. Die experimentell gewonnenen Daten stimmen gut mit den theoretischen Voraussagen überein. Die beobachtete Änderung des Absorptionsindex $\Delta\alpha(E)$ ist um etwa 3 Größenordnungen grösser als vom Modell für das Franz-Keldysheffekt vorausgesagt. Diese Diskrepanz kann jedoch aufgelöst werden, indem man zu dem Modell freie Ladungsträger mit der effektiven Masse von freien Elektronen hinzufügt.

Um zu zeigen, dass diese Schalter auch mit anderen Elementen sinnvoll kombiniert werden können, wurde die Machbarkeit der monolithischen Integration von Schaltern, die auf den oben beschriebenen Effekten basieren, Modeadaptern und Photodetektoren demonstriert. Als praktisches Anwendungsbeispiel wurde ein ein Sende- und Empfangsbauteil hergestellt, das für den Einsatz in einem Endgerät eines passiv optischen Netzwerks konzipiert worden ist. Dank der monolithischen Integration von einer Photodiode zum Empfangen von gesendeten Information, ein reflektiver Mach-Zehnder interferometrischer Schalter um Daten senden zu können und Strahlteiler zur Trennung von empfangenen und zu sendenden Daten, auf einem Chip konnte die Anzahl teurer Faser zu Chip Übergänge auf eine einzige reduziert werden. Weiter wurden Konverter für die optischen Moden integriert um die Faser Chip Verluste gering zu halten und die Justiertoleranzen zu vergrössern. Ein spezieller Prozess musste entwickelt werden, um die optischen Moden Konverter mit ausreichender Homogenität an beliebigen Stellen des Wafers herstellen zu können.

Messungen an den fertigen Bauteilen ergeben einen Faser zu Faser Verlust von nur 8 dB, unabhängig von der Polarisation des Lichtes mit einem Ein/Aus Verhältnis von 15dB über eine optisches Fenster von über 30 nm Breite. Der Modulator kann mit mehreren hundert Megabit pro Sekunde betrieben werden. Die integrierte Photodiode ist in der Lage, mit Datenraten von mehreren Gigabit pro Sekunde umzugehen.

1. INTRODUCTION

To show the significance of electro-optical switches in modern fibre-optical telecommunication systems a short overview over the history and future of telecommunications is given. Key components in fibre-optical communication systems are electro-optical switches. Electro-optical switches are needed to route the optical data-streams to their destination. They are also used for time division multiplexing and to modulate information onto a carrier. It is pointed out that electro-optical space switches can also be used to analyse electro-optical effects very accurately. Finally the motivation and layout of this thesis is outlined.

1.1 *History and state of the art of modern telecommunications*

In our time, telecommunication is a field experiencing increasingly rapid growth. More and more people and companies discover the possibilities of the network called "Internet". The rapid increase of users and growing number of services is leading to a seemingly unsatisfiable demand for more bandwidth.

The cornerstone of today's telecommunication system was laid in 1876 by Alexander Graham Bell by patenting the telephone. After only two years the first manual switchboard was in operation serving 21 subscribers. In 1880 Alexander Graham Bell, who was a little ahead of his time, demonstrated the first optical voice transmission through 200m of atmosphere [1]. His "photophone" modulated the sunlight with a diaphragm and therefore worked only on sunny days. As the telephone network spread all over the globe, the manual switchboards were replaced by automatic switchboards using electro-mechanical relays. Later in the 1970s these in turn were supplemented by electronic switches. During this period the analog voice transmission was replaced by digital signal transmission.

A major breakthrough in data transmission started with the use of optical fibres. A key development was initiated in 1958 by Shawlow and Townes who proposed a coherent light source based on the principle of stimulated emission [2]. Soon afterwards in 1960 a ruby laser was demonstrated [3] and in 1962 the first semiconductor lasers were realized [4, 5]. Semiconductor lasers capable of continuous operation at 1.3 μm and 1.55 μm became available in 1977 [6] and 1979 [7, 8] respectively.

In the beginning optical fibres lost about 5000 dB/km [9] but were improved by a concentrated effort between 1966 and 1970. The breakthrough was the reduction of the losses to 20 dB/km [10]. Whereas a modern optical fibre loses as little as 0.2 db/km with a dispersion of 15 ps/(km nm) at a wavelength of 1.55 μm [11], or 0.35 db/km with vanishing dispersion at 1.3 μm and is capable of a bandwidth of several Terrabits/s [12], a coaxial cable losses 2.5 db/km at 1 MHz and 50 dB/km at 1 GHz. This development increased the capacity from one channel per fibre to several thousand.

Motivated by the advantages of optical fibres over copper wires commercial transmission systems were installed. The first one according to my knowledge was installed 1976 in Chicago and bridged 2.5 km with a bandwidth of 44.7 MBits/s. The first undersea link Optician-1 was deployed on the Canary Islands in 1986 [13] followed by "Transatlantic Lightwave System" TAT-8 in 1988 [14] providing a bandwidth of 275 MBits/s across a distance of 6687 km.

High performance optical links evolve rapidly between the major nodes. In contrast to this wide area networks (WANs) the metropolitan (MANs) and local area networks (LANs) are only now starting to become optical. The "last mile" to the subscriber remains a major bottleneck. Most network users are still connected to the net with analog modems capable of only 56 kBit/s at best. Even ISDN users are not much better off. Only recently an effort is being made in major population centres to utilise the coaxial cables of radio and TV distributors to provide a data channel with a bandwidth of a few megabit among a number of subscribers. Currently solutions are being developed to provide cost effective fibre optical links to subscribers [15, 16].

1.2 Motivation and goals of this thesis

Integrated electro-optic space switches are devices which allow an optical signal to be switched from one of m inputs to one of n output waveguides by applying electric fields or currents. They are key components in fibre optic communication systems. They are used as routers, packet switches and modulators. A good understanding of the electro-optical effects occurring in the phase shifters of a Mach-Zehnder type modulator is necessary to optimise its performance characteristics. The Franz-Keldysh and the Pockels effect are of special interest because they contribute most to the total electro-optic effect.

Aside from their importance in fibre-optic telecommunication systems, integrated electro-optic space switches are very well suited to measure electro-optic effects accurately. Using reverse biased pin-diodes allow the application of electric fields as high as several 10^7 $[\frac{V}{m}]$. By measuring the optical response of the switch the phase shifts in the arms of the Mach-Zehnder interferometers and thereby the refractive index change can be determined accurately. This makes electro-optic space switches ideal for the analysis of electro-optic effects.

Usually several optical and electro-optical components are needed in the terminal equipment at the end of optical fibres. The fibre to chip interfaces are expensive, due to the stringent alignment tolerances. To lower the cost of the optical communication systems it is necessary to reduce the number of fibre to chip interfaces by integrating more components into a single chip. If optical fibres are to replace the copper wire comparatively low prices for terminal equipment are necessary to become affordable to the broad public.

The main goal of this thesis is to obtain a detailed understanding of the

electro-optical effects occurring in a reverse biased InP/InGaAsP heterojunction from a detailed experimental analysis. The effects of interest are the Pockels effect, the Franz-Keldysh effect and the “free carrier” effect. From the experimental data, the behaviour of these effects with respect to their dependence on the polarisation, crystal orientation and photon to bandgap energy difference is to be modelled. Furthermore the dependency of the absorption index on the applied electric field, optical polarisation and photon to bandgap energy has to be derived to allow the optimisation of electro-optic switches. Finally the feasibility of the monolithic integration of multiple electro-optical components is to be demonstrated.

Outline of this thesis

This thesis has been sectioned as follows:

Chapter 2 gives an overview over the basic principles and physics relevant for understanding electro-optical switches. After a short introduction into different switch types the principles of Mach-Zehnder interferometers are outlined. Furthermore the physics of waveguides and pin-diodes are explained. Finally a detailed description of the properties of electro optic effects in crystals are outlined.

Chapter 3 focuses on the physical principles responsible for the electro-optic effects occurring in the depletion zone of reverse biased double-hetero InP/InGaAsP pin-diodes. First theoretical models of the carrier and Pockels effect are presented. These effects can be well described using classical harmonic oscillator models. Subsequently a quantum mechanical model of the Franz-Keldysh effect is presented. The Franz Keldysh is a photon assisted interband tunnelling effect.

Chapter 4 presents the characteristics of the electro-optical effects which are determined for both polarisations over a wide optical wavelength range and compared to the predictions of the physical models.

Chapter 5 demonstrates the feasibility of the monolithic integration of different electro-optic components into a single chip. A transceiver chip intended for the use in passive fibre optic access networks is presented. A detailed description of the design and manufacturing process of a transceiver chip is given. The transceiver chip features monolithically integrated waveguides, optical mode shape adapters, photodetectors and

reflective electro-optical Mach-Zehnder type modulators. Finally the performance characteristics of the transceiver chip are presented.

Chapter 6 summarizes the achievements of this thesis and gives an outlook into the possible future enhancements.

2. ELECTRO-OPTICAL SWITCHING

This chapter gives a detailed description of the principles and the physics of integrated InP/InGaAsP based electro-optic space switches. After an overview of different switch types a short introduction into the basics of integrated optical waveguides is given. Then the dependency of the electric field in a reverse biased pin-diode on the applied voltage is discussed. Finally the properties of the linear and the quadratic electro-optic effects in crystals are analysed.

2.1 Concepts of optical switches

The properties of optical switches depend on their principle of operation, physical effects involved, the material system and technology of their implementation, and on their architecture. As it is generally not possible to optimise all parameters of a switch simultaneously [17]. It is necessary to choose the technology and architecture to obtain switches meeting the requirements imposed by their specific applications.

Properties to be considered are the number of input/output ports, operational wavelength, fibre-to-fibre loss, polarisation sensitivity, crosstalk, switching speed/reconfiguration times, cost effectiveness, size, power consumption, high bit rate transparency and stability for applications.

2.1.1 Applications of optical space switches

Protection switches are used to reroute data streams in case of failure of an optical fibre link. As these switches are only seldom operated, switching speeds can be very low. Protection switches are rarely cascaded. Therefore the requirements regarding insertion loss and cross-talk are somewhat relaxed. The switches should however consume as little power as possible in their non active states.

Applications such as telephony, video conferences, etc. require a dedicated channel or route connecting two sites. Depending on the service connecting switching times up to some hundred milliseconds are acceptable. This type of switching is called *circuit switching*. Circuit switches usually need a high number of input/output ports, they are cascaded and experience a wide range of signal strengths at their input ports the requirements concerning insertion loss and crosstalk are stringent.

On high performance major trunk lines the information is usually sent in a stream of packets transmitted as demand requires. Each package consists of a destination address and a block of data transmitted with bit rates between 155Mbits/s and 40Gbits/s. This technique allows interleaving of data streams even if the data rates are different. At the nodes of such a backbone the address is decoded and the packet routed accordingly. This type of transmission is generally referred to as *packet switching*. To avoid a waste of bandwidth the switching process has to be fast i.e.: the switching times have to be in the nanosecond range or shorter.

A method to increase the bandwidth of a fibre is interleaving multiple data

streams called “time division multiplexing” (TDM). This type of transmission requires very fast switches to add and extract the individual data streams.

2.1.2 Layout of optical space switches

A short overview of the different types of optical switches is given below to motivate the choice of Mach-Zehnder type switches based on the InP/InGaAsP material system.

Mechanical optical switches achieve switching by rearranging or displacing optical fibres. The characteristics of the switches are determined by the properties of the fibres themselves. Thus the optical loss, crosstalk, polarisation and wavelength dependence are very low. The switching speed however is in the range of seconds to minutes. This makes them the suitable choice for protection and fibre-route switching functions. The largest mechanical optical fibre switching array to my knowledge is a 512×512 strictly nonblocking optical fibre matrix [18].

Mach-Zehnder Interferometer (MZI) (see figure 2.1(a)) type switches consist of a beam-splitter and combiner interconnected by two phase shifters. The incoming light is first split in the beam splitter. It then passes through a pair of phase shifters. In the combiner the light of the two arms interferes and the resulting light is coupled into the output waveguide. Switching is accomplished by changing the refractive index in one of the phase-shifters. The resulting change of the phase between the two interfering optical modes directly changes the resulting light intensity. This configuration requires only small refractive index changes for switching and allows independent optimisation of beam splitters/combiners and phase shifters. However, these devices are quite large and show a sinusoidal response.

Directional couplers (see figure 2.1(b)) basically consist of two closely spaced waveguides. The light couples between these two waveguides. Refractive index changes in these waveguides change the coupling length i.e. the length of the waveguides required for coupling the light from one waveguide into the other. The strong dependency of the coupling length on the optical wavelength, polarisation and switch geometry and on fabrication tolerances is a major drawback.

In contrast to interference based Mach-Zehnder type switches and directional couplers, *Digital Optical Switches (DOS)* (see figure 2.1(c)) exploit the property of light to couple into the region of the highest refractive index. The optical mode of the input-waveguide is adiabatically expanded and guided

Seite Leer /
Blank leaf

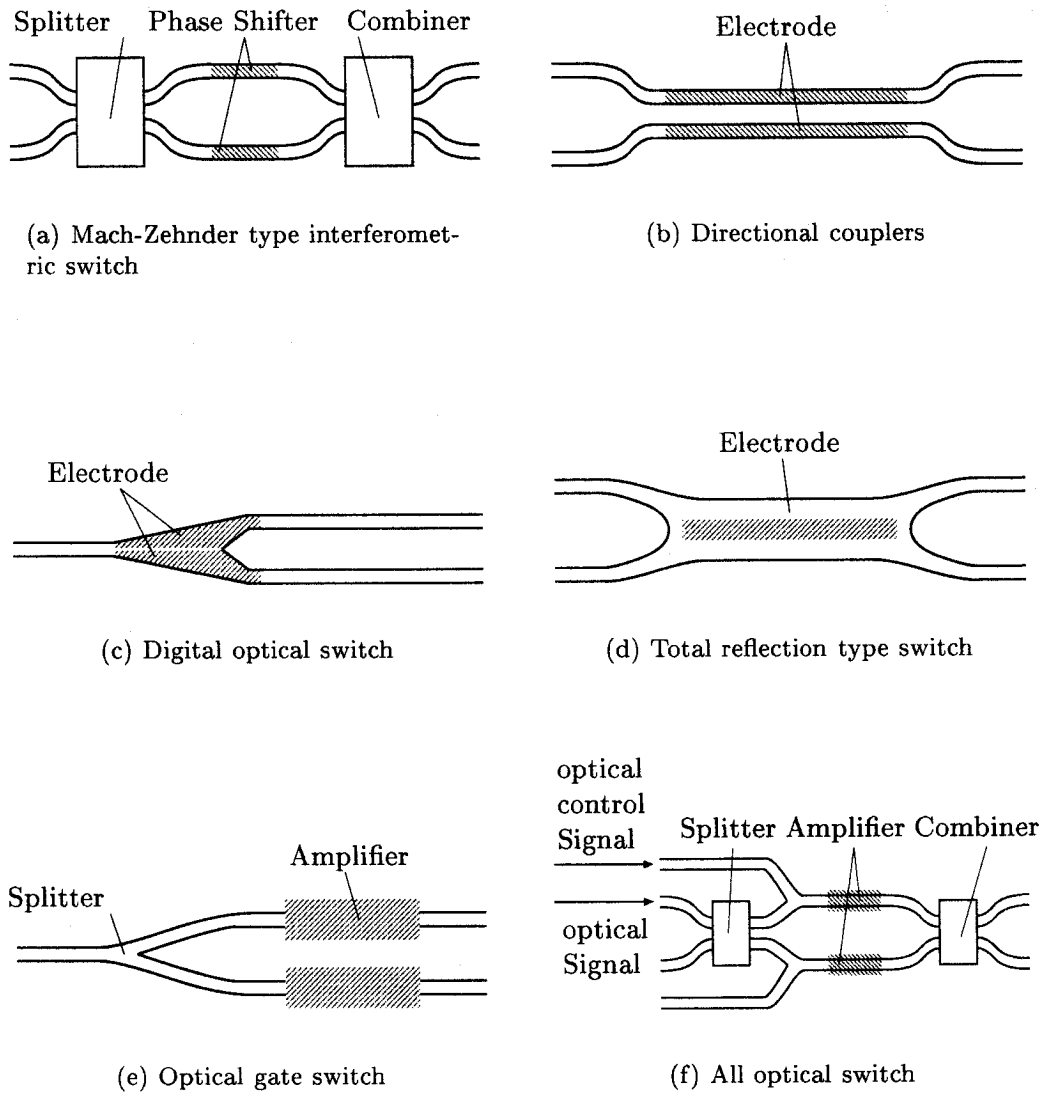


Fig. 2.1: Architectures of optical space switches

towards a Y-branch. Therefore the light leaves the switch in the branch with the higher refractive index. These switches can easily be made polarisation insensitive. However much higher refractive index changes are required than in interference type switches. Also high fabrication tolerances are required, especially in the Y-Branch region of the switch.

Total Internal Reflection (TIR) type switches consist a free space coupler and of two input and two output waveguides in a crossed configuration at the corners of the free space coupler (see figure 2.1(d)). In the non active state of a TIR the light of an input waveguide propagates through the free space coupler to the opposite output waveguide. If the refractive index in the middle of the free space coupler is lowered, the light of the input waveguides is reflected at the region of lower refractive index and thereby switched to the other output waveguide. Total internal reflection switches and digital optical switches share the same advantages and disadvantages. The light is switched between the output waveguides by changing the refractive index in one half of the switching section and thereby changing the critical angle of total internal reflection.

Optical gate switches (see figure 2.1(e)) are based on gain / absorption switching. The incoming light is split into several branches. Each branch features an optical amplifier. Switching is achieved by pumping the amplifier of the corresponding branch. As unpowered amplifiers are good absorbers, high on off ratios are possible. These type of switches allow for low losses or even gain [19, 20]. Noise accumulation and signal distortion, caused by gain saturation effects if the input power is too high, may be a problem. Additionally there is an inter-wavelength crosstalk has to be anticipated in systems using more than one wavelength.

All optical switches (see figure 2.1(f)) are based on Mach-Zehnder interferometric switches. Instead of phase shifters they feature SOAs with input ports for optical control signals. The intensity of the incoming signal and the bias current of the SOAs are selected such that the SOAs are almost saturated. Under these conditions a control signal changes the gain in the SOA and thereby the refractive index. This way the SOAs act as optically controlled phase shifters of a conventional Mach-Zehnder interferometer. All optical switches are capable of switching times in the picosecond range provided that the control pulses are short enough. Thus they are well suited for time division multiplexing applications or add-drop switches. 80 to 10 GBits/s (de)multiplexing has been demonstrated. All optical switches can also be used as wavelength converters. The inherent dependency of these

switches on the intensity of the input signals makes their application in fibre optical networks difficult. In addition measures are required to keep the generally unwanted control signals out of the communication system. Also simultaneous switching of multiple wavelengths is very difficult if not impossible, due the high inter wavelength crosstalk and the wavelength dependency of the gain in an SOA.

The overview given above clearly shows that it is not possible to manufacture switches with ideal characteristics. It clearly indicates that the appropriate switching technology has to be selected according to the application and compromises have to be made.

2.2 Structure and layout of the electro-optic switches implemented

The switches implemented in this thesis are based on a InGaAsP/InP double hetero structure, grown on (100) InP substrates. Due to its higher refractive index the InGaAsP layer is the guiding optical layer. The (100) InP substrates were preferred over (111) InP substrates because they are easily available, and most processing technology is developed for (100) substrates.

The use of (111) substrates would have required the development of a completely new technology. Also it is impossible to cleave vertical optical facets from (111) substrates.

The switches themselves are Mach-Zehnder interferometer (MZI) type switches (figure 2.1(a)) as proposed and realised by Bachmann et al. [21] with multi-mode interference couplers as beam splitters and combiners [22]. The incident light is split in two parts (I_1 and I_2) which follow independent optical paths and are merged again in a combiner where they interfere with each other, provided that the optical path difference is smaller than coherence length of the light. Multi-mode interference couplers were chosen as beam splitters and combiners because they are almost polarisation independent and work over a wavelength range of several ten nanometers and their ease of fabrication. The resulting output power depends on their relative phases $\Delta\varphi$. Taking phase-shifts caused by the MMIs [23] onto account the resulting light intensities at the bar- and cross-output ports are given by

$$I_{Out-cross} = \frac{1}{2} \left(I_1 + I_2 + \sqrt{I_1 \cdot I_2} \cdot \cos(\Delta\varphi) \right) \quad (2.1)$$

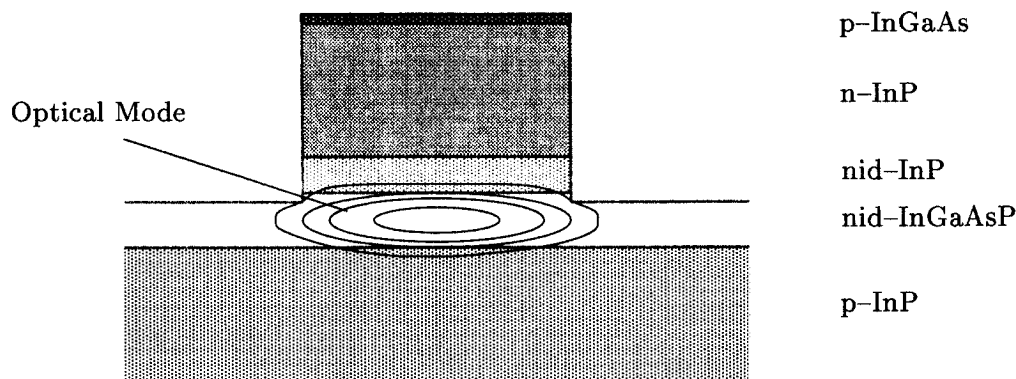


Fig. 2.2: Cross-section through the ridge waveguide

$$I_{Out-bar} = \frac{1}{2} \left(I_1 + I_2 + \sqrt{I_1 \cdot I_2} \cdot \cos(\Delta\varphi + \pi) \right) \quad (2.2)$$

The phase-shift $\Delta\varphi$ is the consequence of a refractive index change Δn in an arm of the Mach-Zehnder interferometer. The quantities $\Delta\varphi$ and Δn are linked by

$$\Delta\varphi = \frac{2\pi}{\lambda} \cdot \Delta n \cdot l \quad (2.3)$$

where λ denotes the optical wavelength in vacuum and l the length of the phase-shifter.

The Mach-Zehnder interferometer was implemented utilising a pin doped double-heterojunction ridge waveguide structure (see figure 2.2) owing to its ease of fabrication and potential to obtain high refractive index changes with low voltages. The refractive index change Δn is generated by the Pockels- and Franz-Keldysh effect caused by the electric field in the intrinsic region of the reverse biased p-i-n diode. The thicknesses of the layers have been chosen to maximise the electrical fields in the light conducting layer. This maximises the refractive index change while keeping the optical losses low.

2.3 Optical ridge waveguides

Optical waveguides are fundamental components for the realisation of integrated electro-optic components. Rib waveguides are usually the preferred choice due to the ease of fabrication. The theory and simulation of waveguides

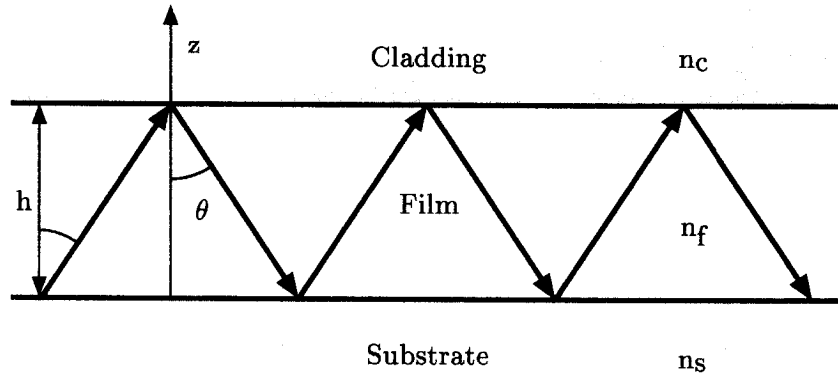


Fig. 2.3: Side view of a slab waveguide showing the zig-zag propagation of the lightwave of a guided mode according to the ray-optic model

has been described comprehensively in several textbooks [24, 25]. Therefore only a short description of their principles of operation, necessary for the understanding of the following sections is given.

The principle of operation of a waveguide can be explained by a simple ray-optical model. For simplicity reasons a two-dimensional model of a slab waveguide is used. A planar waveguide consists of a layer (film) of higher refractive index n_f sandwiched between two materials of lower refractive index, usually referred to as substrate and cladding. The guiding of light in the layer of higher refractive index is based on the effect of total reflection, occurring when light hits an interface to a medium of lower refractive index under a shallow enough angle. Thus the interfaces between film and cover or substrate can act as mirrors trapping light inside the film. The light inside the film propagated in a zig-zag fashion as depicted in 2.3.

The dimensions of the film in integrated-optic devices are of the same order as the wavelength of the conducted light. Therefore the wave properties of light have to be taken into account. This is done by replacing the picture of light travelling in a zig-zag fashion by two superimposed uniform plane waves. These waves are monochromatic and coherent, with a vacuum wavelength λ and a wavevector \vec{k} . The zig-zag picture predicts an effective phase velocity

$$v_p = \frac{c}{n_f} \sin \theta \quad (2.4)$$

By using the definition of the refractive index, the effective refractive index n_{eff} is therefore

$$n_{eff} = n_f \sin \theta \quad (2.5)$$

The effective refractive index n_{eff} is limited by the refractive index of the film and substrate, i.e. $n_s < n_{eff} < n_f$.

However only a discrete set of angles θ leading to a self consistent image is allowed. For self consistency the total phase shifts occurring when the wave moves from one boundary to the other and back again has to be a multiple of 2π . For a film thickness of h we have a phase shift of $2\pi \cdot 2 \frac{n_f}{\lambda} \cos \theta$ for the passage through the film and the phase shifts $2\phi_s$ and $2\phi_c$ from the reflections on the film-substrate and film-cover boundaries which also depend on the angle θ . So the condition

$$2\pi \cdot 2 \frac{n_f h}{\lambda} \cos \theta + 2\phi_s + 2\phi_c = 2\nu\pi \quad (2.6)$$

where the mode number ν is an integer, has to be fulfilled for a guided mode. Due to its complexity equation (2.6) can only be solved numerically. In order to make this calculations more broadly applicable a normalised film thickness

$$V = \frac{2\pi}{\lambda} h \sqrt{n_f^2 - n_s^2} \quad (2.7)$$

and a normalised guide index

$$b = \frac{n_{eff}^2 - n_s^2}{n_f^2 - n_s^2} \quad (2.8)$$

have been introduced. The normalised guide index b can range between 0 ($n_{eff} = n_s$) and 1 ($n_{eff} = n_f$). If the refractive index difference between film and substrate is small equation (2.8) can be rewritten to

$$n_{eff} = n_s + b \cdot (n_f - n_s) \quad (2.9)$$

Slab waveguides confine the optical mode in only one dimension. For most integrated optical devices such as integrated space switches confinement of the optical mode in two dimensions is necessary, requiring a refractive index change in both dimensions perpendicular to the direction of propagation. We have chosen to use a ridge waveguide structure due to its ease of fabrication.

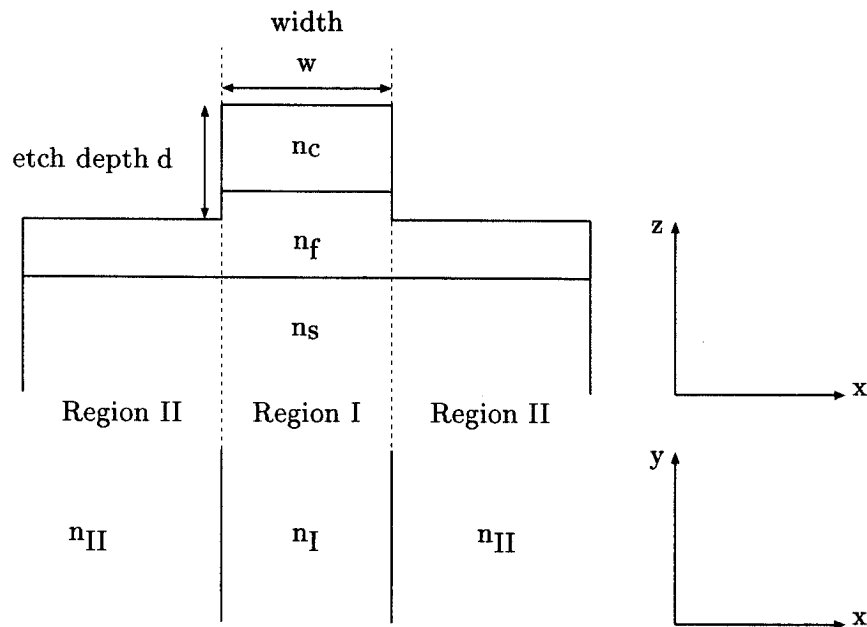


Fig. 2.4: Illustration of the effective index method. First the effective refractive indices are computed for a slab structure corresponding to the structure of region 1 and 2. These effective indices form a second slab where the optical guiding layer has the refractive index n_I and the width w . The “substrate” and “cladding” of this new slab have the refractive index n_{II} . If the index contrast is small, the effective refractive index of the structure is in good approximation the effective index of the second slab.

The properties of three dimensional waveguides generally needs to be determined by solving the wave equation for the structure numerically by using finite element and beam propagation algorithms. However, if the refractive index contrast is small the “effective index method” represents a good approximation. This method assumes for small refractive index contrasts that the guiding in two directions perpendicular to the directions of propagation is independent and can be separated. The computation of the effective refractive index is performed in two steps. First the effective indices n_I and n_{II} of the slab structures in the regions I and II is determined (see figure 2.4) as outlined above. In the second step the effective refractive index of the ridge structure is calculated by evaluating the effective index of a slab structure with the indices n_I and n_{II} for the film and cover/substrate respectively and a film thickness w .

The accurate knowledge of the effective refractive index and thereby the normalisation parameter b will be important later on for evaluating the absolute electric field induced refractive index changes and electro-optic coefficients.

2.4 *Electric field in a reverse biased p-i-n double-heterojunction waveguide*

To analyse the electro-optic effects occurring in a reverse biased p-i-n double heterojunctions it is necessary to know the strength of the electric fields experienced by the waveguide material and the width of the depletion zone. The only observable quantity is the applied bias voltage V it is necessary to derive the resulting electric field \vec{E} and the built-in voltage V_{bi} from a model. A model of an abrupt junction was chosen, with a free carrier and permittivity distribution matching the implemented structure as close as possible. This model assumes that the large carrier gradient in the junction causes holes from the p-side diffuse to the n-side and electrons from the n-side diffuse to the p-side. As electrons migrate to the p-side positive donor ions (N_D^+) near the junction are left behind uncompensated. Similarly migrating holes leave behind negative acceptor ions (N_A^-). This leads to the built-up of a negative space charge in the p-region and a positive space charge in the n-region causing an electric field and thereby a potential that counteracts the diffusion process. An equilibrium is reached when the said electric field causes the same number of carriers to drift back as are diffusing out of their region. The

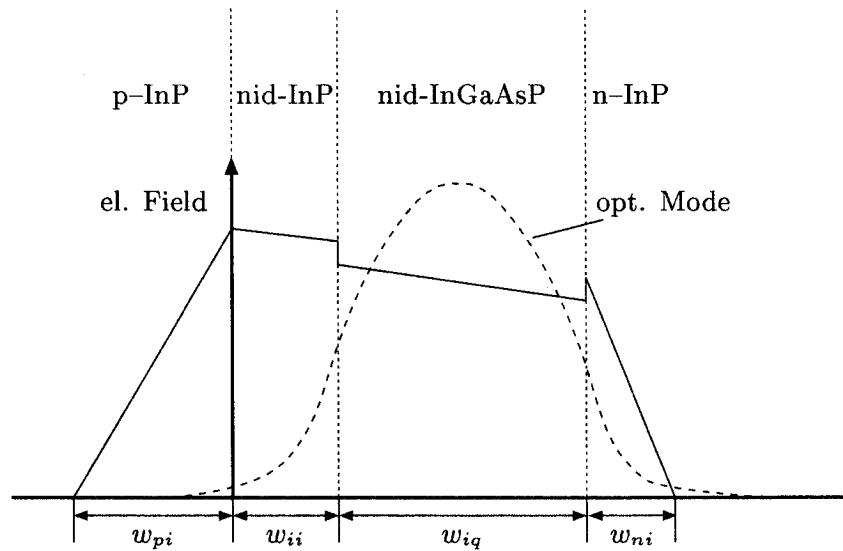


Fig. 2.5: Electric field in a reversed biased p-i-n diode.

potential induced by the diffusion process is called built-in voltage, which is usually in the order of several hundred millivolts.

The holes diffusing out of the p-doped region and electrons diffusing out of the n-doped zone they leave behind a zone depleted of carriers. Since the carrier concentration of this “depletion zone” is much lower than in the undepleted crystal, the resistivity is accordingly higher. By applying a negative bias voltage to the junction the depletion zone broadens and the electric field is increased.

Figure 2.5 gives a schematic overview of the structure and the resulting electric field. The free-carrier concentrations N_A , N_D and N_I for the p-, n- and not intentionally doped (nid) layer have been chosen to be $5 \times 10^{16} \left[\frac{1}{\text{cm}^3} \right]$, $2 \times 10^{17} \left[\frac{1}{\text{cm}^3} \right]$ and $5 \times 10^{15} \left[\frac{1}{\text{cm}^3} \right]$ respectively. The drop of the electric field in the quaternary layer is caused by the higher dielectric constant in this region.

2.5 Electro-optic effects in InP/InGaAsP

In electro-optics it is common practice to expand the electric field induced refractive index change Δn into a series of powers of the applied electric field;

$$\Delta n(E) = c_1 E + c_2 E^2 + \dots \quad (2.10)$$

The first term is called the "linear" or "Pockels" effect and the second term the "quadratic" or "Kerr" effect. Physical models however describe the properties of the dielectric constant ϵ , under the influence of an electric field. In materials with a low magnetic permeability such as insulators and semiconductors the refractive index and the dielectric constant are related by

$$n \simeq \sqrt{\epsilon} \quad (2.11)$$

For anisotropic crystals the dielectric constant is a tensor of second order ϵ_{ij} . The electro-optic tensors

$$\Delta \left(\frac{1}{\epsilon} \right)_{ij} = r_{ijk} E_k + R_{ijkl} E_k E_l \quad (2.12)$$

r_{ijk} and R_{ijkl} , where i, j, k and l represent the components of the incident and applied field with respect to the crystal axes, describe the linear and quadratic electro-optic effect.

The electric field induced refractive index changes are typically 3 to 4 orders of magnitude smaller than the refractive index itself. Therefore the refractive index change Δn can, by expanding equation (2.11), be written as

$$\Delta n = \frac{1}{2n} \Delta \epsilon \quad (2.13)$$

By rewriting equation (2.12) and using the relation (2.13) we can directly relate the refractive index change to the tensors r , R and the electric field E

$$\Delta n(E) = -\frac{n^3}{2} (r_{ijk} E_k + R_{ijkl} E_k E_l) \quad (2.14)$$

Not all coefficients of the tensors r_{ijk} and R_{ijkl} are independent. Due to symmetry considerations these tensors have to be invariant to permutation of the indices. Additionally the tensors have to show the same symmetry as the crystal structure. Therefore several elements of the electro-optic tensors are zero or have the same value. InP/InGaAsP has a zinkblende structure which belongs to the $\bar{4}3m$ point-symmetry class. Hence the reduced form of the electro-optic tensors for InP/InGaAsP is

$$r = \begin{bmatrix} 0 & 0 & 0 \\ 0 & 0 & 0 \\ 0 & 0 & 0 \\ r_{41} & 0 & 0 \\ 0 & r_{52} & 0 \\ 0 & 0 & r_{63} \end{bmatrix} \quad (2.15)$$

with $r_{14} = r_{25} = r_{36}$, and

$$R = \begin{bmatrix} R_{11} & R_{12} & R_{13} & 0 & 0 & 0 \\ R_{21} & R_{22} & R_{23} & 0 & 0 & 0 \\ R_{31} & R_{32} & R_{33} & 0 & 0 & 0 \\ 0 & 0 & 0 & R_{44} & 0 & 0 \\ 0 & 0 & 0 & 0 & R_{55} & 0 \\ 0 & 0 & 0 & 0 & 0 & R_{66} \end{bmatrix} \quad (2.16)$$

with $R_{11} = R_{22} = R_{33}$, $R_{44} = R_{55} = R_{66}$ and $R_{12} = R_{13} = R_{23} = R_{21} = R_{31} = R_{32}$.

This implies that for devices based (100) InP substrates with an electric field perpendicular to the substrate surface (the [100] direction) only the transverse electric (TE) polarised light is affected by the Pockels effect. Additionally the the Pockels effect shows a $\cos 2\varphi$, φ is measured with respect to the $[0\bar{1}1]$ axis, due to the $\bar{4}$ element of the symmetry group of InP. Thus together with equation (2.14) the refractive index change due to the Pockels effect is given by

$$\Delta n = -\frac{n^3}{2} \cdot r_{41} \cdot \cos 2\varphi \cdot E \quad (2.17)$$

For (100) InP substrates with electric fields in the [100] direction the R_{21} and R_{11} coefficients of the electro-optic tensor determine the quadratic electro-optic effect for TE and TM polarised light. The quadratic electro-optic effect is independent of the angle φ to the $[0\bar{1}1]$ axis, but not polarisation independent. The contribution of the quadratic electro-optic effect the the refractive index change for TE and TM polarised light are

$$\Delta n_{TE} = \frac{n^3}{2} \cdot R_{21} \cdot E^2 \quad (2.18)$$

$$\Delta n_{TM} = \frac{n^3}{2} \cdot R_{11} \cdot E^2 \quad (2.19)$$

2.5.1 Phase shift change in a p-i-n double heterojunction waveguide

The main sources of the refractive index change induced by the electric field are the Pockels-effect and the Kerr-effect. The refractive index n and the electro-optic coefficients depend on the material. Therefore, as the optic mode is not completely confined to the guiding layer and the electric field is not constant in the layers either, it is necessary to compute an average electric field, and the square thereof, weighted by the light intensity of the optical mode for each layer. The weighted averages of the electric-field and the square of the electric fields are given by

$$\bar{E} = \frac{\int_{Region} I(x) \cdot E(x) dx}{\int I(x) dx} \quad (2.20)$$

$$\bar{E}^2 = \frac{\int_{Region} I(x) \cdot E^2(x) dx}{\int I(x) dx} \quad (2.21)$$

In addition to the Pockels- and Kerr-effect variations in the carrier concentration also contribute to refractive index changes. When a diode is reverse biased the region around the junction is depleted from its carriers and thereby the refractive index of this depletion zone changed. To calculate the contribution from carrier depletion the change of carrier concentration has to be weighted with the intensity distribution of the optical mode as follows

$$\Gamma = \frac{\int_{depl. zone} I(x) \cdot \Delta N(x, E) dx}{\int I(x) dx} \quad (2.22)$$

$\Delta N(x)$ denotes the change of carrier concentration in the depletion zone.

Finally the phase shift in a an InGaAsP/InP base double-hetero p-i-n waveguide can be calculated for the TE and the TM mode by combining equations (2.3), (2.17), (2.18), (2.19), (2.20) and (2.21).

$$\Delta\varphi_{TE} = \frac{2\pi \cdot l}{\lambda} \cdot \frac{n^3}{2} (r_{41} \cdot \cos 2\alpha \cdot \bar{E} + R_{21} \cdot \bar{E}^2 + D \cdot \Gamma) \quad (2.23)$$

$$\Delta\varphi_{TM} = \frac{2\pi \cdot l}{\lambda} \cdot \frac{n^3}{2} (R_{11} \cdot \bar{E}^2 + D \cdot \Gamma) \quad (2.24)$$

3. ELECTRO-OPTIC EFFECTS

In this chapter models of the "free carrier effect", the Pockels effect and the Franz-Keldysh effect are presented. The "free carrier effect" and the Pockels effect are well described by a harmonic oscillator model. A more complex quantum mechanical model is required to describe the Franz Keldysh effect. This quantum mechanical model also predicts the wavelength and electric field dependency of the refractive index and absorption index change well.

3.1 Introduction

As pointed out in the introduction (section 1.2), for optical switches in III-V compound semiconductor waveguide materials electro-optic effects are preferred. They allow high switching speeds and low holding powers. "Free carrier effects" and current injection are best exploited in amplifier gates. Due to the fact, that almost all III-V compound semiconductor devices are fabricated on (100) substrates with [110] cleaved waveguide facets special waveguide orientations have to be employed to achieve polarisation independence. The polarisation independence is achieved by combining the linear Pockels effect and the approximately quadratic Franz-Keldysh electro optic effects.

The Pockels effect in structures based on (100) InP substrates affects only the TE mode and shows a $\cos(2\varphi)$ dependency with respect to the crystal axes. These properties are a direct consequence of the crystal symmetry.

The Franz-Keldysh effect on the other hand is strongly dispersive and polarisation dependent. It is also responsible for a strong dependence of the absorption index on the applied electric field and optical wavelength. In spite of its importance for the design of electro-optic space switches, very little is known about the Franz-Keldysh effect in InGaAsP.

3.2 Model of the carrier effect

This section deals with carrier effects occurring in reverse biased junctions. Effects caused by carrier injection are not considered here because the junctions of the switches in this thesis are only operated in the reverse bias regime where carrier effects are, except for electric fields below $4 \cdot 10^6 \frac{V}{m}$, side effects compared to the Pockels and the Franz-Keldysh effect.

The main contributors to the carrier effect are the *band filling (Burnstein-Moss)*, *band gap shrinking* and the *plasma effect*. They have been comprehensively studied for the InP/InGaAsP material system by J.E. Vinchant et. al. and B.R. Bennet et. al. [26, 27].

To make use of carrier effects the carrier concentration in the semiconductor has to be changed. This can be done effectively by forward or reverse biasing of a pin-diode. Forward biasing of a pn-junction allows for very high carrier concentration changes causing band filling and band gap shrinking to be the dominating effects. If the concentrations of free carriers is low, which is usually the case in unbiased semiconductors, the plasma effect is dominant.

By reverse biasing the semiconductor is depleted of these carriers and thereby the refractive index is changed.

Band filling occurs if the conduction band is filled by doping or by carrier injection (e.g. by forward biasing). Its effect is most pronounced if the effective mass of the carriers are small (n-type materials), since this leads to a sufficiently small density of states to be appreciably filled by a relatively small number of electrons. For p-type materials the effect is much smaller because the much higher effective mass of the holes leads to a higher density of states. With the lowest energies in the conduction band already filled, greater photon energies are required to excite electrons from the valence band into the conduction band. Thus band filling effectively enlarges the band gap.

On the other hand large electron concentrations lead to *band gap shrinking*. Shrinkage effects are determined by the free-carrier concentration, but are nearly independent of impurity concentration [28]. Therefore band gap shrinking only contributes significantly when carriers are injected, i.e. when the pn-junction is forward biased. The basic mechanism is that when the electron concentration in the conduction band get sufficiently high, the electrons start interacting with each other. They will repel each other through Coulomb forces and electrons of the same spin will avoid each other for statistical reasons. The net effect is a decrease of their energy and thereby lowering the energy of the conduction band. A similar mechanism for holes rises the energy of the valence band adding to the shrinkage of the band gap.

The band shrinking tends to cancel out the effect caused by the band filling. The total effect of these effects can only be determined by numerical analysis and can be positive or negative, depending on the electron concentration and the energy difference of the photon and the band gap [27]. The band filling and band shrinkage effect contribute most to the refractive index when the photon energy is close to the bandgap energy.

In addition these interband absorption related effects, interaction of light waves with free carriers influences the refractive index change in the material. For low carrier concentrations, i.e. below $5^{16}[\frac{1}{cm^3}]$ which is the case for the switches we study, and reverse biased diodes the *plasma effect* is dominant. Carriers in a crystal structure can be regarded as free, if the band in which the carrier moves is in good approximation parabolic, i.e. the kinetic energy of the carrier can be written as $E_{Kin} = \frac{p^2}{2\mu}$, where p denotes the impulse and μ the effective mass of the carrier. Assuming parabolic bands the behaviour

of a carrier with the charge q in a time varying electric field can be described by

$$\mu\ddot{x} = qE(t). \quad (3.1)$$

If the field varies harmonically in time with the frequency ω as $e^{-i\omega t}$ the dipole moment contributed by one carrier is

$$p = qx = \frac{q^2 E}{\mu\omega^2} \quad (3.2)$$

Using the relation of the dielectric constant ε

$$\varepsilon_{tot} = \varepsilon + \Delta\varepsilon_{carrier} = \varepsilon + \frac{1}{\varepsilon_0} Np \quad (3.3)$$

where N denotes the number of carriers per unit volume, with equation (3.2) we obtain for the contribution of the free carriers to the dielectric constant

$$\Delta\varepsilon_{carrier} = -\frac{1}{\varepsilon_0} \frac{Nq^2}{\mu\omega^2} \quad (3.4)$$

If the absorption can be neglected, we can write for the refractive index

$$n_{tot} \simeq \sqrt{\varepsilon_{tot}} = \sqrt{\varepsilon - \frac{1}{\varepsilon_0} \frac{Nq^2}{\mu\omega^2}} \quad (3.5)$$

The assumption of negligible absorption is generally valid if the photon energy is smaller than the band gap energy. The damping of the oscillations of the carriers in the optical field due to carrier-carrier or impurity scattering can also be neglected, because the carriers density is low in our case and the oscillation amplitudes of the carriers at the studied field intensities and frequencies are in the order of Angstroms. Since the change of the dielectric constant caused by plasma effect is orders of magnitude smaller than the dielectric constant itself we can use equation (2.13) together with equation (3.5) to compute the plasma effect induced refractive index change.

$$\Delta n = -\frac{1}{2n\varepsilon_0} \frac{Nq^2}{\mu\omega^2} \quad (3.6)$$

It can be seen from equation (3.6) that the refractive index change due to the plasma effect is always negative i.e an increase in carrier density lowers

the refractive index, inversely proportional to the square of the optical frequency and inversely proportional to the effective mass of the carriers. For InP the effective hole mass is $0.42m_{electron}$ and the effective electron mass is $0.075m_{electron}$. Thus free electrons contribute much more to the plasma effect than holes. For photon energies below the band gap the band filling effect adds to the plasma effect.

Carrier induced refractive index changes can be exploited to form optical wave guiding structures; e.g for optical waveguides n/n^+ structures can be used. The light in such a structure is guided in the lower doped region because the refractive index in the highly doped regions is lower due to the plasma and band filling effect.

Optical switching is typically achieved by carrier injection. In such a modulator carriers are injected into the optically guiding layer to change its refractive index. The choice of the bandgap energy of this layer and the injected carrier concentration is tricky because the total refractive index change is the sum of the index changes induced by the plasma effect, the band filling effect and the band shrinkage effect, which are all of the same order of magnitude, but not of the same sign [27]. For photon energies below the bandgap the band filling effect has a negative sign and adds to the plasma effect. On the other hand the band shrinkage effect is positive. Thus the total refractive index change is not a monotonous function of the injected carrier concentration and can, depending on the difference of the bandgap energy to the photon energy, even change its sign.

3.3 Model of the Pockels effect

The Pockels effect is the first term of the power series expansion (equation 2.10) of the refractive index change with respect to the applied electric field. An expansive description of the Pockels effect can be e.g. found in the lectures of Prof. P. Günter on quantum electronics [29, 30].

Most of the physics of dispersion can be described by the classical model for molecular polarisability extended to time varying electric fields. This model assumes that the electrons of an atom are tied to a heavy, immobile core by a spring with the force $F = -m\omega_0^2x$, where m and ω_0 denote the mass of the electron and is the frequency around the equilibrium position. Under the influence of an electric field the electron is displaced by the amount $x_0 = \frac{-eE}{m\omega_0^2}$ inducing a dipole moment $p = -ex = \frac{e^2}{m\omega_0^2}E$ which is related to the

dielectric constant by $\varepsilon = 1 + pN$ where N denotes the density of electrons. By extending this model to time varying fields the dispersion of most materials can be described quite accurately.

The harmonic oscillator model however fails to describe electric field induced refractive index changes. To include electric field induced refractive index changes into this model a small nonlinear term has to be added to the spring force binding the electron to its core [31, 32, 33, 34]. Thus the equation for the electron reads

$$m(\ddot{x} + \gamma\dot{x} + \omega_0^2 x + \nu x^2) = -e(E^{i\omega t} + E_{const}) \quad (3.7)$$

ν , $E^{i\omega t}$ and E_{const} represent the nonlinear coefficient of the spring force, the optical field and the constant external electric field. It is assumed that the nonlinearity is small, i.e. $\omega_0^2 x \ll \nu x^2$. To solve this equation, we substitute

$$y = x + \frac{eE}{m\omega_0^2} \quad (3.8)$$

into equation (3.7) and get

$$\ddot{y} + \gamma\dot{y} + \left(\omega_0^2 + \frac{2eE_{const}\nu}{m\omega_0^2}\right)y + \nu y^2 + \left(\frac{eE_{const}}{m\omega_0^2}\right)^2 \nu = -\frac{e}{m}Ee^{i\omega t} \quad (3.9)$$

We neglect the nonlinear term νx^2 because it is much smaller than $\omega_0^2 x$ as mentioned above and contributes only to second harmonic generation, not to field induced refractive index changes. So the solution of equation (3.9) reads

$$y = \frac{-\frac{e}{m}Ee^{i\omega t}}{\omega_0^2 - \omega^2 - i\gamma + \frac{2eE_{const}\nu}{m\omega_0^2}} - \left(\frac{eE_{const}}{m\omega_0^2}\right)^2 \frac{\nu}{\omega_0^2 + \frac{2eE_{const}\nu}{m\omega_0^2}} \quad (3.10)$$

Using the relation $\Delta\varepsilon = \frac{1}{\varepsilon_0}Ny$ and equation (2.13), the refractive index change can be written as

$$\Delta n = \frac{-eN}{2n\varepsilon_0}y \quad (3.11)$$

The contribution of the linear Pockels effect to $\Delta\varepsilon$ is the first term of the Taylor series of Δn

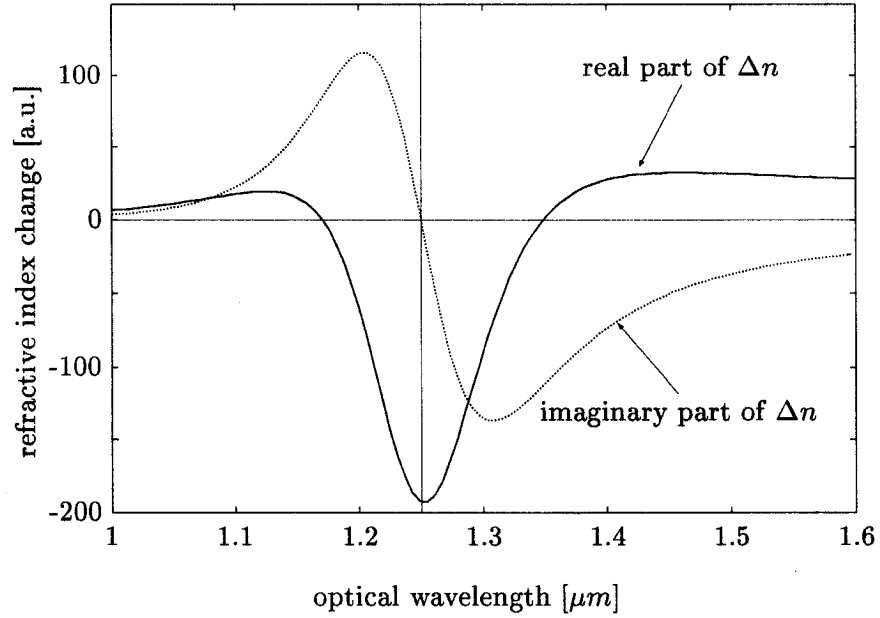


Fig. 3.1: Calculated real and imaginary part of the Pockels-effect induced refractive index change versus the wavelength of the optical mode. The Bandgap energy in this calculation was $1.25\mu m$.

$$\Delta n_{Pockels} = \frac{\partial \Delta n(E_{const} = 0)}{\partial E_{const}} E_{const} = \frac{-eN}{2n\epsilon_0} \frac{\partial y(E_{const} = 0)}{\partial E_{const}} E_{const} \quad (3.12)$$

and thus

$$\Delta n_{Pockels} = \frac{1}{2n} \cdot \frac{-e^3 N \nu}{\epsilon_0 m^2 \omega^2} \cdot \frac{E_{const}}{(\omega_o^2 - \omega^2 + i\gamma)^2} \quad (3.13)$$

Finally the electro-optic coefficient r_{ijk} can be obtained by comparing equation (3.13) and (2.14)

$$r_{ijk} = \frac{1}{n^4} \cdot \frac{e^3 N \nu}{\epsilon_0 m^2 \omega^2} \cdot \frac{1}{(\omega_o^2 - \omega^2 + i\gamma)^2} \quad (3.14)$$

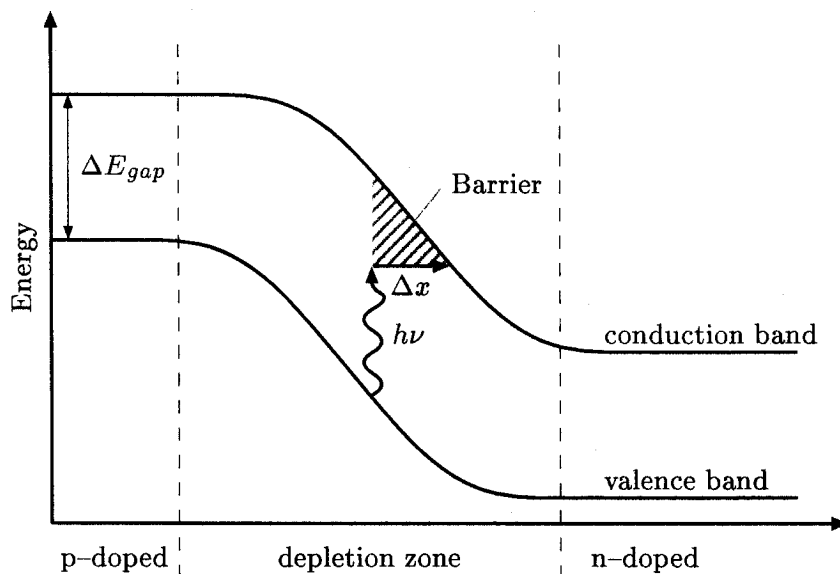


Fig. 3.2: Diagram of a photon assisted tunnelling of an electron in the reverse biased junction of a p-i-n diode

3.4 Model of the Franz Keldysh effect

A significant contribution to the quadratic electro-optic effect in InP and InGaAsP is the Franz-Keldysh effect. It was proposed independently at the same time by W. Franz [35] and L.V. Keldysh [36] in 1958. The Franz-Keldysh effect is an electric field induced photon assisted tunnelling effect. By lowering the effective band-gap energy in a crystal in the presence of an electric field, it acts on the absorption index and on the refractive index.

The physics of the Franz-Keldysh effect can be explained by band deformation in the presence of electric fields. Normally a semiconductor crystal is transparent for photon energies below the bandgap energy. In the presence of an electric field, as it occurs in a pn-junction, however, the conduction and valence band are bent (the details on band bending in semiconductors and pn-junctions can be found in textbooks, e.g. [37]). The bending of energy bands makes tunnelling from the valence to the conduction band possible (see figure 3.2). The electrons have to tunnel through a triangular barrier, that is the smaller the photon energy is to the bandgap energy and the higher the electric field is, because the tunnelling distance Δx decreases with increasing

electric field. Thus the tunnelling probability, and thereby the absorption index, increases with the higher electric fields and photon energies.

Since the initial calculations of W. Franz [35] and L. Keldysh [36] a detailed theoretical study of the electric field dependency of the optical absorption near normal absorption edges has been carried out for direct [38, 39, 40, 41, 42, 43] and indirect transitions [44, 45]. Some experimental verification of these theoretical has been done either by direct absorption measurements [46] and reflection measurements [47].

3.4.1 The imaginary part of the dielectric constant

This section concerns itself with the behaviour of the imaginary part of the dielectric function under influence of an electric field in InP or InGaAsP. The main contribution of the field induced absorption originates from interband absorption around the M_0 critical point, which means that all the components of the effective mass of an electron-hole pair are positive in InP and InGaAsP. The derivation of the imaginary part of the dielectric constant given below assumes parabolic bands and follows the one given by Aspnes [41] and is limited to the case of interband absorption around a M_0 critical point.

The imaginary part of the dielectric constant is defined by [38]

$$\varepsilon_2 = \frac{4\pi^2 e^2}{m^2 \omega^2} \sum_i |P_{if}|^2 \delta(E_f - E_i - \hbar\omega) \quad (3.15)$$

where P_{fi} denotes the matrix element for an electron transition from the initial state to the final state and the delta function guarantees the conservation of energy. For allowed transition the matrix element can be written as [48]

$$P_{if} = \phi(0) C_0 \delta_{k_i, k_f} \quad (3.16)$$

C_0 represents the matrix element between the periodic parts of the Bloch waves at the band edge, and $\phi(r)$ the solution of the Schrödinger equation for an electron hole pair. The imaginary part of the dielectric constant can therefore be written as

$$\varepsilon_2 = \frac{4\pi^2 e^2}{m^2 \omega^2} \sum_i C_0^2 |\phi(0)|^2 \delta(E_f - E_i - \hbar\omega) \quad (3.17)$$

The Schrödinger equation for an electron-hole pair with the effective masses μ_i along the symmetry axes in the presence of an electric field reads

$$\left(\frac{\hbar}{2\mu_x} \frac{\partial^2}{\partial x^2} + \frac{\hbar}{2\mu_y} \frac{\partial^2}{\partial y^2} + \frac{\hbar}{2\mu_z} \frac{\partial^2}{\partial z^2} + e \cdot \vec{E} + E \right) \phi(\vec{r}) = 0 \quad (3.18)$$

In equation (3.18) the electron-hole interaction has been neglected. It has an exact solution [49] that involves Airy-Functions

$$\phi(\vec{r}) = C_x C_y C_z \text{Ai}(-\xi_x) \text{Ai}(-\xi_y) \text{Ai}(-\xi_z) \quad (3.19)$$

where

$$\xi_i = i \frac{|e|E_i}{\hbar\varphi_i} + \frac{\epsilon_i}{\hbar\varphi} \quad (3.20)$$

with

$$\varphi_i^3 = \frac{e^2 E_i^2}{2\hbar\mu_i} \quad \text{and} \quad E = \epsilon_x + \epsilon_y + \epsilon_z$$

The constants C_i , normalising the delta functions with respect to the integral for each ϵ_i , are given by

$$C_i = N \frac{\sqrt{|e|E_i}}{\pi\hbar\varphi_i} \quad (3.21)$$

By substituting equations (3.20) and (3.19) into equation (3.17), converting the sum with an integral over ϵ_x , ϵ_y and ϵ_z , adding a factor of 2 to account for the two possible spin states of an electron and doing some algebra we obtain for the imaginary part of the dielectric constant

$$\begin{aligned} \epsilon_2 = & \frac{nc}{\omega} \frac{4RN^6}{\hbar^2 \pi^4 (\varphi_x \varphi_y \varphi_z)^{\frac{1}{2}}} \iiint d\epsilon_x d\epsilon_y d\epsilon_z \text{Ai}^2 \left(-\frac{\epsilon_x}{\hbar\varphi_x} \right) \text{Ai}^2 \left(-\frac{\epsilon_y}{\hbar\varphi_y} \right) \\ & \cdot \text{Ai}^2 \left(-\frac{\epsilon_z}{\hbar\varphi_z} \right) \delta(E_g - \hbar\omega + \epsilon_x + \epsilon_y + \epsilon_z) \end{aligned} \quad (3.22)$$

with

$$R = \frac{2e^2 C_0^2}{\hbar\omega n c m^2} \left(\frac{8\mu_x \mu_y \mu_z}{\hbar^3} \right)^{\frac{1}{2}} \quad (3.23)$$

To evaluate the integral in equation (3.22) we make use of the fact that the delta function contributes only if its argument is zero, i.e

$$E_g - \hbar\omega + \epsilon_x + \epsilon_y + \epsilon_z = 0$$

and integrate over ϵ_x to get rid of the delta function. The integral now reads

$$\iint d\epsilon_y d\epsilon_z \text{Ai}^2\left(-\frac{E_g - \hbar\omega + \epsilon_x + \epsilon_y}{\hbar\varphi_x}\right) \text{Ai}^2\left(-\frac{\epsilon_y}{\hbar\varphi_y}\right) \text{Ai}^2\left(-\frac{\epsilon_z}{\hbar\varphi_z}\right)$$

Next we substitute $r = -\frac{\epsilon_y}{\hbar\varphi_y}$ and $s = -\frac{\epsilon_z}{\hbar\varphi_z}$ and obtain

$$\varepsilon_2 = \frac{nc}{\omega} \frac{4RN^6(\varphi_y\varphi_z)^{\frac{1}{2}}}{\pi^4\varphi_x^{\frac{1}{2}}} \int dr \text{Ai}^2(r) \int ds \text{Ai}^2(s) \text{Ai}^2\left(\frac{E_g - \hbar\omega}{\hbar\varphi_x} - r\frac{\varphi_y}{\varphi_x} - s\frac{\varphi_z}{\varphi_x}\right) \quad (3.24)$$

These integrals can be evaluated by applying the following integral relation [41]

$$\int_{-\infty}^{\infty} dt \text{Ai}^2(t+x) \text{Ai}^2(y-\alpha t) = \frac{\pi}{2N^2\sqrt{\alpha}} \int_0^{\infty} \frac{du}{\sqrt{u}} \text{Ai}^2\left(u + \frac{\alpha x + y}{(1+\alpha^3)^{\frac{1}{3}}}\right) \quad (3.25)$$

to equation (3.24) and integrating over s we obtain

$$\varepsilon_2 = \frac{nc}{\omega} \frac{2RN^4\varphi_y^{\frac{1}{2}}}{\pi^3} \int_0^{\infty} \frac{du}{\sqrt{u}} \int_{-\infty}^{\infty} \text{Ai}^2(r) \text{Ai}^2\left(u + \frac{E_g - \hbar\omega}{\hbar(\varphi_x^3 + \varphi_z^3)^{\frac{1}{3}}} - r\frac{\varphi_y}{\hbar(\varphi_x^3 + \varphi_z^3)^{\frac{1}{3}}}\right) \quad (3.26)$$

A second application of equation (3.25) yield

$$\varepsilon_2 = \frac{nc}{\omega} \frac{N^2R}{\pi^2} (\varphi_x^3 + \varphi_z^3)^{\frac{1}{6}} \int_0^{\infty} \int_0^{\infty} \frac{du dw}{\sqrt{uw}} \text{Ai}^2\left(w + u\frac{(\varphi_x^3 + \varphi_z^3)^{\frac{1}{3}}}{\varphi_0} + \frac{E_g - \hbar\omega}{\hbar\varphi_0}\right) \quad (3.27)$$

where $\varphi_0^3 = \varphi_x^3 + \varphi_y^3 + \varphi_z^3$. Finally, by changing variables and applying the relations [41]

$$\int_0^{\infty} \int_0^{\infty} \frac{dx dy}{\sqrt{xy}} \text{Ai}^2(x+y) = \pi \int_0^{\infty} dz \text{Ai}^2(z) \quad (3.28)$$

and

$$-\int_{\eta}^{\infty} du \operatorname{Ai}^2(x) = \eta \operatorname{Ai}^2(\eta) - \operatorname{Ai}'^2(\eta) \quad (3.29)$$

the a closed relation for the imaginary part of the dielectric function

$$\varepsilon_2 = \frac{nc}{\omega} \frac{RN^2}{\pi} \varphi_0^{\frac{1}{2}} [\operatorname{Ai}'^2(\eta) - \operatorname{Ai}^2(\eta)] \quad (3.30)$$

is obtained, where

$$\eta = \frac{E_g - \hbar\omega}{\hbar\varphi_0} \quad (3.31)$$

In order to make use of this result, we have to calculate the experimentally measurable change

$$\Delta\varepsilon_2(\vec{E}) = \varepsilon_2(\vec{E}) - \lim_{|\vec{E}| \rightarrow 0} \varepsilon_2(\vec{E}) \quad (3.32)$$

Because η becomes infinite as \vec{E} vanishes, the asymptotic forms of the Airy functions [50] can be used for $x \rightarrow \infty$

$$x \operatorname{Ai}^2(x) \sim \frac{\pi}{4N^2} x^{\frac{1}{2}} e^{-\frac{4}{3}x} \sim \operatorname{Ai}'^2(x) \quad (3.33)$$

$$x \operatorname{Ai}^2(-x) \sim \frac{\pi}{4N^2} x^{\frac{1}{2}} \sin^2 \left(\frac{2}{3}(-x)^{\frac{2}{3}} + \frac{1}{4}\pi \right) \quad (3.34)$$

$$x \operatorname{Ai}'^2(-x) \sim \frac{\pi}{4N^2} x^{\frac{1}{2}} \cos^2 \left(\frac{2}{3}(-x)^{\frac{2}{3}} + \frac{1}{4}\pi \right) \quad (3.35)$$

$$(3.36)$$

to calculate the limes $\lim_{|\vec{E}| \rightarrow 0} \varepsilon_2(\vec{E})$ and $\Delta\varepsilon_2$, which reads

$$\Delta\varepsilon_2 = \frac{nc}{\omega} R \varphi_0^{\frac{1}{2}} F(\eta) \quad (3.37)$$

where $F(\eta)$ is defined as

$$F(\eta) = \frac{N^2}{\pi} [\operatorname{Ai}'^2(\eta) - \eta \operatorname{Ai}^2(\eta)] - \sqrt{-\eta} H(-\eta) \quad (3.38)$$

and $H(x)$ represents the unit step function which is 1 for positive x and zero otherwise.

Integrated optical devices are operated at wavelength below the absorption edge, i.e. $\eta > 0$ and with relatively small fields. For moderate field strengths typically occurring in InP/InGaAsP based devices η is large (10 and 100). Thus the asymptotic expansion of Airy functions [50]

$$\text{Ai}(z) \sim \frac{1}{2\pi^{\frac{1}{2}}} z^{-\frac{1}{4}} e^{-\zeta} \left[\sum_{k=0}^{\infty} (-1)^k c_k \zeta^{-k} \right] \quad (3.39)$$

$$\text{Ai}'(z) \sim \frac{1}{2\pi^{\frac{1}{2}}} z^{\frac{1}{4}} e^{-\zeta} \left[\sum_{k=0}^{\infty} (-1)^k d_k \zeta^{-k} \right] \quad (3.40)$$

$$c_0 = 1 \quad , \quad c_k = \frac{\Gamma(2k + \frac{1}{2})}{54^k k! \Gamma(k + \frac{1}{2})} \quad (3.41)$$

$$d_0 = 1 \quad , \quad d_k = -\frac{6k+1}{6k-1} c_k \quad (3.42)$$

where $\zeta = \frac{2}{3} z^{\frac{3}{2}}$, can be used to expand equation (3.38). By using the fact that $c_1 = \frac{5}{72}$ and neglecting all but the first term

$$F(\eta) = \frac{N^2}{\pi} \frac{1}{8\eta} e^{-\frac{4}{3}\eta^{\frac{3}{2}}} \quad (3.43)$$

is obtained.

3.4.2 The real part of the dielectric constant

The direct calculation of the real part of the dielectric constant ε_1 is much more complicated than the calculation of the imaginary part ε_2 as it involves a lot of complicated quantum mechanics. An expression for the frequency dependent dielectric constant ε_1 is derived by Callaway [51, 52]

$$\varepsilon_1 = 1 + \frac{e^2}{m\omega^2\varepsilon_0} \sum_{\vec{k}, l} N_l(\vec{k}) \cdot \left[1 - \frac{2}{3\hbar m} \sum_{n \neq m} \frac{\omega_{nl}(\vec{k}) |\vec{p}_{nl}(\vec{k})|^2}{\omega_{nl}(\vec{k})^2 - \omega^2} \right] \quad (3.44)$$

where the quantities N_l denote the density of states in the band l , ω the frequency of the incident light, p_{ln} the momentum matrix elements and $\hbar\omega_{nl}$

the energy difference between the bands l and n . In a semiconductor, all bands are either completely full or completely empty and, by neglecting the contributions of free carriers, which give rise to the plasma effect, equation (3.44) reduces to

$$\varepsilon_1 = 1 + \frac{2e^2}{3m^2\omega^2\varepsilon_0} \sum_{\vec{k}, l} N_l(\vec{k}) \sum_{n \neq m} \frac{|\vec{p}_{nl}(\vec{k})|^2}{\omega_{nl}(\omega_{nl}^2 - \omega^2)} \quad (3.45)$$

This equation of the real part of the dielectric constant involves sums over all bands of the semiconductor and is therefore too complicated to evaluate. Since the largest contributions to the change of the real part of the dielectric constant originate from the onset of interband transitions (Van Hove singularities in the density of states), and we are interested only in the electric field induced changes of the dielectric constant, it suffices to regard the onset of the transition from the valence band to the conduction band, i.e. the pair of bands which are closest at $\vec{k} = 0$. By using the parabolic band approximation and wave functions which are solutions of the Schrödinger equation of an electron hole pair in the presence of an electric field (equation (3.18)) one obtains

$$\varepsilon_1 = 1 + B\varphi_0^{\frac{1}{2}} \cdot \int_{\frac{E_g}{\hbar\varphi_0}}^{\infty} dt \frac{2}{\pi} P \int_{-\infty}^{\infty} \frac{\text{Ai}^2\left(t - \frac{\omega'}{\varphi_0}\right)}{\omega'(\omega' - \omega)(\omega' + \omega)} d\omega' \quad (3.46)$$

The same result can also be obtained by performing a Kramers–Kronig transformation on the imaginary part of the dielectric constant [42].

To evaluate the principal integral of equation (3.46) the denominator has to be broken up using the method of partial fractions and the following relation are needed. Comparing the real parts of relation A8b of [42], it follows that

$$P \int_{-\infty}^{\infty} \frac{\text{Ai}^2(x')}{x' - x} dx' = -i\pi \text{Ai}(x) \text{Bi}(x) \quad (3.47)$$

The relation for ε_1 now reads

$$\varepsilon_1 = 1 + \frac{2}{\omega^2} B\varphi_0^{\frac{1}{2}} \cdot \left(\int_{\frac{E_g}{\hbar\varphi_0}}^{\infty} \text{Ai}(u) \text{Bi}(u) du - \right.$$

$$\begin{aligned}
& - \frac{1}{2} \int_{\frac{E_g + \hbar\omega}{\hbar\varphi_0}}^{\infty} \text{Ai}(u) \text{Bi}(u) du - \\
& - \frac{1}{2} \int_{\frac{E_g - \hbar\omega}{\hbar\varphi_0}}^{\infty} \text{Ai}(u) \text{Bi}(u) du \Big) \quad (3.48)
\end{aligned}$$

These integrals can be finally evaluated using [41, equation B22]

$$\int^t \text{Ai}(u) \text{Bi}(u) du = t \text{Ai}(t) \text{Bi}(t) - \text{Ai}'(t) \text{Bi}'(t) \quad (3.49)$$

resulting in

$$\begin{aligned}
\varepsilon_1 &= 1 - \frac{B\varphi_0^{\frac{1}{2}}}{\omega^2} \left\{ 2\pi [\text{Ai}'(\alpha) \text{Bi}'(\alpha) - \alpha \text{Ai}(\alpha) \text{Bi}(\alpha)] \right. \\
& - \pi [\text{Ai}'(\beta) \text{Bi}'(\beta) - \beta \text{Ai}(\beta) \text{Bi}(\beta)] \\
& \left. - \pi [\text{Ai}'(\eta) \text{Bi}'(\eta) - \eta \text{Ai}(\eta) \text{Bi}(\eta)] \right\} \quad (3.50)
\end{aligned}$$

with $\alpha = \frac{E_g}{\hbar\varphi_0}$, $\beta = \frac{E_g + \hbar\omega}{\hbar\varphi_0}$ and $\eta = \frac{E_g - \hbar\omega}{\hbar\varphi_0}$. The experimentally measured change of the real part of the dielectric constant is obtained by calculating the limit $\lim_{E \rightarrow 0} \varepsilon_1$ using the asymptotic forms for $x \rightarrow \infty$ (equations (3.39), (3.40) and below)

$$\text{Bi}(z) \sim \pi^{-\frac{1}{2}} z^{-\frac{1}{4}} e^{\zeta} \left[\sum_{k=0}^{\infty} (-1)^k c_k \zeta^{-k} \right] \quad (3.51)$$

$$\text{Bi}'(z) \sim \pi^{-\frac{1}{2}} z^{\frac{1}{4}} e^{\zeta} \left[\sum_{k=0}^{\infty} (-1)^k d_k \zeta^{-k} \right] \quad (3.52)$$

c_k and d_k are defined in equations (3.41) and (3.42). $\Delta\varepsilon_1$ now reads

$$\Delta\varepsilon_1 = \frac{B\varphi_0^{\frac{1}{2}}}{\omega^2} (G(\alpha) + G(\beta) + G(\gamma)) \quad (3.53)$$

$G(x)$ is called the electro-optic function of the second kind and is defined as

$$G(x) = \frac{N^2}{\pi} [\text{Ai}'(x) \text{Bi}'(x) - x \text{Ai}(x) \text{Bi}(x)] + \sqrt{x} \text{H}(x) \quad (3.54)$$

The function $H(x)$ is the unit-step function and is 0 for all negative arguments and 1 for all positive arguments.

Under the conditions normally occurring in InP/InGaAsP based electro-optic space switches, i.e. electric fields in the order of $10^6[\frac{V}{m}]$, $E_g = 1[eV]$ and optical wavelengths of $1.55[\mu m]$, the contributions of $G(\alpha)$ and $G(\beta)$ are at least 2 orders of magnitude smaller than the contribution of $G(\eta)$ and can therefore be neglected. As mentioned above (section 3.4.1), η is large under the normal operating conditions of an electro-optic space switch. Therefore the asymptotic forms of the Airy functions (equations (3.39), (3.40), (3.51), (3.52)) are very good approximations. Expanding $G(\eta)$ and keeping only the term of the lowest order, one obtains

$$G(\eta) = \frac{107}{2404} \frac{1}{\eta^{\frac{5}{2}}} \quad (3.55)$$

Substituting equation (3.31) into equation (3.55) and using

$$\varphi_0^3 = \frac{e^2 |E^2|}{2\mu\hbar} \quad (3.56)$$

one finally obtains for the electric field induced change of the real part of the dielectric constant

$$\Delta\varepsilon_1(E, \omega) = \frac{107}{2404} \frac{B\hbar^{\frac{3}{2}}}{2\mu\omega^2} \frac{e^2 |E^2|}{(E_g - \hbar\omega)^{\frac{5}{2}}} \quad (3.57)$$

The electro-optic coefficient R_{ij} follows from comparison of equation (3.57) and (2.18) or (2.19) for small refractive index changes

$$R = \frac{107}{2404} \frac{B\hbar^{\frac{3}{2}}}{2n^4\mu\omega^2} \frac{e^2}{(E_g - \hbar\omega)^{\frac{5}{2}}} \quad (3.58)$$

From equation (3.57) it can be seen that the Franz-Keldysh effect is proportional to the square of the electric field. It contributes therefore to the Kerr effect. As the Franz-Keldysh effect is also inversely proportional to $(E_g - \hbar\omega)^{\frac{5}{2}}$, it is strongly dispersive for photon energies near the bandgap.

3.5 Electro-optic effects in waveguides on (100) InP

In this work all waveguides are based on (100) InP substrates. This implies that the optical mode propagate in the (100) crystal plane and the applied electric fields are oriented perpendicular to the (100) crystal plane. As described in section 2.5 InP has a zinkblende structure which belongs to the $\bar{4}3m$ point-symmetry class.

3.5.1 Pockels Effect in (100) InGaAsP/InP

Under the conditions described above all coefficients of the electro-optic tensor r_{ijk} except $r_{41} = r_{52} = r_{63}$ are zero. Consequently the Pockels effect affects only TE polarised light and shows a $\cos(2\varphi)$ dependency with respect to the $[\bar{1}10]$ crystal axis.

From the oscillator model described in section 3.3 only a small dependency of r_{41} on the bandgap energy to photon energy difference, also called energy detuning, is expected for photon energies sufficiently far from the bandgap energy. The lineshapes of the real and imaginary refractive index change as calculated from equation (3.13) are plotted in figure 3.1. It can be seen that for a bandgap wavelength of $1.25 \mu m$ the Pockels-effect shows only very little dispersion between 1.4 and $1.6 \mu m$, which is the region relevant for the design of integrated optic devices.

The properties of the Pockels effect can be exploited to design polarisation independent modulators. The fact that it affects only the TE polarised light and its $\cos(2\varphi)$ dependency with respect to the crystal axes, allows the compensation of a polarisation dependence of the Franz-Keldysh effect. By choosing the orientation of the waveguide a defined fraction of the Pockels effect can be added to the Franz-Keldysh effect to achieve polarisation insensitivity.

3.5.2 Franz-Keldysh Effect in (100) InGaAsP/InP

Due to the crystal symmetry of InGaAsP/InP only the coefficients R_{21} and R_{11} , affecting the TE and TM mode respectively, are relevant in waveguides based on (100) InP wafers. From the point symmetry group of InGaAsP/InP no predictions concerning the relationship between R_{11} and R_{21} can be made. It is therefore likely that these two coefficients are not equal, which means that the Franz-Keldysh is not likely to be polarisation independent.

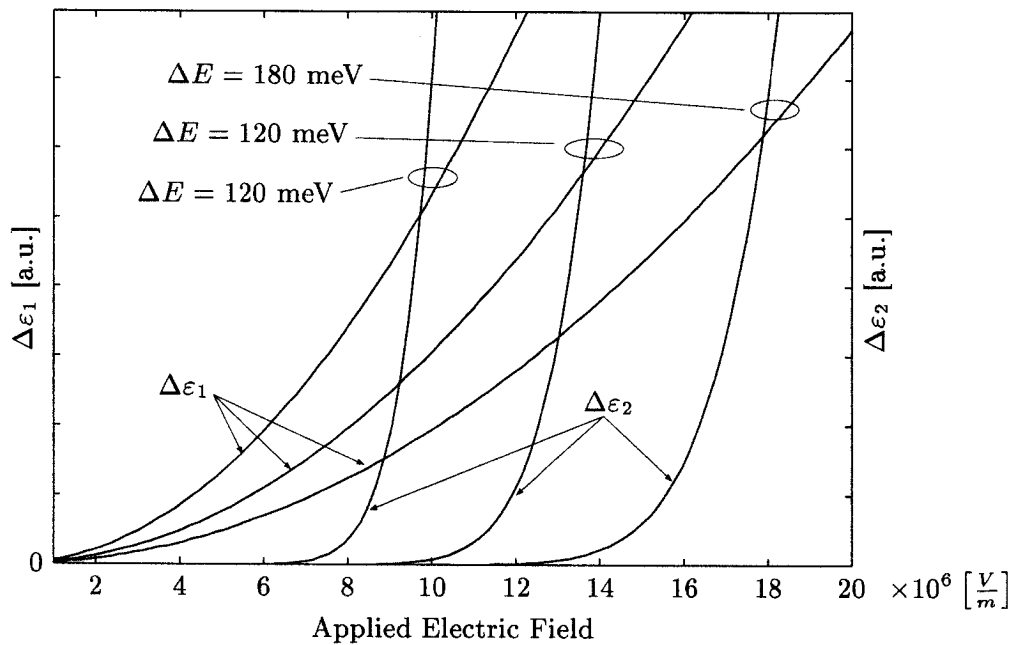


Fig. 3.3: Calculated lineshapes of $\Delta\epsilon_1$ and $\Delta\epsilon_2$ versus the applied electric field for photon to bandgap energy differences of 120, 150 and 180 meV. The effective mass of the electron-hole pairs is assumed to be $0.2 m_e$

In figure 3.3 the lineshapes of the real and imaginary part of $\Delta\epsilon_1$ $\Delta\epsilon_2$ and are plotted for an energy detuning of 120, 150 and 180 meV with an assumed effective mass of the electron-hole pairs of $0.2 m_e$. It can be seen that $\Delta\epsilon_1$ increases as the energy detuning decreases. Furthermore $\Delta\epsilon_2$ increases rapidly from a certain electric field strength on. This threshold electric field strength decreases with decreasing bandgap to photon energy difference.

For efficient electro-optical switching it is desirable to use waveguide structures with a small energy detuning. The behaviour of $\Delta\epsilon_2$ however imposes a lower limit to the energy detuning, because the optical losses have to be kept low. One has also to keep in mind, that even in an unbiased waveguide, there is an electric field in the order of $10^6 \frac{V}{m}$ due to the built in voltage of the p-i-n diode structure. This built in electric field can contribute substantially to the optical losses of a waveguide, provided the energy detuning is sufficiently small.

4. MEASUREMENT OF THE ELECTRO-OPTICAL EFFECTS

To verify the theoretical predictions of the previous chapter the changes of the refractive index and the absorption index were measured versus the applied electric field. These measurements were carried out for multiple optical wavelengths, angles to the crystal axes and polarisations. The obtained experimental data fit very well with the theoretical predictions.

4.1 Introduction

The magnitude of the electro-optic effects in InGaAsP was determined by measuring the refractive index change of an optical mode in a double heterojunction InGaAsP/InP ridge waveguide forming a pin-diode. This method allows the measurement of refractive index changes at a well defined polarisation and angle with respect to the crystal axes. It also allows easy application of electric fields in the order of 10^7 to 10^8 [$\frac{V}{m}$] by reverse biasing the pin-diodes. The refractive index changes can be determined by measuring the response of 2×2 Mach-Zehnder type interferometric space switches very accurately.

The measurements were performed on special chips featuring 2×2 Mach-Zehnder type space switches oriented under various angles with respect to the $[0\bar{1}1]$ crystal axis, as shown in figures 4.1(a) and 4.1(b).

A schematic of the measurement setup is depicted in figure 4.2. The light of an external cavity laser (ECL), which acts as a tunable lightsource ($1.47 - 1.59\mu\text{m}$), is guided via a single mode fibre to a polarisation controller and from there to the optical bench. A microscope objective is used to collect the optical mode exiting the end of the single mode fibre. The beam passes an adjustable polariser and is focused on the facet of the chip under test using a $20\times$ microscope objective. The optical responses of the switches were measured versus the applied voltage by projecting the light of the output waveguides with a second $20\times$ microscope objective onto a large area InGaAs photodiode for optical wavelength between $1.47\mu\text{m}$ and $1.55\mu\text{m}$, TE and TM polarisation and bandgap wavelengths of the chips of $1.25\mu\text{m}$ and $1.35\mu\text{m}$.

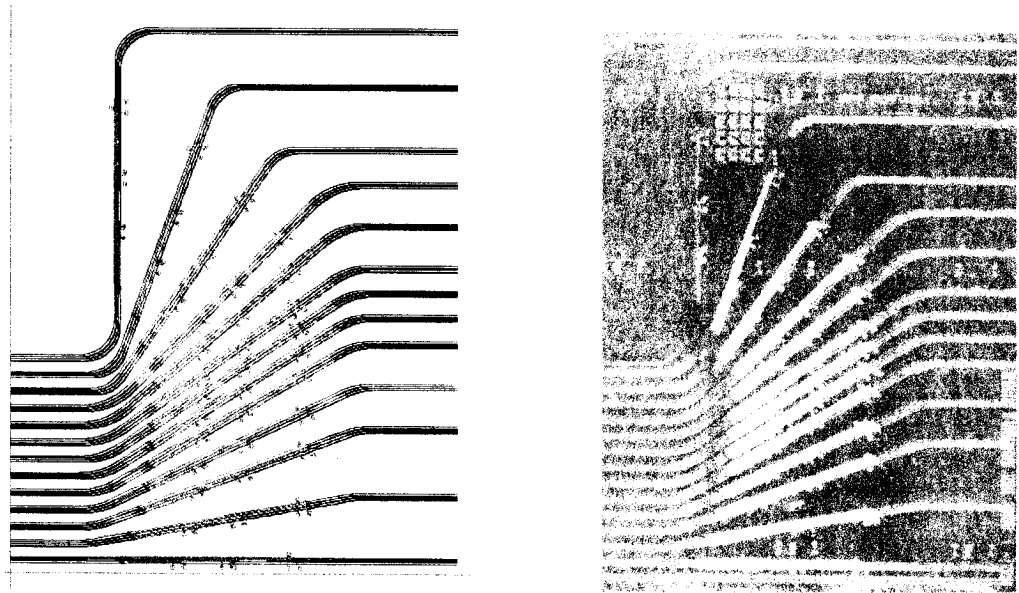
4.1.1 The refractive and the absorption index

The refractive index change Δn and the absorption index $\Delta\alpha$ have been measured. To compare the experimental results with the theoretical calculations, these quantities have to be calculated from $\Delta\varepsilon_1$ and $\Delta\varepsilon_2$.

The complex refractive index $\tilde{n} = n + ik$ is related the complex dielectric constant $\varepsilon = \varepsilon_1 + i\varepsilon_2$ by

$$\varepsilon = \tilde{n}^2 \quad \text{or} \quad \varepsilon_1 + i\varepsilon_2 = (n + ik)^2 \quad (4.1)$$

where k is the extinction coefficient and is related to the absorption coefficient α by



(a) Mask layout of chip used

(b) Photograph of the chip used

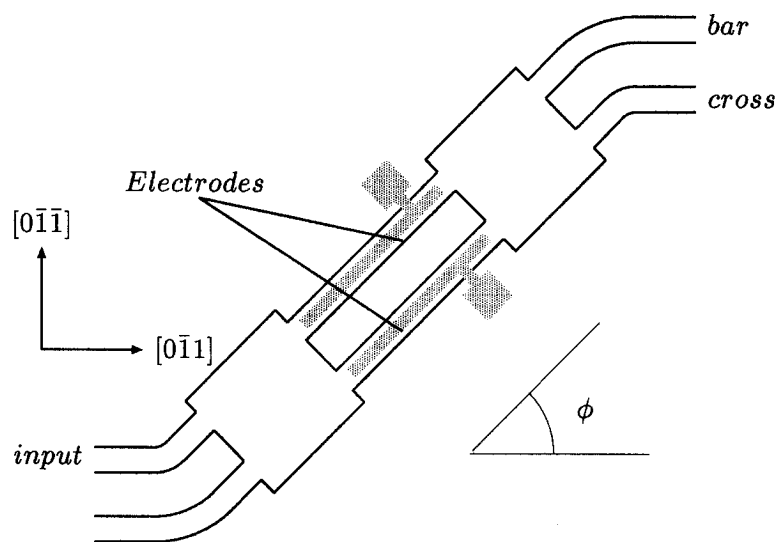
(c) Layout of a single 2×2 Mach-Zehnder interferometric switch

Fig. 4.1: Mask-layout and photograph of the chip used for measuring the electro-optic effects

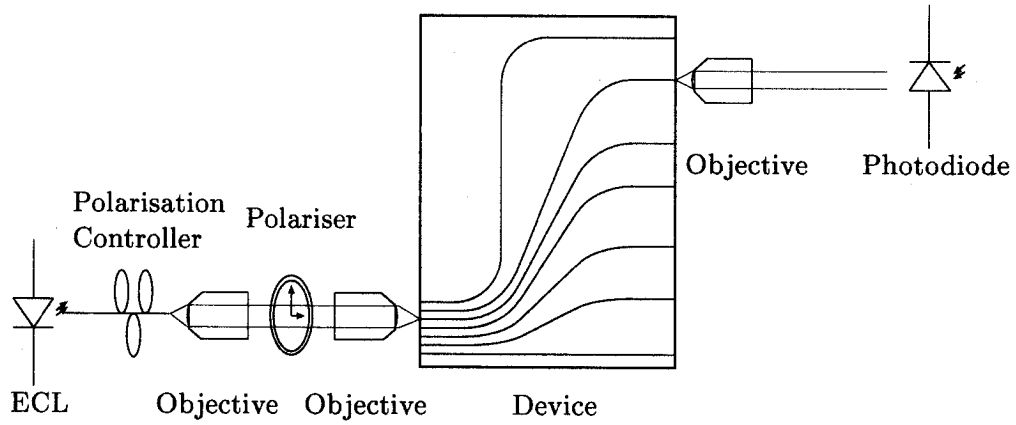


Fig. 4.2: Schematic of the experimental setup to measure the refractive index change

$$\alpha = \frac{2\omega k}{c} = \frac{\varepsilon_2 \omega}{nc} \quad (4.2)$$

Comparing the real and the imaginary part of both sides of equation (4.1) yields

$$\varepsilon_1 = n^2 - k^2 \quad (4.3)$$

$$\varepsilon_2 = 2nk \quad (4.4)$$

As mentioned above we are interested in the experimentally measurable changes of the absorption and of the refractive index. These quantities can be calculated by substituting in equation (4.3) and (4.4) $n = n_0 + \Delta n$, $k = k_0 + \Delta k$, $\varepsilon_1 = \varepsilon_{10} + \Delta\varepsilon_1$ and $\varepsilon_2 = \varepsilon_{20} + \Delta\varepsilon_2$. Nonlinear terms of Δn and Δk can be neglected as $\Delta n \ll n$ and $\Delta k \ll k$. Thus one obtains for $\Delta\varepsilon_1$ and $\Delta\varepsilon_2$

$$\Delta\varepsilon_1 \approx 2n_0\Delta n - 2k_0\Delta k \quad (4.5)$$

$$\Delta\varepsilon_2 \approx 2n_0\Delta k + 2k_0\Delta n \quad (4.6)$$

Under conditions usually occurring in InP/InGaAsP based space switches $k \ll n$. Thus the expressions for $\Delta\varepsilon_1$ and $\Delta\varepsilon_2$ can be reduced further to read

$$\Delta n \approx \frac{\Delta \varepsilon_1}{2n_0} \quad (4.7)$$

$$\Delta k \approx \frac{\Delta \varepsilon_2}{2n_0} \quad (4.8)$$

4.2 Measurement of the field dependency of the absorption index

The absorption behaviour of double-heterojunction waveguides was characterised by measuring the response of straight waveguides or adding the light of the output waveguides of a 2×2 switch. The absorption coefficient can be calculated from the optical response by using

$$\Delta \alpha(U) = -\frac{1}{L} \cdot \ln \left(\frac{P(U)}{P(0)} \right) \quad (4.9)$$

for straight waveguides or

$$\Delta \alpha(U) = -\frac{1}{L} \cdot \ln \left(2 \frac{P(U)}{P_{cross}(0) + P_{bar}(0)} - 1 \right) \quad (4.10)$$

for 2×2 spaces switches. The length of the electrodes L is 5 mm for both devices.

Examples of electro-absorption curves are given in figure 4.3. These measurements clearly show that the absorption index in InP/InGaAsP is independent of the orientation with respect to the $[0\bar{1}1]$ in the (100) crystal plane. They also show that the electro-absorption depends on the polarisation of the optical mode.

The electroabsorption curves have been measured for energy distances to the bandgap between 91 and 181[meV] for the TE and the TM mode. The field induced absorption changes have been compared to the theoretical prediction calculated from equations (4.8), (3.23) and (4.2)

$$\Delta \alpha = C \cdot \frac{\mu_{TE/TM}}{\omega} \frac{E}{E_g - \hbar\omega} e^{-\frac{4}{3}\eta^{\frac{3}{2}}} \quad (4.11)$$

The parameters C , μ_{TE} and μ_{TM} have been obtained by fitting them to the experimental absorption responses. The measured values and the theoretical

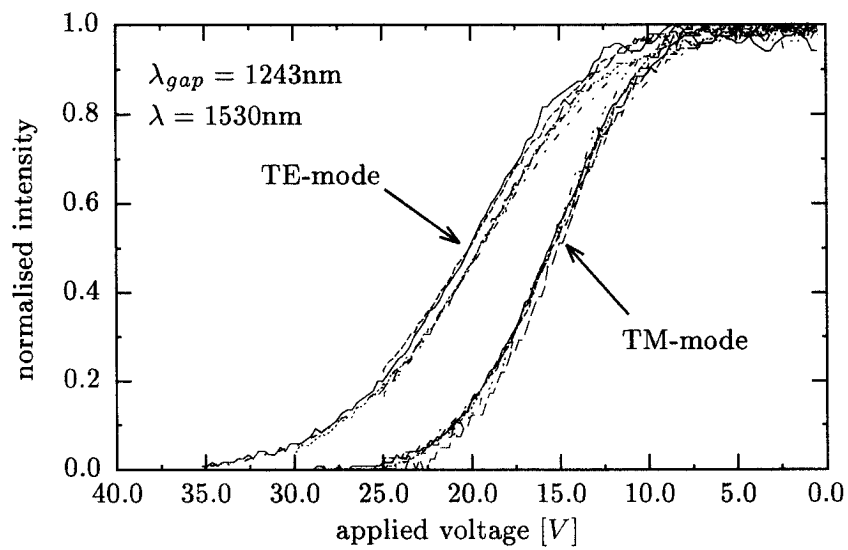
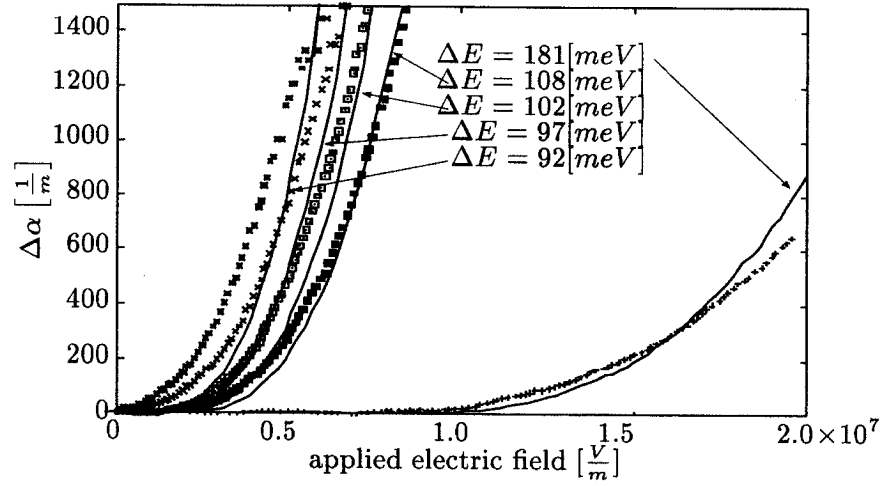
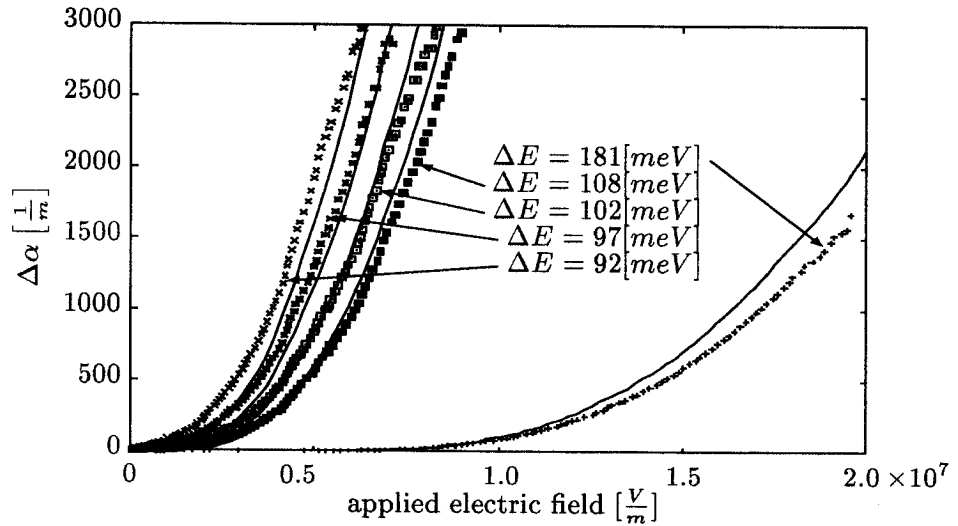


Fig. 4.3: Measured TE and TM electro-absorption curves at a wavelength of $1.53\mu\text{m}$ under different angles with respect to the $[0\bar{1}1]$ crystal axis. The bandgap energy of the guiding layer was $1.243\mu\text{m}$.



(a) Absorption index measured for the TE-mode



(b) Absorption index measured for the TM-mode

Fig. 4.4: Absorption index changes $\Delta\alpha$ (see equation (4.9)) measured for different energy differences of the optical mode to the bandgap (diamonds) compared to theoretical calculations using equations (3.38) and (4.8). The fit parameters were the effective electron mass μ and the constant R , defined by equation (3.23)

curves are shown in figure 4.4(a) for the TE and figure 4.4(b) for the TM mode. The experimental data fits quite well with the theoretical expectations. The fit parameter C has been found to be $4.8 \cdot 10^{24}$ and the effective electron masses for the TE $\mu_{TE} = 0.037m_e$ and $\mu_{TM} = 0.01m_e$. By comparing the obtained electron masses with published values, it follows that free electrons are the major contributors to electro-absorption.

4.3 Measurement of the field dependency of the refractive index

In a second experiment the refractive index change due to the Franz-Keldysh, Pockels, carrier effect and their polarisation dependency has been analysed by measuring the optical switching responses for applying voltages to the electrodes of 2×2 Mach-Zehnder interferometers oriented under a number of angles with respect to the $[0\bar{1}1]$ crystal axis. An example of these switching responses is given in figure 4.5 for an optical wavelength of $1.53\mu\text{m}$ and a bandgap wavelength of $1.25\mu\text{m}$. From these switching responses the phase-shift $\Delta\varphi$ and thereby the refractive index change Δn was computed.

4.3.1 Pockels effect

The Pockels-effect can be separated from the Franz-Keldysh effect and the carrier effect by using its $\cos 2\varphi$ dependency with respect to the crystal axes. It also affects only the TE polarised light (see figure 4.5). The Pockels and Franz-Keldysh effect were separated by fitting the function $a \cdot \cos(2\varphi) + b$ into the experimentally obtained refractive index changes $\Delta n(\varphi, V)$. The resulting $a(V)$ corresponds to the measured contributions of the Pockels effect.

In figure 4.6, the measured refractive index changes are plotted versus the applied effective electric field for optical wavelengths. It can be seen that the Pockels effect shows no dependency on the difference between photon and bandgap energy within the limits of error.

The electro-optic coefficient of the Pockels-effect in InGaAsP was obtained by fitting the function

$$\Delta n = -\frac{n^3}{2}r_{41}\Gamma\bar{E} \quad (4.12)$$

into the experimental data. The parameter Γ , which was calculated by numerical simulations, represents the fraction of the light under the ridge waveguide and \bar{E} stands for the optical mode weighted average of the electric

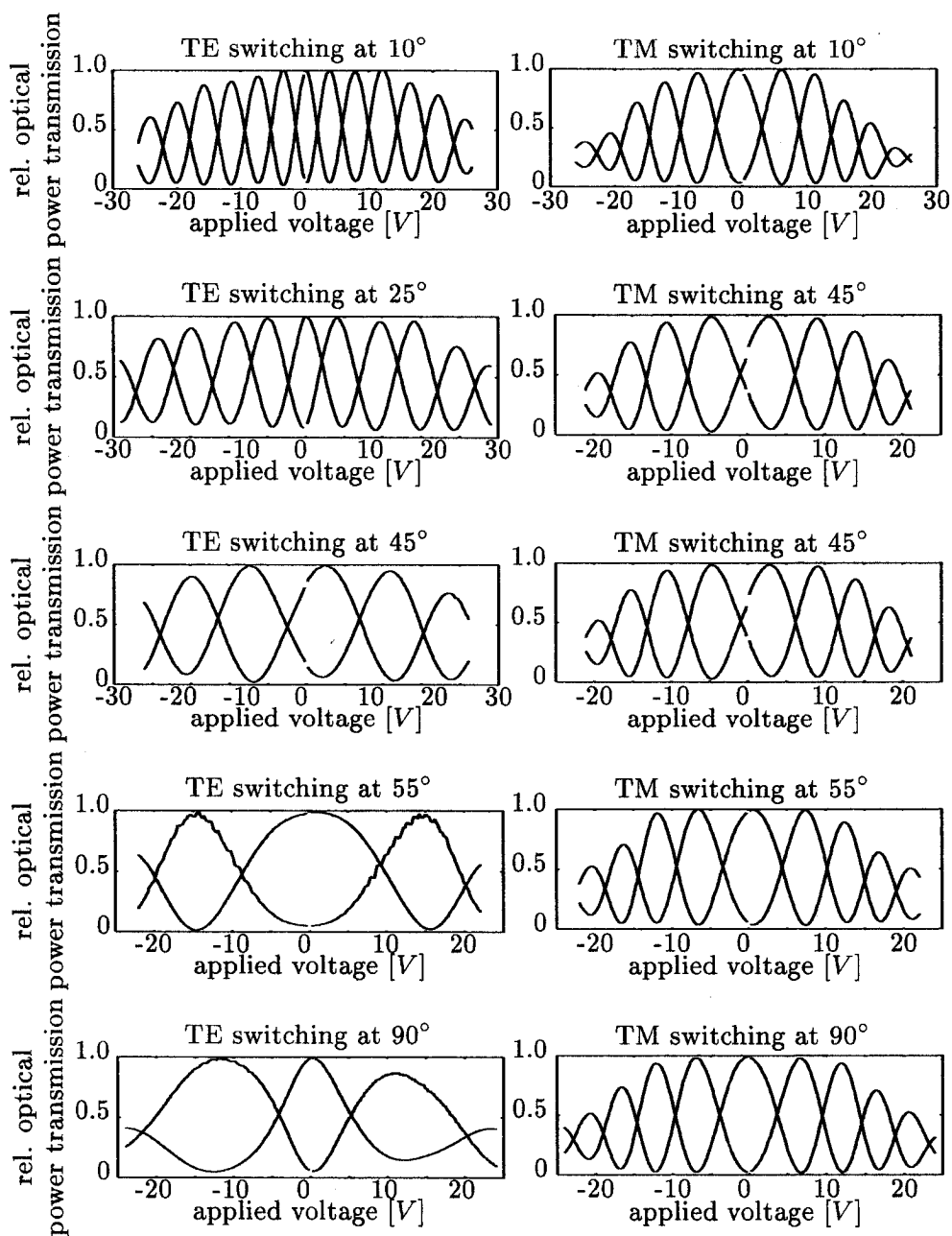


Fig. 4.5: Optical responses of Mach-Zehnder interferometric switches oriented under different angles with respect to the $[0\bar{1}1]$ axis. The optical wavelength was $1.53\mu\text{m}$ and the bandgap wavelength $1.25\mu\text{m}$

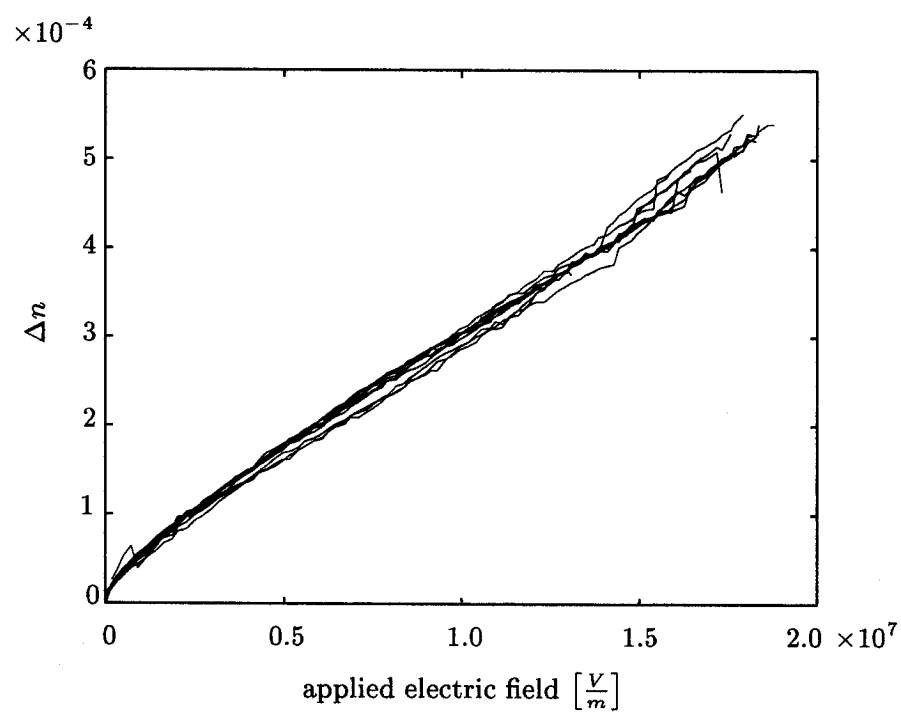


Fig. 4.6: Contribution of the Pockels-effect to the refractive index change, measured for optical wavelengths between 1460 and 1540nm corresponding to an energy difference to the bandgap between 143 and 187eV.

field. As two materials, InP and InGaAsP, contribute to the total refractive index change it is necessary to assume a value for the coefficient in one of the materials. Since the measurements show no dependency of the coefficient on the energy difference between photon and bandgap energy, it can be assumed that the coefficients of the Pockels effect are approximately the same in InP and InGaAsP. Under this assumption the electro-optic coefficient of the Pockels effect r_{41} has been found to be $1.47 \left[\frac{\text{pm}}{\text{V}} \right]$ which agrees well with values published in literature [53].

4.3.2 Franz-Keldysh and carrier effect

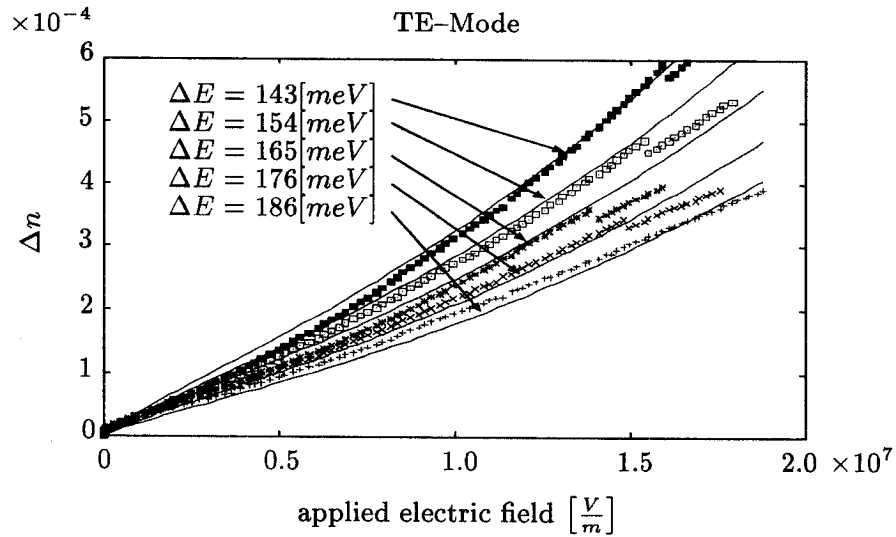
After the separation of the orientation dependent Pockels-effect the main contributors to the orientation independent refractive index change are the Franz-Keldysh effect and the carrier effect. These effects can be separated by making use of their different characteristics. Whereas the refractive index change due to the Franz-Keldysh effect is proportional to the square of the electric field, the contribution of the carrier effect is approximately proportional to the square root of the electric field. By comparison of the equations (2.24) and (3.58) one obtains for the total expected refractive index change in the material

$$\Delta n = \frac{\mu^{\frac{1}{2}}}{\omega^2} \cdot C \cdot \frac{|E^2|}{(E_g - \hbar\omega)^{\frac{5}{2}}} + \frac{n^3}{2} D(\omega) \cdot \Gamma \quad (4.13)$$

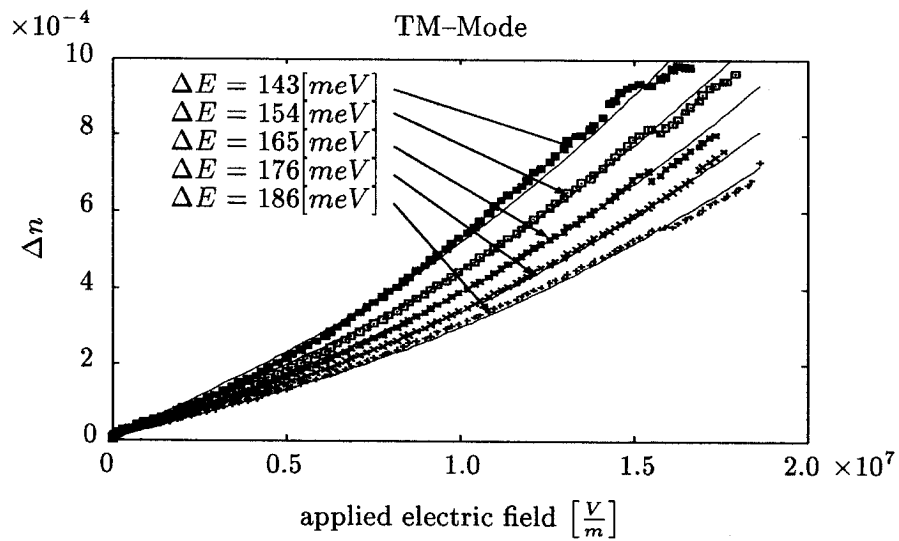
The parameter C summarises several physical constants including C_0 the approximately k -independent part of the matrix element [48, 38] and $D(\omega)$ the coefficient of the carrier effect

In a first step, the theoretical dependencies of the Franz-Keldysh effect and carrier effect on the electric-field were calculated numerically, taking the overlap of the electric field with the optical mode into account as described in section 2.5.1. These theoretical curves were subsequently fitted into the experimentally obtained values using C , μ and $D(\omega)$ as fitting parameters. The results of the fit are depicted in the figure 4.7(a) for the TE and in figure 4.7(b) for TM mode. The theoretical curves match the experimental data very well if C is chosen to be $5.2 \cdot 10^{-21}$ and the effective masses $\mu_{TM} = 0.037m_e$ and $\mu_{TE} = 0.01m_e$ found in section 4.2 are used.

In contrast to the Franz-Keldysh effect, the contribution of the carrier effect to the refractive index change required for a good fit cannot be described



(a) Refractive index change measured for the TE-mode



(b) Refractive index change measured for the TM-mode

Fig. 4.7: Measured contribution of the Franz-Keldysh effect and the carrier effect to the refractive index change (diamonds) and the theoretically expected curves (solid lines).

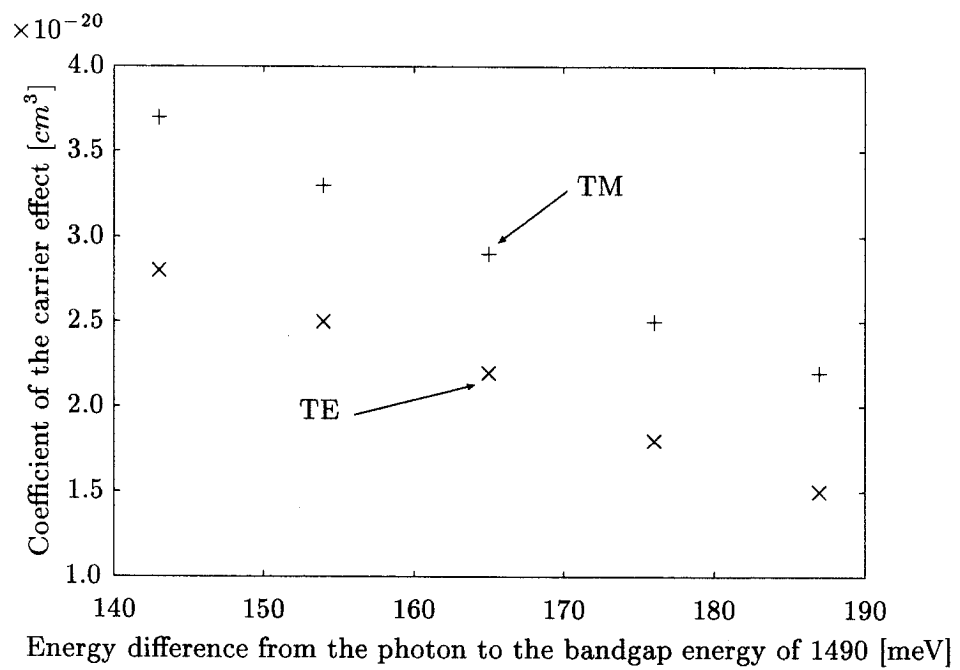


Fig. 4.8: Observed dependency of the coefficients of the carrier effect on the polarisation and energy detuning.

by a simple model of an electron gas as described in section 3.2. For an electron gas, we expect the contribution of the carrier effect to be inversely proportional to $\frac{1}{\omega^2}$. As shown in figure 4.8, experimental data, however, shows that the contribution of the carrier effect rises, as $\hbar\omega$ approaches the band gap energy. This clearly indicates that the band filling and band shrinkage effect play an important role [27] for the carrier concentration and distance to the bandgap used, rendering a theoretical description very difficult due to the nature of the effects involved.

4.4 Discussion

The accuracy of the parameters used for fitting the refractive and absorption index, extracted from the experimentally obtained switching curves, suffers from some uncertainty.

The main source of uncertainty is the exact value of the applied electric field, which has to be computed using a model of a pin-diode. Considering an uncertainty of $20nm$, due to variations over the wafer, and an uncertainty of the doping levels, especially the level in the not intentionally doped layer, an uncertainty of 4% of the electric field strength has to be expected.

The linear electro-optic depends on the angle of the waveguide with respect to the $[0\bar{1}1]$ crystal axis. Misalignment of the masks with respect to the crystallographic axis of 0.5 degrees adds 3.5% to the uncertainty of the results. The total uncertainty of the coefficient of the linear electro-optic r_{41} effect therefore add to $\pm 8\%$.

The coefficients R_{11} and R_{12} of the quadratic electro-optic effect contain an error of 8% from the uncertainty of the electric field. These coefficients also depend strongly on the photon to bandgap energy difference. Thus band gap variations developing during epitaxial layer growth, typically $20nm$ over the wafer, induce an additional uncertainty of 15% of the coefficients at a given energy difference.

The coefficients of the plasma effect depend on the photon and bandgap energy. The coefficient of the carrier can be determined within 10%, but it has to be noted that at high carrier concentrations other effects also become relevant. Due to the complex nature of the carrier effect and the absence of a sufficient amount of experimental data, no general statement about the behaviour of the carrier effects can be made.

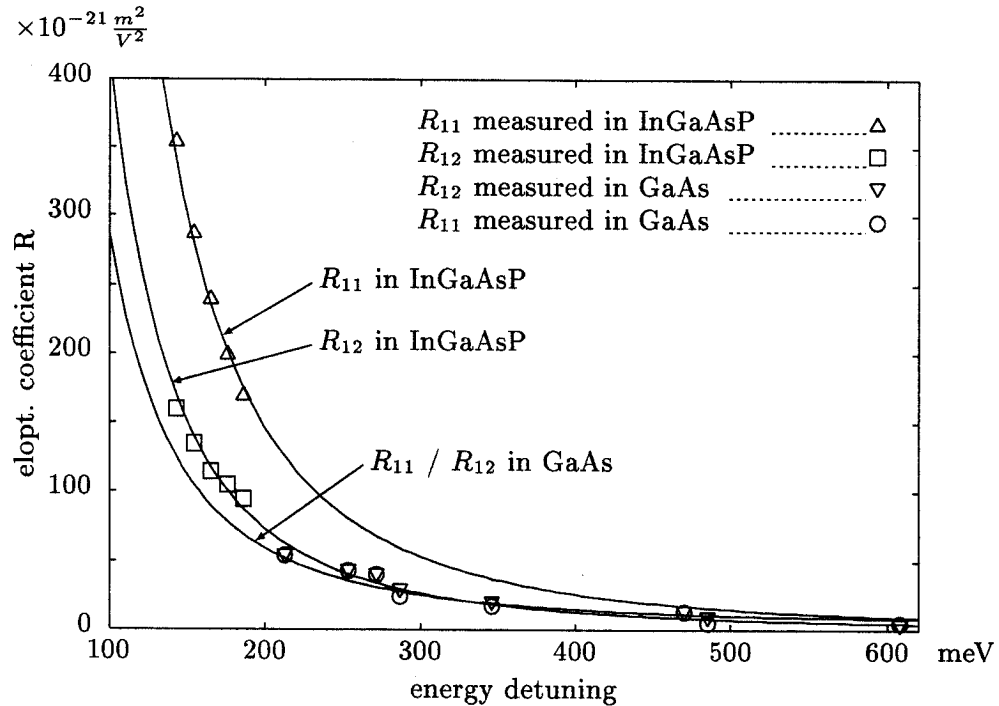


Fig. 4.9: Observed and theoretically predicted dependency of the coefficients of the Franz-Keldysh effect on the polarisation and energy detuning in InGaAsP and GaAs. The values in InGaAsP were determined in this thesis, the values in GaAs can be found in publications [54].

4.5 Summary and Conclusion

In this chapter the field induced index changes in InGaAsP/InP double heterojunction waveguide structures were theoretically and experimentally examined for the TE and TM polarised light, a number of photon to bandgap energy differences and directions of waveguide, using 2×2 Mach-Zehnder space switches. The experimentally obtained data fits very well with the theoretical predictions.

As described in detail above in section 3.4 the Franz-Keldysh effect is a field enhanced absorption effect. The electric field deforms the band structure of the material. This allows the tunnelling of carriers from the valence band to the conduction band through a triangular barrier (see also figure 3.2). The increased tunnelling probability in the presence of an electric field increases

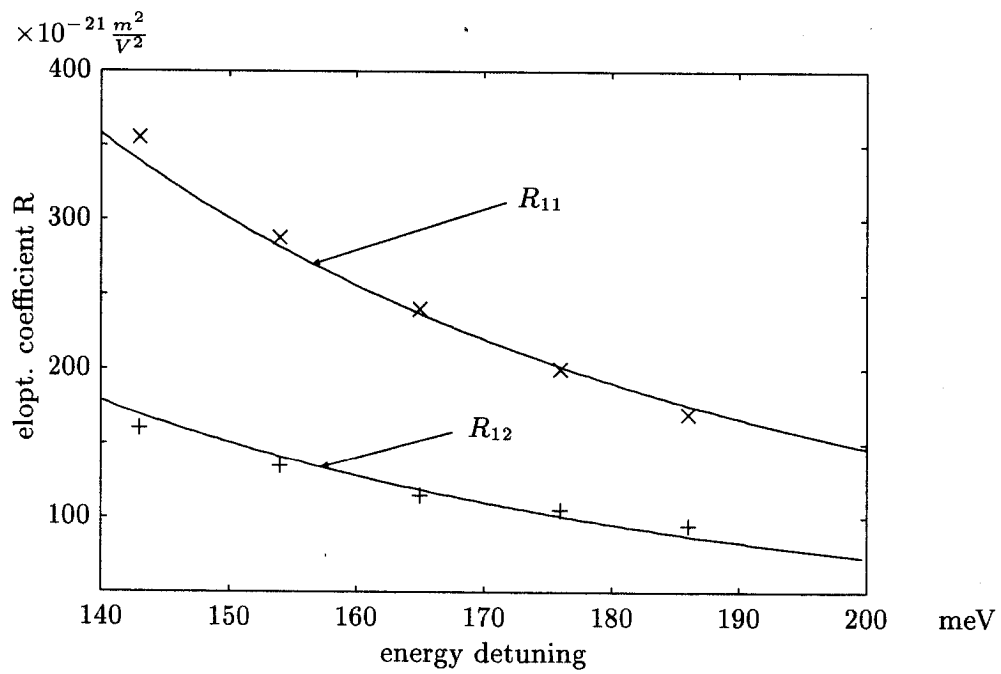


Fig. 4.10: Observed and theoretically predicted dependency of the coefficients of the Franz-Keldysh effect on the polarisation and energy detuning in In-GaAsP.

the absorption coefficient of the material and thereby also changes the refractive index. The tunnelling probability can be calculated by solving the Schrödinger equation for an electron hole pair in the presence of an electric field (equation 3.18)

$$\left(\frac{\hbar}{2\mu_x} \frac{\partial^2}{\partial x^2} + \frac{\hbar}{2\mu_y} \frac{\partial^2}{\partial y^2} + \frac{\hbar}{2\mu_z} \frac{\partial^2}{\partial z^2} + e \cdot \vec{E} + E \right) \phi(\vec{r}) = 0$$

The exact solution to this equation involves Airy-Functions [49]

$$\phi(\vec{r}) = C_x C_y C_z \text{Ai}(-\xi_x) \text{Ai}(-\xi_y) \text{Ai}(-\xi_z)$$

Using this solution the absorption index change and refractive index change can be calculated as outlined in section 3.4. For the absorption index change the relation

$$\Delta\alpha = C \cdot \frac{\mu}{\omega} \frac{1}{E_g - \hbar\omega} \cdot e^{-\frac{4}{3}\eta^{\frac{3}{2}}}$$

and for the refractive index change the relation

$$\Delta n = \frac{\sqrt{\mu}}{\omega^2} \cdot D \cdot \frac{|E^2|}{(E_g - \hbar\omega)^{\frac{5}{2}}}$$

is obtained. It can clearly be seen that the electro-absorption and the refractive index change increases very rapidly as the energy detuning $E_g - \hbar\omega$ decreases.

The values for C , D and μ were determined by fitting the theoretical predictions into the experimental data. By using the data for electro-absorption the value for C was found to be $4.8 \cdot 10^{24} [\frac{s}{kgm}]$ and the effective mass μ was found to be $0.037m_e$ for TE and $0.01m_e$ for TM polarisation. Thus electroabsorption is 3.7 times higher for TM polarisation.

In contrast to the electro-absorption the equation for the refractive index change does not allow to separate the parameter D from the effective mass μ . Therefore the values for μ found from fitting the values of the electro-absorption were used and only D was used for the fit. The resulting value of $5.2 \cdot 10^{-21} [\frac{m^7 V^2}{s}]$ fits very well for TE and TM polarised light (see figure 4.10).

The values of R_{11} and R_{12} measured in InGaAsP were also compared to values for GaAs published in literature [54, 55, 56, 57] (see figure 4.9).

It can be seen that the coefficients of the coefficients in GaAs match the theoretical predictions quite well and go well together with the values found in InGaAs. However it has to be noted that the polarisation dependency of the Franz-Keldysh coefficients in InGaAsP and GaAs is different. While the Franz-Keldysh effect in GaAs is nearly polarisation independent, it is almost twice as strong for TM polarised light in InGaAsP.

The linear electro-optic (Pockels) shows a $\cos 2\varphi$ dependency relative to the $[0\bar{1}1]$ crystal axis and affects only the TE-mode. Its coefficient has a constant value of $1.47[\frac{pm}{V}]$ over the observed wavelength range.

Finally, the change of the free carrier concentration contributes to the refractive index change. Although it is a side effect, compared to the Pockels and the Franz-Keldysh effect, its contribution cannot be neglected for low electric field strengths. Its contribution to the refractive index change and wavelength dependency have been measured (see also figure 4.8). The complex nature of the carrier effect, however, prevents a general description of this effect.

From the results described above it follows that an energy detuning of less than 150 [meV] is impracticable for electro-optic space switches due to the rapid and polarisation dependent increase of electroabsorption. Polarisation independent operation of electro-optic switches can be achieved by combining the Pockels and the Franz-Keldysh effect by choosing the correct angle of the waveguides with respect to the $[\bar{1}10]$ crystal axis. The exact angle depends on the energy detuning and on the shape of the waveguides. For the switches implemented in this thesis this angle is approximately 35 degrees.

5. DESIGN AND LAYOUT OF A TRANSCEIVER CHIP FOR PASSIVE OPTICAL NETWORKS

The most important advantages of semiconductor based electro-optic modulators over modulators based on other materials is their potential to integrate multiple components into a single chip. To demonstrate the feasibility of such an integration, a transceiver chip, intended for the use in passive optical networks, featuring a monolithically integrated modulator and photodetectors, has been designed and manufactured. To motivate the design of this device, this chapter gives a short overview of the concepts of passive optical networks. Subsequently, the design of this transceiver chip and the integrated components, such as tapers, photodetectors, multi-mode interference couplers, modulators, are discussed in detail. Afterwards the manufacturing process of the transceivers are described in detail and experimental results are presented.

5.1 *Introduction*

Bringing optical fibres to the customers is an elegant way to provide high speed access to networks. If optical networks are to penetrate to small business and private customers, these networks have to be able to compete with the copper wire [16]. Fibre optical networks will always bring more bandwidth and communication capacity. They will however have to become as cost effective as copper wire based systems, or offset the additional costs through extra revenues.

The most expensive parts in electro-optic equipment are the chips themselves and the fibre to chip interfaces. While the chip costs can be expected to fall as the manufacturing technology advances, fibre to chip interfaces will probably always remain expensive due to the stringent alignment tolerances. Therefore the number of fibre to chip interfaces has to be minimized. This can be achieved by monolithic integration of multiple components into a single chip and a single package with one fibre in- and output. This type of chips, which are capable of transmitting and receiving data, are called "transceiver chips".

To demonstrate the feasibility of the integration of a multiplicity of components into a single chip, a transceiver chip intended for the use in subscriber terminals of passive optical networks has been designed and manufactured. It features monolithically integrated waveguides, modulators, photodetectors, power splitters and mode shape adapters. For a better understanding of the design consideration a short overview over (passive) optical networks is given below.

5.1.1 *Optical Networks*

The most simple approach to bring optical fibres to the customers, which is equivalent to currently used copper wire networks, uses one or two dedicated fibres for each customer. It has the advantage of high security and privacy, high capacity and allows simple equipment on the customers premises. Due to the high costs associated with the installation, maintenance and optical components however, this option is rather uneconomic for private or small business utilisation. The costs of optical components and deployment of fibres are too high by far for private and small business users. This problem can be overcome by sharing the large bandwidths offered by single-mode optical fibre

systems among several customers and taking provisions that this systems can be upgraded easily if required later on.

The most promising network structures currently under consideration are multi-star networks with active or passive nodes and star-bus systems. These network structures share resources by concentrating the traffic towards the larger nodes. Active node multi-star networks have the advantage of being able to provide a large range of services and good privacy for the customers with comparatively simple optical components. On the other hand they require electric power to perform their task, causing additional expenses for feeding cables and issues associated with outdoor electronics. It is furthermore not possible to upgrade active nodes easily if a much higher bandwidth is required.

5.1.2 *Passive optical networks (PONs)*

To avoid the issues associated with out-stationed electronics, it has been proposed to replace all active nodes with fully passive ones. Possible components for these passive nodes are power splitters or wavelength division multiplexers (WDMs). Also the use of a combination of power splitting and WDM techniques is possible. Furthermore, different techniques and network architectures for the up- and downstream data channels can be used if desired.

For networks based on power splitting, a high degree of resource sharing can be achieved and the number of components required in the central office can be greatly reduced. However, more sophisticated electronic circuits are required for the customers terminal equipment to deal with timing problems and to separate the data streams for the different customers [58]. This, however, will most likely not increase the cost of these terminals especially if they are produced in large volumes. The privacy of the customers can be preserved by using encryption technologies. Provided that the customer terminals are equipped with optical filters, passive optical networks based on power splitting can be easily upgraded by simply adding additional wavelengths to provide extra services with minimal interruption. Only those customers, who want to make use of the extra services need to upgrade their terminal equipment. Even if only one wavelength is used multiple analog and digital channels can be transmitted using subcarrier multiplexing. Furthermore, the requirements concerning the wavelength accuracy and stability of the optical power sources are not very stringent. Thus, comparatively cheap Fabry Perot laser sources are sufficient. The main disadvantages of power splitting are a lower available

bandwidth per user, as the bandwidth of a channels is shared among certain number of users, and a tighter power budget.

Passive optical networks based on WDM technology are more flexible due to the fact that every customer can use a dedicated wavelength and is therefore independent of the other subscribers, but also more expensive since more laser sources are required. Modern dense WDMs can support 20 channels or more. Therefore, laser sources with a stable wavelength and narrow linewidth, such as thermally stabilised DFB lasers, matching the wavelengths of the WDM are required. As each customer receives only the data modulated on his wavelength security and privacy is ensured. Furthermore, the data rate for each customer can be selected individually, allowing easy upgrade if desired.

5.1.3 *Terminal equipment in passive optical networks*

The technology used for the network terminals at the customers premises is premises depends strongly on structure of the passive optical network and is critical for its performance. During the last years, a number of optoelectronic devices for the use in passive optical networks have been proposed and implemented.

Devices with integrated lasers and photodetectors [59, 60, 61, 62] are well suited for networks using power splitting at the remote nodes for distribution as the active light sources relax the power budget which is inherently strained by the power splitting approach. For networks based on WDMs with narrow channel spacing (i.e. the channels are separated by $1nm$ or less), the requirements regarding the wavelength accuracy and stability of the laser are very stringent because they have to match wavelength of the WDM channel exactly. Such stringent requirements can only be met by temperature stabilised DFB lasers, which are very costly and therefore not yet an attractive option, not to mention the issues associated with the temperature stabilisation under uncontrolled environmental conditions at the customers premises.

Reflective semiconductor optical amplifiers (SOAs) are interesting candidates for transceivers. They can be operated as transmitters and photodetectors [63, 64, 65]. For transmission a signal can be modulated on light transmitted from the central office by modulating the gain via the injected current of the SOA. To receive an incoming signal the SOA is used as a photodetector. Reflective SOAs are an attractive option because they are small, and they allow high on-off ratios and low losses or even gain and they require little or no cooling. Furthermore, the reflected light has inherently exactly

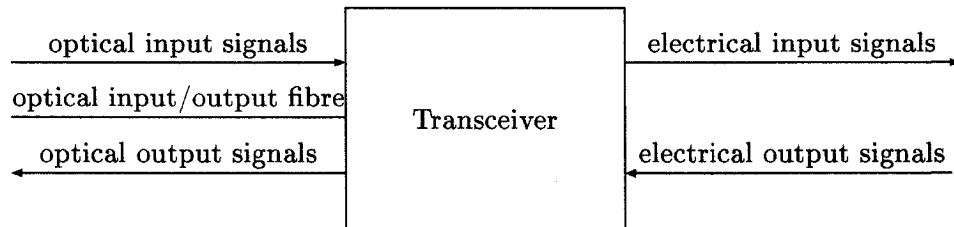


Fig. 5.1: Functional diagram of a transceiver. A transceiver converts optical input signals into electrical signals and electrical input signals are modulated onto an optical carrier

the same wavelength as the transmitted light which is important for WDM based passive optical networks. On the other hand the electronics required to switch between the transmission and reception mode reduce the sensitivity of the receiver. Additionally some time is required to switch between the amplifier and the photodetector mode to charge and discharge the junction of the SOA resulting in a loss of bandwidth which can be a serious problem in networks using power splitting and time division techniques, even though some effort has been made to reduce this switching time [66, 67]. It has also be noted that reflective SOAs cannot be operated in the full duplex mode, i.e. transmission and reception at the same time.

The issues of the switching time between reception and transmission mode can be avoided by integrating photodetectors and reflective modulators, while preserving the advantages of the reflective SOAs with the exception of the signal amplification SOAs are capable of. Reflective modulators normally loose more light than reflective SOAs but are on the other hand in principle capable of full duplex operation [68, 69, 70] and do not require time to switch between transmission and reception mode. For stable operation of SOAs the ambient temperature has to be controlled. This is especially difficult as it is not possible to control the environmental conditions at the customers premises. In order to obtain a high reliability, it is therefore best to leave sensitive devices such as lasers in a central office where the environmental conditions are more favourable. Cost effective reflective electro-mechanic modulators [71] have been demonstrated successfully.

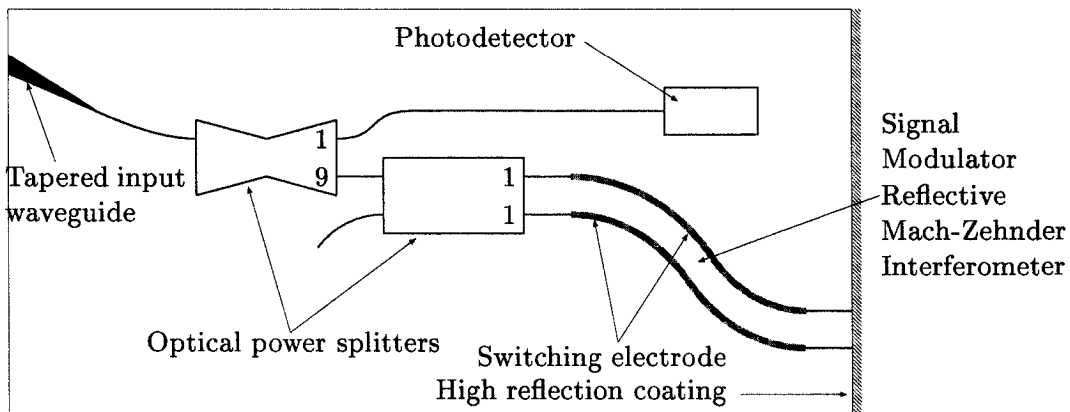


Fig. 5.2: Schematic layout of the implemented transceiver chip for passive optical networks

5.2 Concept and design of the transceiver chip

A transceiver chip is the key component in the terminal equipment of passive optical networks. It converts incoming optical signals into electrical signals for reception and electrical signals into optical signals for transmission of data. The same optical fibre is used for the incoming and outgoing optical signals as depicted in the schematic in figure 5.1.

To manufacture such a transceiver chip a technique allowing the integration of low loss optical structures and strongly absorbing regions has to be developed. Additionally care has to be taken to avoid back reflection at the fibre to chip interface. Any back reflected light reduces the overall on-off ratio of the transmitted signal substantially; e.g. with a fibre to fibre loss of 10 dB, a residual reflectivity of only 1% will limit the on-off ratio to 10 dB at best. Furthermore mode shape adapters have to be integrated to minimize the optical losses at the fibre to chip interface and to ease the alignment tolerances. As the chip size is comparatively small, a process, allowing to manufacture these mode shape adapters in arbitrary locations on the wafer, has to be developed.

In passive optical networks power to operate the network units has to be applied locally and a minimum of services has to be provided even during power outages, the terminal equipment should consume as little power as possible to allow a long lifetime of necessary backup batteries. Furthermore, the

devices should feature low optical losses, high optical and signal bandwidth, polarisation insensitive operation and sensitive photodetectors (see figure 5.2).

To meet all these requirements, an InP/InGaAsP based transceiver chip was designed with all electro-optic components integrated. It features mode shape adapters to minimize coupling losses to single mode lensed fibres and to relax the fibre alignment tolerances, a tap to extract 10% of the incoming light for detection in an evanescent coupled photodiode with a bandwidth in the gigabit range and a reflective Mach-Zehnder interferometric modulator to remodulate the incoming light. The arms of the Mach-Zehnder interferometer are oriented under an angle of 32 degrees to achieve polarisation insensitive modulation. Polarisation insensitive operation over a wavelength range of 20–30nm is ensured by using multi mode interference couplers as optical power splitters and combiners. The fibre to chip coupling losses are minimized by integrating mode shape adapters and applying an anti-reflection coating. Residual back reflected light from the chip facet can seriously degrade the on-off ratio of the modulator. The input-output waveguide is therefore tilted by 7 degrees to prevent light from being back reflected into the fibre. In the following, a detailed description integrated optical components is given.

5.2.1 Ridge waveguides and electro-optic modulators

To implement the transceiver chip a double hetero-structure ridge waveguide structure was chosen. The layer structure and doping levels are depicted in figure 5.3. This structure was chosen because it allows for low optical losses while maintaining good guiding properties, highly efficient phase shifters and its ease of fabrication. In the following, the design considerations will be presented.

Electro-optic effects are utilised to modulate the back reflected light. The necessary electric fields are generated by reverse biasing a pin-diode structure. A pin-diode structure has been chosen because it allows high switching efficiencies, i.e. high refractive index changes with small changes of the applied voltage, while minimizing free carrier induced losses. As the switching efficiency increases with decreasing thickness of the intrinsic layer, a tradeoff has to be found between a high switching efficiency and low carrier absorption losses. Accordingly, an intrinsic guiding layer thickness of 600 nm and low doping levels ($2 \cdot 10^{17} [\frac{1}{cm^3}]$ for the n-type and $5 \cdot 10^{16} [\frac{1}{cm^3}]$ for the p-type material) have been chosen. Published values in literature [72, 73] indicate that the absorption in p-type material is 10 times higher than in n-type material.

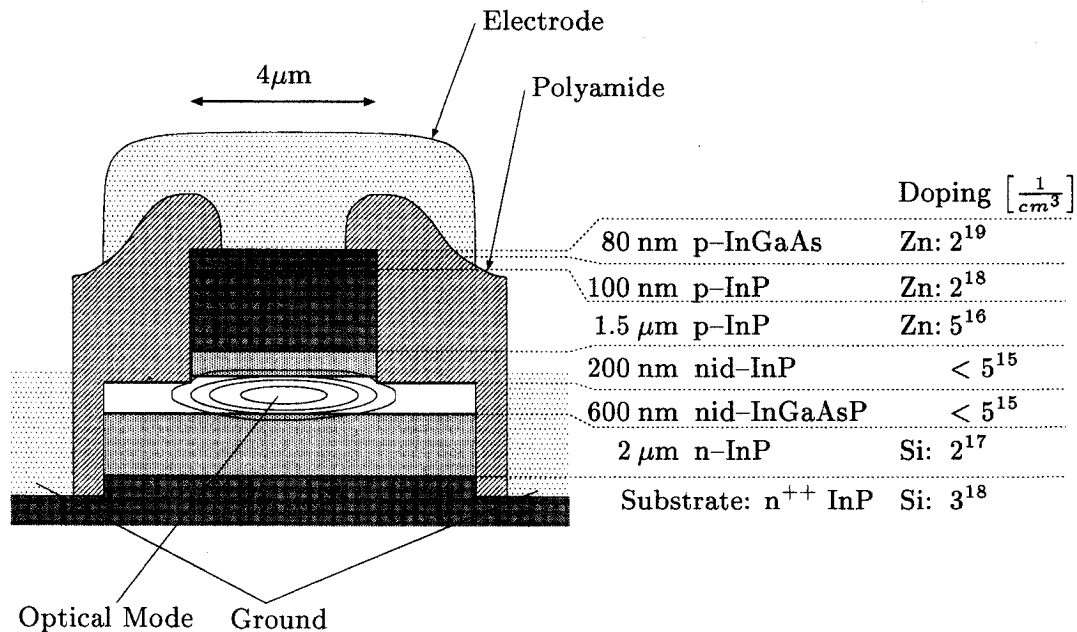


Fig. 5.3: Cross-section through the switching electrode

To reduce absorption further, a 200 nm thick undoped InP spacing layer has been inserted between the guiding and the p-doped layers.

To achieve polarisation insensitive switching, the arms of the Mach-Zehnder interferometer were tilted on average by an angle of 32 degrees with respect to the $[0\bar{1}1]$ crystal axis. The electrodes of the modulator are 5mm long, which allows for low switching voltages.

Sources of optical losses in double hetero-structure ridge waveguides are absorption in the guiding layer, absorption by free carriers, scattering from film inhomogeneities, surface roughness and radiation losses in curved waveguide sections. To minimize absorption losses in the film, it is necessary to use a bandgap energy as far away from the photon energy as possible as absorption increases rapidly when the photon energy gets close to the bandgap (see sections 3.4.1 and 4.2). On the other hand the electro-optic coefficients influencing the refractive index in the presence of electric fields decrease with increasing bandgap to photon energy difference. Therefore, a compromise must be made between high switching efficiency and low losses. A energy separation of 200 meV was chosen because the switching efficiency is still reasonably high and the losses sufficiently low.

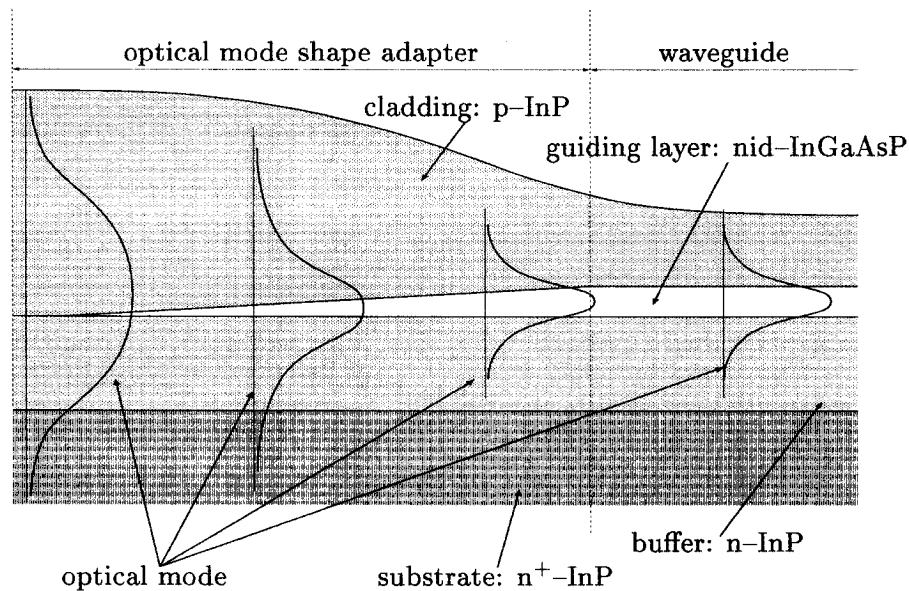


Fig. 5.4: Cross section through an integrated optical mode shape adapter consisting of a slowly tapered down InGaAsP waveguide layer and an up tapered InP cladding layer. The mode in the tapered guiding layer expands adiabatically to match the mode of a single mode fibre.

Another source of losses is scattering on surface roughness. While the quality of the epitaxial layer growth is good, side roughness of waveguides from dry etching processes is an issue especially as the refractive index contrast semiconductor to air is much higher than the refractive index contrast guiding layer to cladding. This scattering losses increase with increasing etch depth and decreases with increasing ridge width [74]. Thus the ridge has to be made as wide as possible while remaining single mode and the etch depth should be minimized. The ridge width was chosen to be 3 microns for normal waveguides and 4 microns for the phase shifters to relax the adjustment tolerances. The waveguide was etched 100 nm into the guiding layer. This is a good compromise between low scattering losses and good lateral confinement.

5.2.2 Optical mode size adapters

The waveguide structure described above has been optimised for low losses and highly efficient switching. The resulting mode sizes are very small, typi-

cally $3 \times 1 \mu m^2$, compared with single mode fibres, which guide a circular mode with 8 to 10 μm diameter. The large mode-size differences result in coupling losses of 7 to 10 dB per fibre chip interface. In addition the stringent adjustment tolerances due to the small mode size of the waveguides makes the fibre adjustment difficult. To reduce the coupling losses between waveguides and single mode fibres, micro lenses [75] and lensed fibres [76] have been used successfully, however without solving the problem of the strict alignment tolerances. To ease the alignment tolerances and to reduce the coupling losses to single mode fibres, mode shape adapters have been integrated into chips [77].

We chose to implement the mode shape adapters developed by T. Brenner [78]. A schematic of the structure is shown in figure 5.4. It consists basically of a guiding layer tapered slowly to zero thickness and an up tapered cladding layer. The width of the ridge is simultaneously expanded from 3 to 7 microns. As the optical mode travels towards the tapered down end, it expands adiabatically as the guiding layer becomes thinner. Numerical calculations using the beam propagation method (BPM) [79] show that the tapered section has to be at least 500 microns long to allow adiabatic expansion. The same applies for light coupled from the fibre into the chip. In the section between the chip facet and the tip of the guiding layer the light is guided by the $n-n^+$ interface of the substrate to cladding layer. Using these tapers, optical coupling losses to lensed single mode fibres as low as 0.5 to 1.0 dB can be obtained and the alignment tolerances are relaxed to 2 microns.

5.2.3 Optical 3dB power splitters

The performance of Mach-Zehnder type interferometric modulators depends strongly on the properties of the power splitters and combiners used. We have chosen to use multi-mode interference couplers (MMIs) because they can be made polarisation insensitive, have low losses, have a wide optical bandwidth [80], are very compact [81, 82], are relative insensitive to fabrication tolerances [22] and can be easily integrated with waveguides. Other types of power splitters/combiners such as directional couplers or Y-branches are either polarisation or wavelength sensitive or both and are susceptible to process tolerances. Multimode interference couplers have proven their favourable properties in a wide range of applications, for instance in polarisation insensitive switches [83, 84], phase-diversity networks [85, 86] and semiconductor ring lasers [87].

MMIs are based on the self-imaging properties of periodic objects illumi-

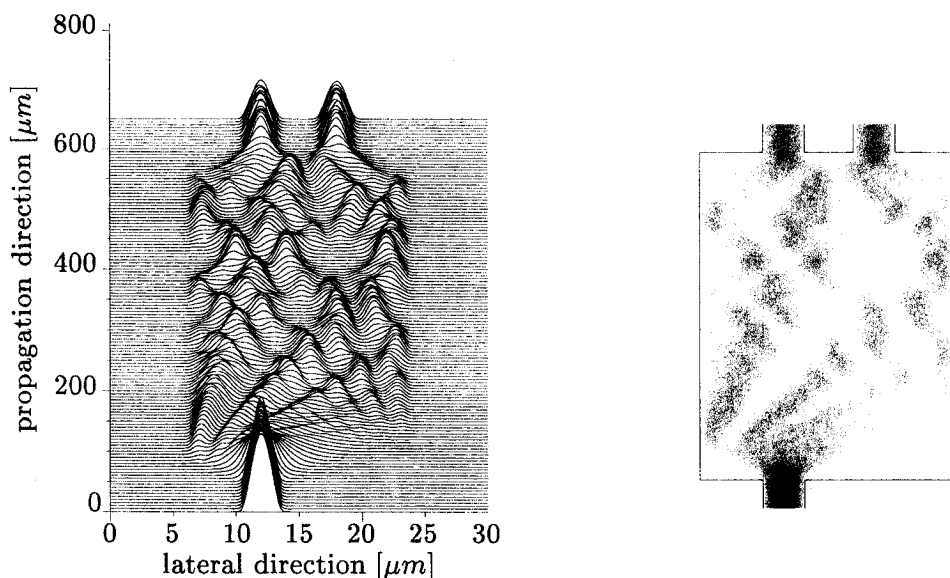


Fig. 5.5: Surface (left) and contour plot (right) of the simulated light intensity distribution in a 3dB power splitting multi mode interference coupler

nated with coherent light [88, 89]. They consist of a broad waveguide into which light is coupled. The incoupled light excites a series of eigenmodes in the MMI section propagating with different velocities. After a well defined propagation length $L_N^M = \frac{3L_c M}{N}$, the incoupled light field is reproduced N fold by interference of the propagation eigenmodes. The coupling length $L_c \simeq \frac{4nW^2}{\lambda}$, where W is the effective width of the MMI, is defined as the coupling length of the 0^{th} and the 1^{st} eigenmode. The theoretical details can be found in the literature [89, 23, 90].

The 2×2 MMI implemented uses the same layer structure as illustrated in figure 5.3 and is a restricted type. It has been simulated using the effective index and beam propagation method [79] with the results of the equations mentioned above as a starting point. The light field distribution found by the simulations are depicted in figure 5.5. The optimum dimension found are $550 \times 17.4 \mu\text{m}^2$ with the centres of the input/output waveguide 6 microns or $\frac{1}{3}$ of the effective width of the waveguide apart. The guiding layer was etched 100 nm deep and 300 nm at the sides of the MMI to increase the fabrication tolerances with respect to the etch depth and to reduce the polarisation dependence due to different mode confinement.

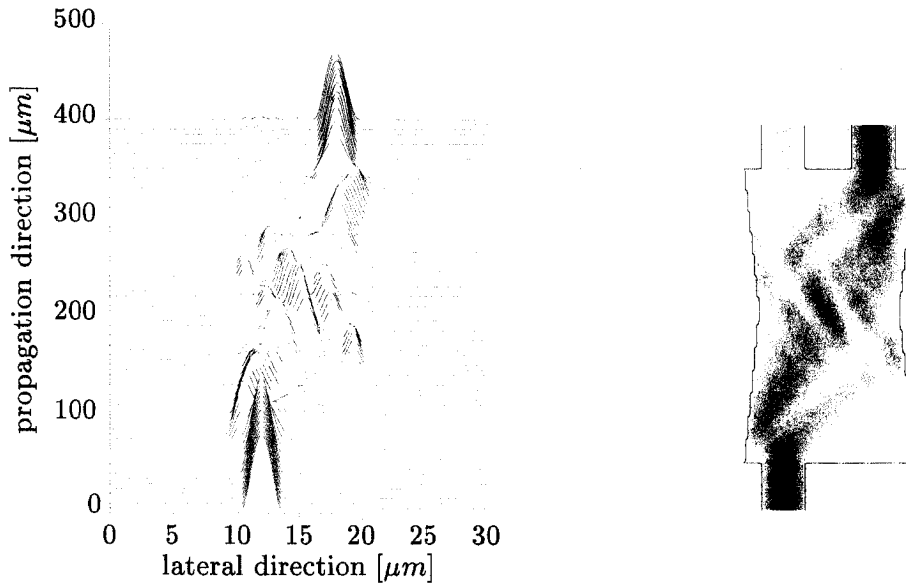


Fig. 5.6: Surface (left) and contour plot (right) of the simulated light intensity distribution in a 3dB power splitting multi mode interference coupler

5.2.4 Optical 1:9 power splitters

To extract a small part (10%) of the incoming light for detection in the photodiode, a tap device is required. A MMI coupler was chosen due to its superior over alternative types of power splitters as described in the previous section and the possibility to choose the splitting ratio freely [91]. Arbitrary splitting ratios can be obtained by using so called “butterfly MMIs”.

In the middle of a conventional MMI twice the numbers of self images appear. The MMI can therefore be split mentally into two sections. By introducing a phase shift between the output of the first section and the input of the second section, the ratio of the output power of the self images at the end of the second section is changed. This phase shift is generated by linearly up- and down-tapering the MMI sections.

To obtain a splitting ratio of 9:1, we start from an MMI of the length $L_4^1 = \frac{3L_c}{4}$ with input waveguides placed at the first and third quarter of the width of the MMI, where restricted interference already leads to a splitting ratio of 85:15. By tapering down the MMI towards its middle, a splitting ratio of 9:1 is finally achieved. The device parameters were initially calculated

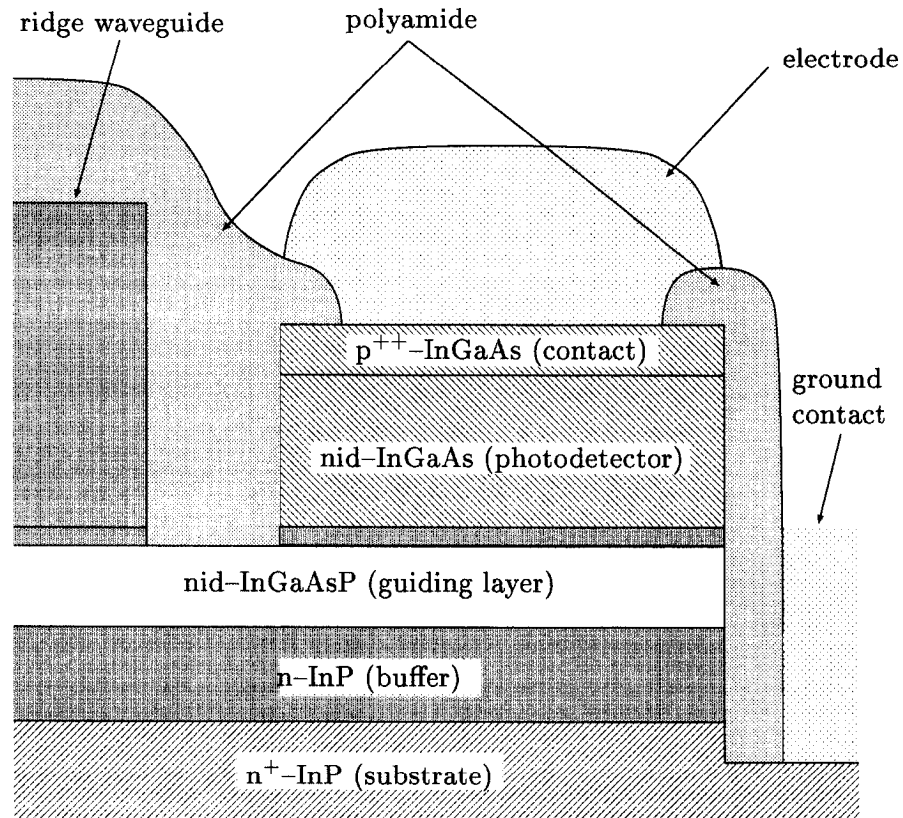


Fig. 5.7: Cross section through an evanescent coupled pin-photodiode integrated with a waveguide.

using the analytical formulas given in [91] and refined afterwards numerically by using a combination of the beam propagation method and the refractive index method. Accordingly the device width and length were chosen to be $10.4 \times 304 \mu\text{m}^2$ with a minimal width of $8.4 \mu\text{m}$ in the middle and the centres of the input/output waveguides placed $3 \mu\text{m}$ from the centre. The simulated light field is shown in figure 5.6. Analogous to the 1:1 splitting MMI described in the previous section, the guiding layer was etched 100 nm deep except at the sides of the MMI to reduce the polarisation sensitivity and increase the fabrication tolerances with respect to the etch depth.

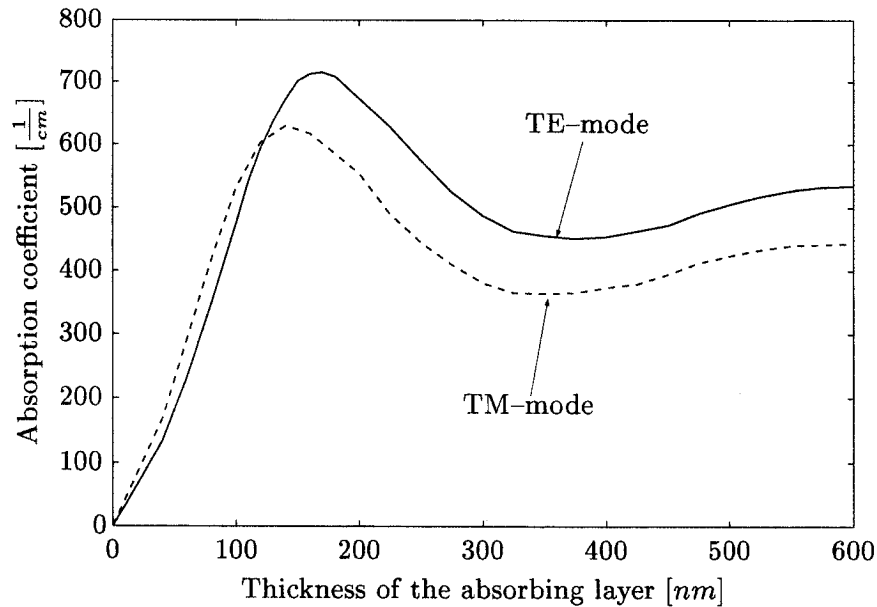


Fig. 5.8: Calculated absorption constant using the beam propagation method of the evanescent field coupled waveguide photodiode versus the thickness of the absorbing InGaAs layer plotted for the TE- and TM-polarisation.

5.2.5 Waveguide photodetectors

To receive downstream data, photodetectors are necessary. Evanescent field coupled waveguide photodetectors are very suitable devices because they are comparatively easy to integrate with waveguides and allow high waveguide to detector coupling [92, 93]. The evanescent field waveguide photodiode implemented consists of an InGaAs photodiode placed on top of an InP/InGaAsP double hetero-structure waveguide. A schematic cross section of a waveguide with an integrated photodetector is shown in figure 5.7.

Important for the design of waveguide photodetectors is the knowledge of the absorption per detector length typically given in dB/cm or dB/ μm . The absorption depends on the thickness of the spacing layer between the guiding InGaAsP layer as well as on the thickness of the absorbing InGaAs layer. It can be calculated using the eigenmode analysis [94] or the BPM method [95, 96]. For thin absorbing layers, the eigenmode method can yield absorption indices which can be much too high because it neglects multimode interference effects [97]. The beam propagation method is expected to yield more accurate

results and was therefore chosen to calculate the absorption constant (figure 5.8). The values of the real and imaginary part of the refractive index in InGaAs at an optical wavelength of $1.3 \mu\text{m}$ are $n = 3.65$ and $k = 0.25$ [98]

To avoid the resonance peak of the absorption index, and especially the absorption minimum after the resonance peak, a 420 nm thick layer of InGaAs, of which 370 nm are not intentionally doped, and the remaining 50 nm are highly doped to achieve a good ohmic contact, was chosen as the absorber. An undoped spacing layer of 200 nm InP was inserted between the guiding and the absorbing layer for technological reason in the manufacturing process. With an absorption constant of approximately $400 \frac{1}{\text{cm}}$, a detector length of $100 \mu\text{m}$ is required to detect 99% of the incoming light. As the required speed of the photodetector is only 622 MHz, speed is not an issue. The length of the waveguide photodetector implemented is $216 \mu\text{m}$ long to be of the same size. Accordingly, a width of $40 \mu\text{m}$ is required to allow free propagation of the light in the photodetector.

5.3 Fabrication process sequence

This section gives a description of the process developed to manufacture the transceiver chip described above. The key issues solved were the monolithic integration of waveguides and photodetectors and the integration of mode shape adapters in arbitrary locations on the wafer.

The manufacturing process can be split into four main steps. In the first step, the layer structure for all components is grown and defined by a carefully designed sequence of metal organic vapour phase epitaxy (MOVPE) growth steps, wet chemical etching and a selective area regrowth. In a second step, the waveguides are structured using dry etching techniques and the electrical contacts were formed. The photodetectors are uncovered, structured and contacted in the third step. In the fourth step, the chips are passivated and the final metallisations is applied.

5.3.1 Definition of the layer structure

First layer growth

The layers for waveguides, mode shape adapters and photodetectors were formed by two growth steps and one wet chemical etching step.

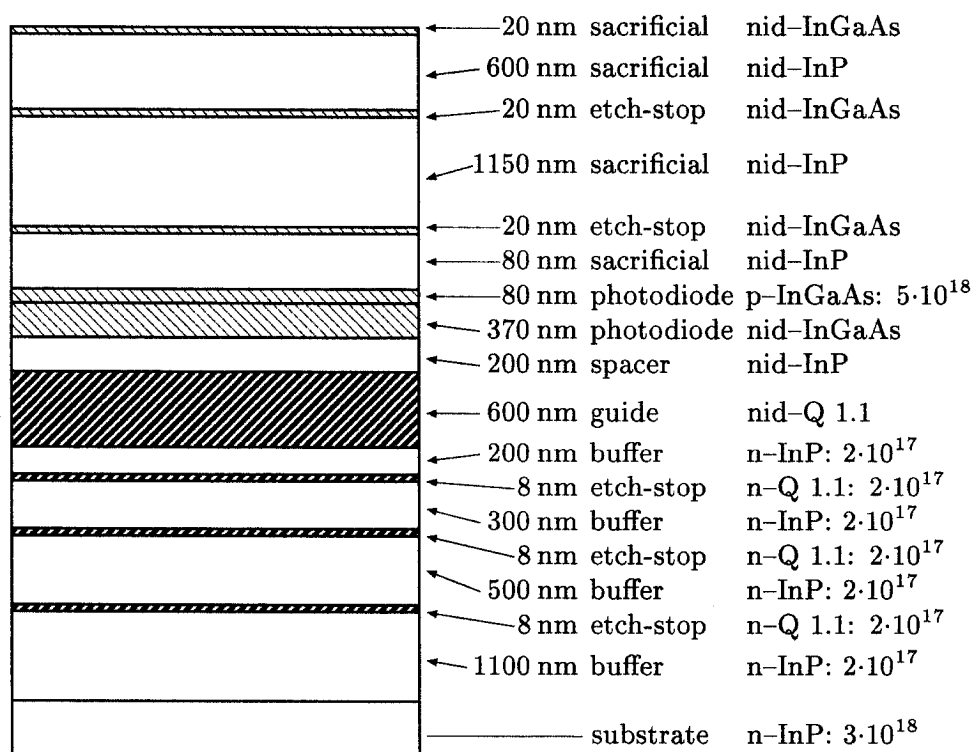


Fig. 5.9: Schematic layer structure of the first growth

First, the layer stack of the waveguide photodetectors was grown lattice matched on an InP wafer, n-doped $3 \cdot 10^{18} [\frac{1}{cm^3}]$ with Silicon. The layer stack is depicted in figure 5.9. It starts with a 2100 nm thick n-doped InP buffer layer with three 8 nm quaternary (InGaAsP) layers, serving as etch stop layers, inserted. The etch stop layers are necessary to prevent uncontrolled etching during the taper etching. On this buffer, the 600 nm thick not intentionally doped light guiding quaternary layer with a bandgap energy of $1.1 \mu m$ is grown. On top of this, a 200 nm thick undoped spacer and the InGaAs used as a photodetector are grown. The undoped spacing layer is necessary to reduce absorption losses in the waveguide section. Finally, auxiliary layers, needed to manufacture the mode shape adapters, are grown.

Definition of the photodetectors

In this step, the auxiliary layers above the first etch stop are removed except at the photodetector sites.

The sites of the photodetectors were masked with photoresist (AZ1518), which is resistant against semiconductor etching solutions. The InGaAs layer was then removed with a mixture of 4:20:1 mixture of 98% H_2SO_4 , H_2O and H_2O_2 . Next the photoresist is removed using solvents. The structured InGaAs layer now serves a mask for the InP etching step. The InP layer is etched with a 1:2 mixture of 32% HCl and 100% CH_3COOH .

Diffusion limited etching of vertical mode shape adapters

The vertical mode shape adapters were formed by planar diffusion limited wet chemical etching. Further etching steps served to remove the auxiliary layers from the photodetector sites and remove the photodetector material everywhere else at the same time.

To form the mask for this process step, 2000 \AA SiO_x are deposited using plasma enhanced chemical vapour deposition (PE-CVD). The SiO_x is subsequently structured with photolithography and reactive ion etching (RIE) with a 1:5 mixture of CHF_3 and Argon. SiO_x was chosen for the mask material because it resists the etching solution used and withstands the high temperatures of the following selective area growth. The diffusion limited etching agent chosen is a solution of 0.1 ml bromine in 100 ml methanol. As the etching is diffusion limited, the etching rates are the higher, the nearer and larger masked areas are. As a consequence the etching rate is highest where

ellipses are nearest, decreasing as the distance between the ellipses increases. To increase the homogeneity, the 2 inch wafer was positioned on a 3 inch wafer.

The etching process has to be concluded, when the InGaAs material of the photodetector layer is reached and before the etch stop layer above the photodetector layer at the photodetectors site is removed. The etching process at the photodetectors sites lags approximately 600 nm behind because the top auxiliary layer has not been removed there as described above. This moment can be determined accurately because interference phenomena, caused by the sequence of thin layers of InP and InGaAs, then disappear. After the diffusion limited etching, the residual InP is removed from the photodetector sites by etching with a 1:2 mixture of HCl and CH₃COOH. Subsequently, the photodetector material is removed except at the photodetector sites, now masked with InP, by etching using a mixture of 4:20:1 mixture of 98% H₂SO₄, H₂O and 30% H₂O₂. A side effect of these etching steps is the removal of any residual contamination.

Second growth

A selective area growth was used to planarise the wafer and the p-doped semiconductor material of the pin-diode is grown. The layer stack after the second growth is depicted in figure 5.10.

The growth rate is highest where the gap between the ellipses as the MOVPE growth is also diffusion limited. Thus, the effects of the diffusion limited etching are reversed and the wafer is planarised. After the selective area growth crystallite grown on defects of the SiO_x mask have to be removed, otherwise they would prevent a good contact between mask and wafer in the following photolithographic steps. This was done with a series of wet chemical etching steps. Finally, the SiO_x mask is removed.

5.3.2 Structuring of the waveguides

Evaporation of p-contact metallisation of the switching electrodes

In this step, metal forming an ohmic contact is evaporated on the highly p-doped InGaAs contact layer. The semiconductor is contacted now because the deposition of oxide and dry etching later on tends to damage the surface of the semiconductor, resulting in contacts of lower quality.

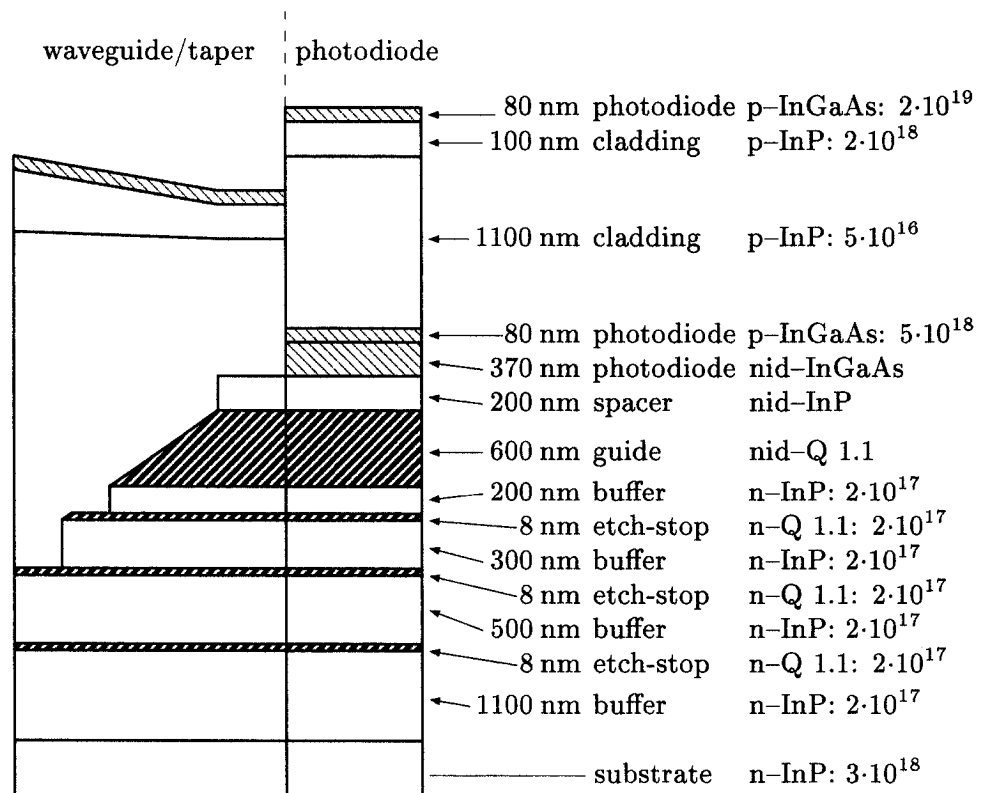


Fig. 5.10: Schematic layer structure of the taper / waveguide (left) and the photodiode (right) after the second growth.

As etchants for metal usually also etch semiconductor material a lift off technique based on chlorobenzene with a $1.8 \mu\text{m}$ thick photoresist was used to evaporate a stack of 300 \AA titanium, 400 \AA platinum and 1000 \AA gold. The titanium guarantees good adhesion and the platinum acts as a diffusion barrier to prevent the diffusion of gold into the semiconductor, destroying the contact. The width of the electrode was chosen to be $1 \mu\text{m}$ narrower than the rib allowing the rib mask to cover it completely.

Rib etching

The light guiding structures are formed in this step. Additionally, the photodetectors and switching electrodes are electrically insulated from the rest of the chip.

A 200 nm thick PECVD deposited SiO_x mask was used for the rib etching because it has to withstand a considerable time of dry etching. As the quality of the photolithographic step defining the rib geometry was critical, 70 \AA titanium was evaporated onto the oxide as adhesion promoter. The Oxide was then structured using reactive ion etching with a 1:5 mixture of CHF_3 and argon. Afterwards, the rib was dry etched in two steps using a 5:1 mixture of H_2 and CH_4 . Dry etching was used because it allows for vertical walls independent of direction of the rib relative to the crystal axes as opposed to wet chemical etching. The etching rate under these conditions was between 10 and 12 nm per minute . During the etching process plastic formed on top of the oxide mask and had to be removed with O_2 plasma.

In the first step the waveguide was etched 800 nm deep. Then a 50 nm long break was made oxide mask using buffered HF at the end of the switching electrodes and photodetectors and the rib etching was continued until 50 nm into the guiding layer. The resulting gap in the top of the waveguide does not affect its optical properties, but it effectively insulates the electrodes from the rest of the device. The etching depth into the guiding layer can be controlled very accurately because interference phenomena occur when the InP layer above becomes thinner than 100 to 150 nm and InGaAsP has a different colour than InP.

Deep etching of the MMI's

Next, the lateral confinement of the multi mode interference couplers (MMIs) was increased by etching the guiding layer deeper at the side of the MMIs. This increased their fabrication tolerance and polarisation insensitivity.

A photoresist mask was used to define the deep etched areas at the sides of the MMIs. The mask was self aligning because the SiO_x mask from the rib etching step still covers the MMI. The core layer was then etched another 300 nm, using the same dry etching technique as used for etching the rib.

Etching of the n-contact areas and lateral mode shape adapters

Deep trenches were etched at the sides of the mode shape adapters to provide lateral confinement. Simultaneously, the areas of the ground contacts were etched down to the substrate. This is necessary to obtain a good electric contact with the highly n-doped substrate.

A 3 μm thick photoresist mask was used for this etching step. The trenches defining the horizontal confinement of the mode shape adapters are self aligning as the oxide mask was still on the rib. A 5:1 mixture of H_2 and CH_4 was used to etch the semiconductor material down into the substrate. To avoid burning and polymerisation of the photoresist, the etching process was stopped every 10 minutes for 5 minutes to allow the photoresist to cool. After the completion of the deep etching process O_2 plasma and solvents were needed to remove the plastic and mask.

Evaporation and alloying of the ground contacts

In this step germanium and gold forming the n-contacts was evaporated and alloyed.

First, the oxides formed during the exposure to O_2 plasma during the previous steps was removed with a short dip in a 10% NaOH solution. Subsequently, the a metal stack of 50Å nickel, 300Å germanium, 600Å gold, 100Å nickel and 500Å gold was evaporated using a chlorobenzene lift off technique. The germanium and gold were afterward alloyed by heating one minute to 450°C with a one minute heating ramp.

5.3.3 Photodetectors

Uncovering and definition of the photodetectors

The photodetector material has been covered by the second growth step and masked during the rib etching. This material is now removed and the InGaAs is shaped into its final form.

The covering material was removed by selective etching with a 4:20:1 solution of 98% H_2SO_4 , H_2O and H_2O_2 and a 1:2 mixture of 32% HCl and 100% CH_3COOH . Afterwards the InGaAs was shaped with a separate photoresist mask and etching with the mixture of H_2SO_4 , H_2O and H_2O_2 .

Evaporation of the p-contacts of the photodetectors

Directly after the uncovering and shaping of the photodetectors, metal forming ohmic p-contacts was evaporated. A lift off technique based on chlorobenzene with a $1.8 \mu\text{m}$ thick photoresist was used to evaporate a stack of 300 Å titanium, 400 Å platinum and 1000 Å gold.

5.3.4 Passivation, final metallisation and coatings

Passivation of the integrated devices

After the final fabrication and shaping of all components, the device was conditioned and passivated with a layer of polyamide. Then, the polyamide was patterned to expose the cleavage edges and n-contacts.

First, the top atomic layers, oxidised and damaged by the ion bombardment of the dry etching process, were removed by a quick dip in 10% NaOH , because they would degrade the quality and performance of the pn-junction. Dipping in HF would be even more effective, however, HF etches titanium and would therefore underetch the p-metallisation. Immediately afterwards, polyamide (Pyralin PI-2555) was spun onto the wafer and heated to 125°C for 30 minutes (softbake). The polyamide was subsequently patterned and removed from the n-contacts and cleavage edges by a photolithographic process. This is possible as Pyralin is dissolved by the developer used for photolithography. This method, however, does not allow resolutions below a few microns, depending on the thickness of the photoresist and the polyamide. The polyamide was then polymerised by heating to 250°C for three hours. In the polymerised state the polyamide can not be dissolved anymore.

Gap etching over the switching electrodes

A 2 μm wide slit to allow contacting has to be etched into the polyamide above the p-contacts of the phase shifting electrodes.

The resolution of the structuring technique described above is not sufficient to remove the polyamide from the p-contacts. The 2 μm wide slits were etched with CF_4 reactive ion etching and a photoresist mask. The CF_4 also removed the SiO_x covering the rib and p-contact. As CF_4 corrodes the photoresist mask with almost the same speed as the polyamide, it was necessary to replace the photoresist mask three times. As a desired side effect, the walls of the slits were not vertical but comparatively shallow.

Evaporating the final metallisation

In this step the contact pads were manufactured and connected to the electrodes. Two masks were used in the photolithographic step to pattern the photoresist for the lift-off process. The first one had openings for the phase-shifting electrodes, contacts on the photodetectors, contact pads and ground contact areas and the second mask to connect all metal surfaces. Immediately before the evaporation of metal the wafer was subjected to Ar sputtering to increase the adhesion of the metal to the polyamide and to remove any residuals, which might negatively influence the adhesion of the metallisation. Finally 200Å of titanium and 2000Å gold were evaporated.

Electroplating of the metallisation

The metallisation was then electroplated to allow easy bonding and to decrease the electric resistance to the electrodes. The same mask as above was used to pattern the photoresist as mentioned above but not the second mask used to short circuit all metal surfaces. As electroplating deposits metal on all conducting surfaces, the wafer was glued to a nonconducting silicon wafer to avoid electroplating the conducting backside of the wafer. After electroplating 3 μm , gold the photoresist was removed.

Removing the short circuits

Finally, the short circuits between the metallic surfaces had to be removed. The 2000Å gold of the short circuits was etched with a 3:20:1 solution of

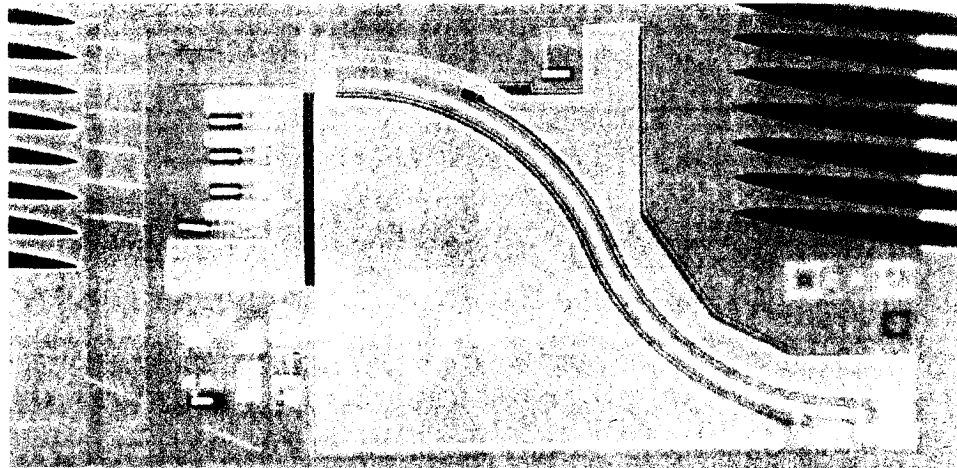


Fig. 5.11: Photograph of a finished transceiver chip. The chip size is $3.5 \times 8.5 \text{ mm}^2$.

KI, H_2O and I. The remaining 200\AA titanium were removed with CF_4 dry etching.

Scribing, breaking and AR/HR coatings

After the processing of the wafer was finished, the wafer was cleaved to separate the individual devices arrayed in a 4×8 grid on the wafer. First, the wafer was cleaved into 8 horizontal stripes of 4 devices. Then, the facets of the devices were cleaved approximately $50\mu\text{m}$ from the mode shape adapters to obtain a good coupling efficiency.

Subsequently, the an anti-reflection coating consisting of SiO and a protective layer of Al_2O_3 to prevent the SiO from oxidising was evaporated on the front facets of the devices. A mirror of titanium and gold was also evaporated on the back facets of the chip. A photograph of a finished chip is shown in figure 5.11.

5.4 Experimental results

5.4.1 Photodetector

The setup to measure the performance of the integrated photodetectors is depicted in figure 5.12. Light from a $1.3\mu\text{m}$ FP laser is modulated by a LiNbO_3

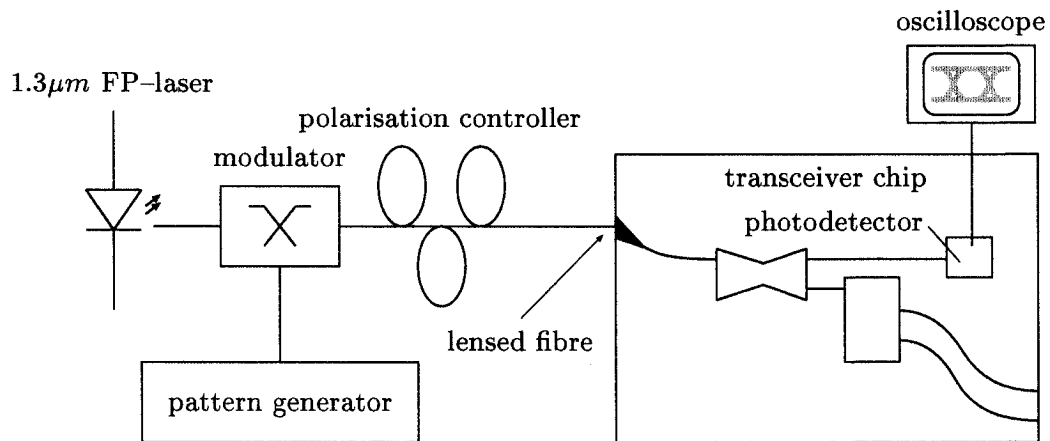


Fig. 5.12: Experimental setup for characterising the photodetector of the transceiver chip.

modulator with a pseudorandom bit sequence. A polarisation controller is used to control the polarisation state of the pulse train, which is then coupled into the transceiver chip. This pulse train is received in the photodetector. The resulting electrical signal is fed directly into a 50 GHz oscilloscope and evaluated. An example of a resulting eye diagram recorded at a bit rate of 2 Gbits/s is shown in figure 5.13. It can be seen that the photodiode has a bandwidth of at least 2 Gbits/s.

To measure the overall quantum efficiency of the photodetector, the optical power exiting the lensed fibre was measured with a calibrated power meter and the resulting photo current was measured with a pico amperemeter. Thereby, the overall efficiency of the photodiode was determined to $45\text{--}55 \frac{\text{mA}}{\text{W}}$. Taking into account the losses (1.5dB coupling losses, 10dB power splitting ratio and 1.5dB excess loss), the internal quantum efficiency of the photodiode is near 100%. The polarisation dependence observed is as low as 0.5dB and can be attributed to the polarisation dependency of the losses in the optical waveguide and of the optical power splitter.

5.4.2 Modulator

The setup to characterise the electro-optical modulator is similar to the setup used for characterisation of the photodiodes described above. It is shown in figure 5.14. The light from a 1.3µm FP laser diode or from a SOA is coupled

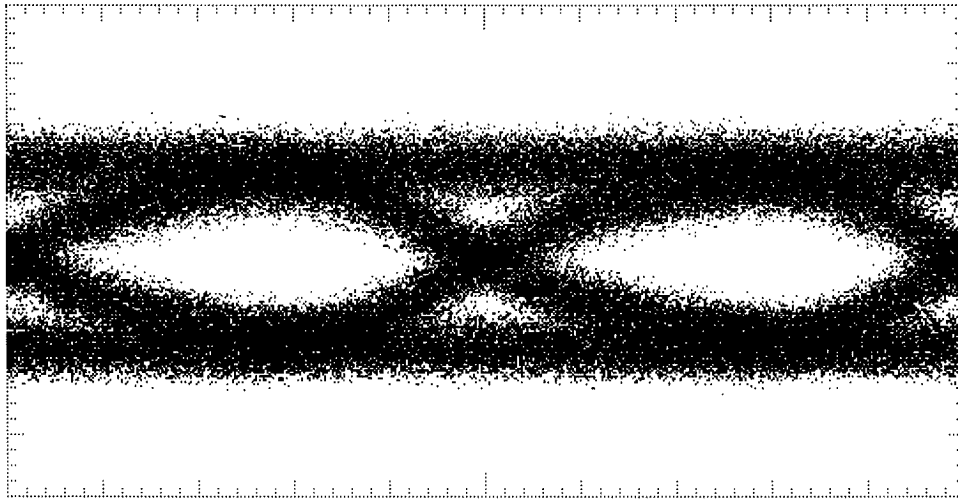


Fig. 5.13: Response of the waveguide photodiode at 2 GBit/s. Eye diagram with horizontal 100 ps/div scale.

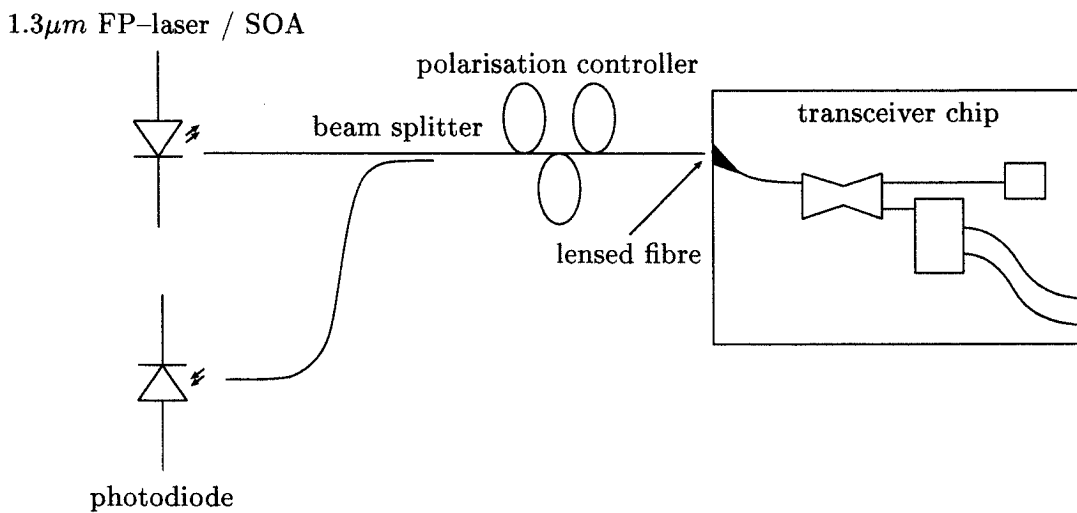


Fig. 5.14: Experimental setup for characterising the electro-optic modulator of the transceiver chip. To measure the performance of the reflective Mach-Zehnder interferometric modulator, the reflected light is extracted with a powersplitter and detected in a broad area photodiode. A $1.3\mu\text{m}$ Fabry-Perot laser was used to measure the switching curves and an $1.3\mu\text{m}$ SOA served as a broad band light source to determine the optical bandwidth of the modulator.

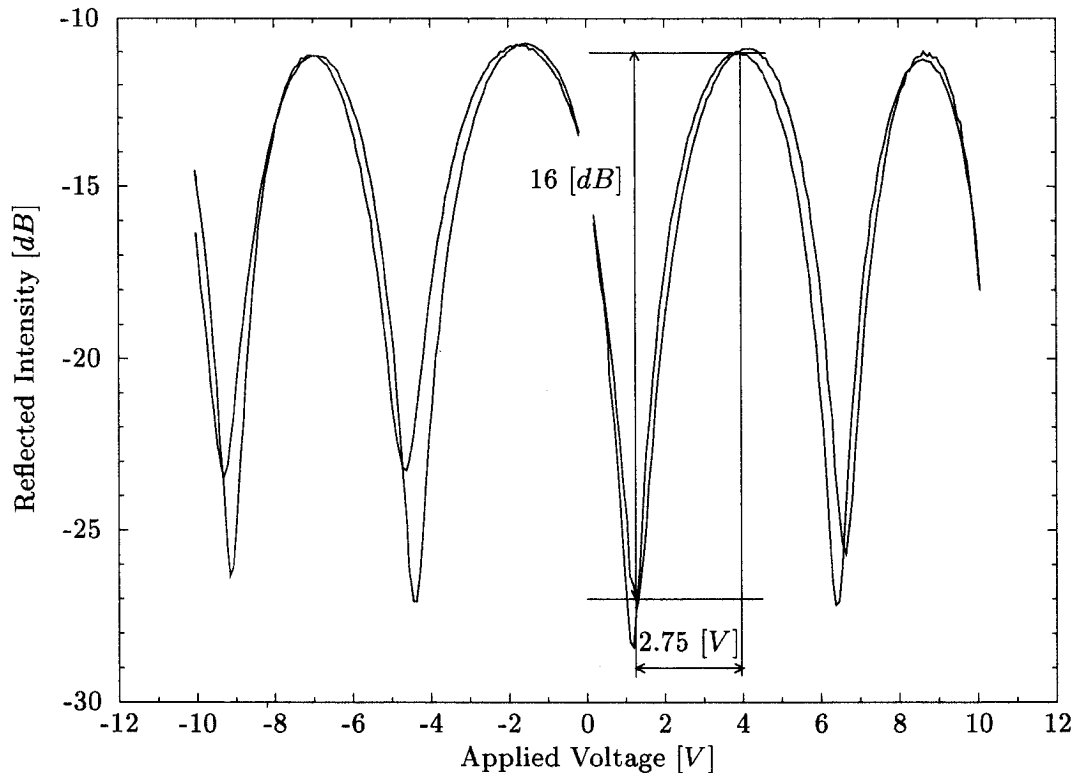


Fig. 5.15: Switching characteristics measured at an optical wavelength of $\lambda = 1.306\mu\text{m}$. The two switching curves show the best and worst case while varying the polarisation state of the incoming optical mode.

into the chip. The backreflected light is then extracted by means of an optical power splitter and converted into an electrical signal in a photodiode.

The polarisation state is therefore unknown. To determine the polarisation sensitivity of the modulator, the polarisation state was varied with a polarisation controller and the switching curves in the best and worst case were recorded. A typical response of a reflective modulator measured at $1.306\mu\text{m}$ is shown in figure 5.15. Single mode fibres do not preserve the polarisation state of the optical mode. It shows nearly polarisation insensitive switching voltages of 2.75 V and overall insertion losses of 11 dB with a polarisation dependence of less than 0.5 dB . By driving the modulator in the “push-pull” switching voltages below 1.5 V are possible. The on-off ratio of the modulator is at least 16 dB .

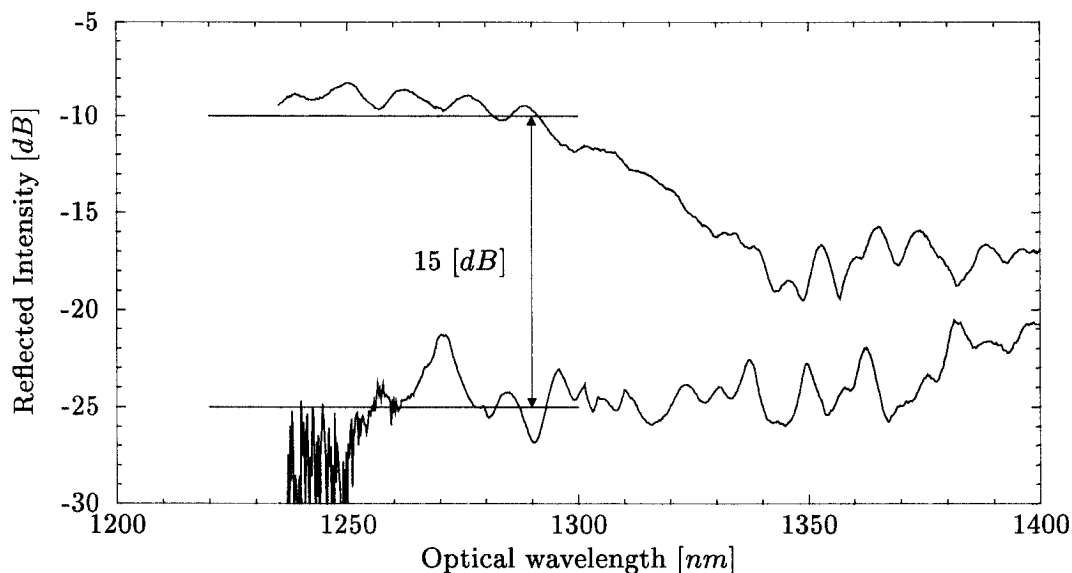


Fig. 5.16: Optical broad band measurement of the switching characteristics of the integrated modulator. The reflected light intensity in the on-state and off-state are plotted versus the wavelength of the incident light.

To determine the bandwidth of the monolithically integrated reflective modulator, a SOA was used as a “white light source”. The spectra of the SOA and of the reflected light in the on-state and off-state were recorded with an optical spectrum analyser (OSA). By comparison of the spectra, the optical losses of the modulator were determined. In figure 5.16 an example of such an analysis is shown. It can be seen that the overall losses of the modulator are as low as 8 dB and that the on-off ratio is larger than 15 dB over at least 40 nm. It can also be seen that the modulator performs best at an optical wavelength of 1250 nm and not at the desired wavelength of 1300 nm. This discrepancy is caused by the performance of the deep-etched multi mode interference couplers which were designed a little too narrow, because the models used for their design start to fail for the deep etching depth used.

5.5 Conclusion

In this chapter, a detailed description of the design considerations and manufacturing process of an InP/InGaAsP base transceiver chip intended for the

use in passive optical networks with all optical components monolithically integrated is given. The transceiver chip features monolithically integrated mode size adapters, waveguide photodiodes and a reflective electro-optic modulator.

Experimental measurement carried out on realised devices indicate that the bandwidth of the photodiode is at least 2 GHz and has an overall efficiency of the $50 \frac{mA}{W}$. Taking the expected optical losses into account, it can be assumed that the internal quantum efficiency of the photodiode is near 100%.

The reflective electro-optical modulator has a good overall performance which includes comparatively low optical losses between 8 and 9 dB, an on-off ratio of at least 15 dB over an optical bandwidth of over 40 nm. The switching voltage is as low as 2.75V and switching speeds of several hundred megahertz can be expected.

It has been successfully demonstrated that monolithic integration of several optical components is possible. By optimising the individual components, a better performance, especially a much higher bandwidth, can be achieved at the cost of complicating the manufacturing process significantly.

6. SUMMARY AND OUTLOOK

6.1 Summary

In the frame of this thesis the electro-optic occurring in the electric field of reverse biased InP/InGaAsP pin diodes and the monolithic integration of multiple electro-optic components were studied. The most important effects are the Franz-Keldysh, the Pockels and the free carrier effect. Furthermore the feasibility of the monolithic integration of photodetectors, waveguides, mode shape adapters and modulators was demonstrated.

Device physics

The electro-optic effects, occurring in InP/InGaAsP based reverse biased pin-diodes, were analysed experimentally over a large optical wavelength range and compared to theoretical models. Under these conditions the relevant effects are the Pockels effect, the Franz-Keldysh effect and the plasma effect. The experimentally obtained data was found to fit the theoretical predictions very well.

The Pockels effect shows a $\cos 2\varphi$ dependency relative to the $[0\bar{1}1]$ crystal axis and affects only the TE-mode on (100) substrates. Its coefficient has a constant value of $1.47[\frac{\text{Å}}{\text{V}}]$ over the observed wavelength range.

The Franz-Keldysh effect is in good approximation proportional to the square of the electric field $|\vec{E}|^2$ and to the bandgap to photon energy difference to the power of $\frac{5}{2}$ $(E_g - \hbar\omega)^{\frac{5}{2}}$. It is therefore strongly dispersive. Furthermore the magnitude of the Franz-Keldysh effect depends strongly on the polarisation. It is approximately 60% larger for the TM polarisation than the TE polarisation. For a bandgap to photon energy difference of 175 meV, which is a reasonable choice for electro-optic space switches because it allows for high refractive index changes while keeping the absorption losses low, the

coefficients of the Franz–Keldysh have been found to be $62 \times 10^{-20} [\frac{m^2}{V^2}]$ and $98 \times 10^{-20} [\frac{m^2}{V^2}]$ for the TE and TM polarisation respectively.

The Franz–Keldysh effect is also the main contributor to the electro-absorption which is also strongly dispersive. The absorption increases rapidly when the photon energy comes close to the bandgap. High absorption thus makes energy difference below 150 meV unattractive for use in electro-optic space switches. On the other hand the refractive index change decreases rapidly as the energy difference increases. For practical purposes the energy difference should therefore be chosen to be below 200 meV.

Realisation of the transceiver chip

The feasibility to integrate waveguides, modulators, mode-shape adapters and photodetectors was demonstrated. To fabricate the transceiver chip the following technological issues had to be solved:

- Monolithic integration of photodetectors and mode-shape adapters into a waveguide structure.
- Development of a process allowing the placement of mode-shape adapters in arbitrary places on the wafer.
- Optimisation of a 10:90 multi mode interference coupler.

Experimental measurements on a realised device show an overall fibre-to-fibre loss of 8 dB, an on-off ratio of at least 15 dB over an optical wavelength range of 40 nm, a polarisation sensitivity of less than 1 dB and a switching voltage of 2.75 V. The photodetector has an overall responsivity of $50 \frac{mA}{W}$, corresponding to approximately 100% quantum efficiency, and a bandwidth of 2 GHz.

6.2 Outlook

Device physics

The presented physical models of the electro-optic effects explain the experimental data on the refractive index and the absorption index change very well.

However to understand the effects of the free carriers completely further investigations are necessary. Aside from the plasma effect, the band filling and band gap shrinking effect should be taken into account. This was not done in this work because the carrier effects contribute little to the refractive index change in a reverse biased pin-diode and because the experimental analysis of these effects difficult and inaccurate in devices made with the technology available.

Transceiver chip

The experimental results of the fabricated transceiver chips shows that monolithic integration of waveguide, photodetectors, mode shape adapters and modulators is possible.

Currently the manufacturing process of these devices is complicated and expensive. It would be desirable to simplify this process. This is especially true for the mode shape adapter part.

The transceiver chip has still a big potential for optimisation. By replacing the electrodes of the modulator section with strip-lines, switching speeds up to several gigabits per second are possible. The photodetector can also be tuned to be capable of handling several ten gigabits per second. These measures to optimise the speed of the device however complicate the manufacturing process further.

Investigations into more efficient and less space consuming phase shifters would be worthwhile. By reducing the size of the devices the costs per device, which depends mainly on its size, could be reduced significantly.

BIBLIOGRAPHY

- [1] A. Bell, "Selenium and the Photophone", *The Electrician*, p. 214, 1880.
- [2] A. Schawlow and C. Townes, "Infrared and optical masers", *Physical Review*, vol. 212, pp. 1940–1949, 1958.
- [3] T. Maiman, "Stimulated optical radiation in ruby", *Nature*, vol. 187, pp. 493–494, May 1960.
- [4] R. Hall, G. Fenner, J. Kingsleya, T. Soltys, and R. Carlson, "Coherent light emission from GaAs junction", *Physical Review Letters*, vol. 9, pp. 366–368, Nov. 1962.
- [5] M. Nathan, W. Dumke, G. Burns, F. Dill, and G. Lasher, "Stimulated emission of radiation from GaAs p-n junctions", *Applied Physics Letters*, vol. 1, pp. 62–64, Nov. 1962.
- [6] K. Oe, S. Ando, and K. Sugiyama, "1.3 μm CW operation of InGaAsP/InP DH diode lasers at room temperature", *Japanese Journal of Applied Physics*, vol. 16, p. 1273, 1977.
- [7] N. Kabayashi and Y. Horikoshi, "1.5 μm InGaAsP/InP heterostructure laser with optical waveguide structure", *Japanese Journal of Applied Physics*, vol. 18, p. 1005, 1979.
- [8] G. Henshall and P. Greene, "Low threshold (Ga, In)(As, P) DH lasers emitting at 1.55 μm grown by LPE", *Electronics Letters*, vol. 15, p. 621, 1979.
- [9] J. Strong, "Appendix N", in *Concepts of Classic Optics*, San Francisco: Freeman, 1959.
- [10] F. Kapron, D. Keck, and R. Maurer, "Radiation losses in glass optical waveguides", *Applied Physics Letters*, vol. 17, pp. 423–425, 1970.

- [11] T. Miya, Y. Terunuma, T. Hosaka, and T. Miyashita, "Ultimate low-loss single mode fiber at $1.55\mu\text{m}$ ", *Electronics Letters*, vol. 15, pp. 106–108, 1979.
- [12] Y. Yano, T. Ono, K. Fukuchi, T. Ito, H. Yamazaki, M. Yamaguchi, and E. Emura, "2.6 Terrabit/s WDM transmission experiment using optical duobinary coding", in *Proceedings of the 22nd European Conference on Optical Communication (ECOC'96)*, (Oslo, Norway), pp. 5.3–5.6, 1996.
- [13] S. Brewer, "Two pioneer undersea cable links", *PTC'86, Honolulu*, pp. 31–34, 1986.
- [14] R. Easton, "TAT-8: The First Transatlantic Optical System", *Proceedings of the SPIE*, vol. 1174, pp. 114–122, 1989.
- [15] T. H. Wood, R. D. Feldman, and R. F. Austin, "Demonstration of a Cost-Effective, Broadband Passive Optical Network System", *IEEE Photonics Technology Letters*, vol. 6, pp. 575–577, Apr. 1994.
- [16] L. Altwegg, A. Azizi, P. Vogel, Y. Wang, and F. Wyler, "LOCNET: A Fiber in the Loop System With No Light Source at the Subscriber End", *Journal of Lightwave Technology*, vol. 12, pp. 535–539, Mar. 1994.
- [17] L. Thylén, "Guided-wave switching devices", in *Proceedings of the 17th European Conference on Optical Communication (ECOC'91)*, (Paris, France), pp. 109–116, 1991. invited paper.
- [18] M. Tachikura, T. Katagiri, and H. Kobayashi, "Strictly Nonblocking 512×512 Optical Fiber Matrix Switch Based on Three-Stage Clos Network", *IEEE Photonics Technology Letters*, vol. 6, pp. 764–766, June 1994.
- [19] T. Kirihera, M. Ogawa, H. Inoue, H. Koderu, and K. Ishida, "Lossless and low-crosstalk characteristics in an InP-based 4×4 optical switch with integrated single-stage optical amplifiers", *IEEE Photonics Technology Letters*, vol. 6, no. 2, pp. 218–221, 1994.
- [20] M. Gustavsson, B. Lagerström, L. Thylén, M. Janson, L. Lundgren, A. Mörner, M. Rask, and B. Stolz, "Monolithically integrated 4×4 InGaAsP/InP laser amplifier gate switch array", *Electronics Letters*, vol. 28, pp. 2223–2225, 1992.

- [21] M. Bachmann, M. Smit, P. Besse, E. Gini, and H. Melchior, "Polarization-insensitive low-voltage waveguide switch using InGaAsP/InP four-port Mach-Zender interferometer", in (*OFC/IOOC'93*), vol. 4, (San Jose, California, USA), pp. 32-33, 1983.
- [22] P. Besse, M. Bachmann, H. Melchior, L. Soldano, and M. Smit, "Optical bandwidth and fabrication tolerance of MMI couplers", *Journal of Lightwave Technology*, vol. 12, pp. 1004-1009, 1994.
- [23] M. Bachman, P. Besse, and H. Melchior, "General self imaging properties on $N \times N$ multimode interference couplers including phase relations", *Applied Optics*, vol. 33, pp. 3905-3911, 1994.
- [24] T. Tamir, ed., *Guided-Wave Optoelectronics*, vol. 26 of *Electronics and photonics*, ch. Theory of optical waveguides. Springer, Berlin Heidelberg, 1988.
- [25] R. Hunsberger, *Integrated Optics, Theory and technology*. Springer, 4 ed., 1995.
- [26] J.-F. Vinchant, J. A. Cavailles, M. Erman, P. Jarry, and M. Renaud, "InP/InGaAsP Guided-Wave Phase Modulators Based on Carrier-Induced Effects: Theory and Experiment", *Journal of Lightwave Technology*, vol. 10, p. 63, Jan. 1992.
- [27] B. Bennett, R. Soref, and J. D. Alamo, "Carrier-Induced Change in Refractive Index of InP, GaAs, and InGaAsP", *IEEE Journal of Quantum Electronics*, vol. 26, p. 113, Jan. 1990.
- [28] L. Zverev, S. Negashev, V. Kruzhaev, and G. Min'kov, "Mechanism of band gap variation in heavy doped gallium arsenide", *Soviet Physics - Semiconductors*, vol. 11, pp. 603-605, 1977.
- [29] P. Günter, *Quantenelektronik IV: Elektro-Optik*. PhD thesis, Swiss Federal Institute of Technology, 1989. chapter 2.
- [30] P. Günter, *Quantenelektronik III: Nichtlineare Optik*. PhD thesis, Swiss Federal Institute of Technology, 1992. chapter 1.4.3.
- [31] S. Wemple and M. DiDomenico, "Optical Dispersion and the Structure of Solids", *Physical Review Letters*, vol. 23, p. 1156, Nov. 1969.

- [32] S. H. Wemple and J. M. DiDomenico, "Theory of the elasto-optic effect in nonmetallic crystals", *Physical Review B*, vol. 1, pp. 193–202, Jan. 1970.
- [33] S. Wemple and M. DiDomenico, "Behavior of electronics dielectric constant in covalent and intrinsic Materials", *Physical Review B*, vol. 3, p. 1338, Feb. 1971.
- [34] J. M. DiDomenico and S. H. Wemple, "Oxygen-octahedra ferroelectrics. I. Theory of electro-optical and nonlinear optical effects", *Applied Physics Letters*, vol. 40, pp. 720–734, Feb. 1969.
- [35] W. Franz, "Einfluß eines elektrischen Feldes auf eine optische Absorptionskante", *Zeitschrift für Naturforschung*, vol. 13a, pp. 484–489, 1958.
- [36] L. Keldysh, "The effect of a strong electric field on the optical properties of insulation crystals", *Soviet Physics JETP*, vol. 34, p. 758, July 1958.
- [37] S. Sze, *Semiconductor devices, physics and technology*, ch. p-n Junction. John Wiley & Sons, 1985.
- [38] K. Tharmalingam, "Optical Absorption in the Presence of a Uniform Field", *Physical Review*, vol. 130, p. 2104, June 1963.
- [39] J. Callaway, "Optical Absorption in an Electric Field", *Physical Review*, vol. 130, p. 549, Apr. 1963.
- [40] J. Callaway, "Optical Absorption in an Electric Field", *Physical Review*, vol. 134, p. A998, May 1964.
- [41] D. Aspnes, "Electric Field Effects on Optical Absorption near Thresholds in Solids", *Physical Review*, vol. 147, p. 554, July 1966.
- [42] D. Aspnes, "Electric Field Effects and the Dielectric Constant of Solids", *Physical Review*, vol. 153, p. 972, Jan. 1967.
- [43] D. E. Aspnes, "Handbook on Semiconductors", vol. 2, ch. Chapter 4A: Modulation Spectroscopy/Electric Field Effects on the Dielectric Function of Semiconductors, p. 109, North Holland Publishing Company, 1980.

- [44] C. Penchina, "Phonon-Assisted Optical Absorption in an Electric Field", *Physical Review*, vol. 138, p. A924, May 1965.
- [45] M. Chester and L. Fritsche, "Phonon-Assisted Electroabsorption", *Physical Review*, vol. 139, p. A518, July 1965.
- [46] A. Frova and P. Handler, "Franz-Keldysh Effect in the Space-Charge Region of a Germanium p-n Junction", *Physical Review*, vol. 137, p. A1857, Dec. 1965.
- [47] K. Shaklee, F. Pollak, and M. Cardona, "Electroreflectance at a Semiconductor-Electrolyte Interface", *Physical Review Letters*, vol. 15, p. 883, Dec. 1965.
- [48] R. Elliott, "Intensity of Optical Absorption by Excitons", *Physical Review*, vol. 15, pp. 1384-1389, Dec. 1957.
- [49] L. Landau and E. Lifschitz, *Lehrbuch der Theoretischen Physik*, vol. III Quantenmechanik, ch. 24. Die Bewegung imhomogenen Feld, p. 72 ff. Akademie-Verlag Berlin, 9 ed., 1979.
- [50] M. Abramowitz and I. Stegun, eds., *Handbook of Mathematical Functions*, vol. 55 of *Appl. Math. Ser.*, ch. 10.4 Airy Function, p. 446ff. Washington D.C: U.S. Department of Commerce, National Bureau of Standards, 1964.
- [51] J. Callaway, *Energy Band Theory*. Academic Press Inc., New York, 1964.
- [52] K. Viswanathan and J. Callaway, "Dielectric Constant of a Semiconductor in an External Electric Field", *Physical Review*, vol. 143, p. 564, Mar. 1966.
- [53] S. Adachi and K. Oe, "Linear electro-optic effects in zinblende-type semiconductors: Key properties of InGaAsP relevant to device design", *Journal of Applied Physics*, vol. 56, p. 74, July 1984.
- [54] J. Zucker, *Propertiers of Lattice-Matched and Strained Indium Gallium Arsenide*, ch. Linear and quadratic electro-optic coefficients in InGaAsP. IEE Inspec, 1993.

- [55] C. Berseth, C.W., and F. Reinhart, "The electro-optic coefficients of GaAs: Measurement at 1.32 and 1.52 μm and study of their dispersion between 0,9 and 10 μm ", *Journal of Applied Physics*, vol. 71, p. 2821, Mar. 1992.
- [56] J. Faist and F. Reinhart, "Phase modulation in GaAs/AlGaAs double heterostructures. I Theory", *Journal of Applied Physics*, vol. 67, p. 6998, June 1990.
- [57] S. Lee, R. Ramsawamy, and V. Sundaram, "Analysis and design of high-speed high efficiency GaAs-AlGaAs double-hetero waveguide phase modulator", *IEEE Journal of Quantum Electronics*, vol. 27, p. 726, Mar. 1991.
- [58] D. W. Faulkner, D. B. Payne, J. R. Stern, and J. W. Ballance, "Optical Networks for Local Loop Applications", *Journal of Lightwave Technology*, vol. 7, pp. 1741-1751, Nov. 1989.
- [59] H. Nakajima, A. Leroy, B. Pierre, P. Boulet, J. Charil, S. Grosmaire, A. Gloukhian, Y. Rafflé, S. Slempek, F. Mallécot, and F. Doukhan, "1.3 μm / 1.55 μm in-line transceiver assembly with -27dBm full-duplex sensitivity", *Electronics Letters*, vol. 34, no. 3, pp. 303-304, 1998.
- [60] Y. Tohmori, M. Fukuda, S. Matsumoto, T. Kurosaki, M. Yamamoto, Y. Itaya, T. Sugie, and H. Tsuchiya, "Optical Module with a Silica-Based Planar Lightwave Circuit for Fiber-Optic Subscriber Systems", *IEEE Photonics Technology Letters*, vol. 4, pp. 660-662, June 1992.
- [61] J. Cross, A. Lopez-Lagunas, B. Buchanan, L. Carastro, S.-C. Wang, N. M. Kokersset, S. Wills, M. Brooke, and M. A. Ingram, "A Single-Fiber Bidirectional Optical Link Using Colocated Emitters and detectors", *IEEE Photonics Technology Letters*, vol. 8, pp. 1385-1387, Oct. 1996.
- [62] G. Foster, J. Rawsthorne, J. Hall, M. Keraley, and P. Williams, "OEIC WDM transceiver modules for local access networks", *Electronics Letters*, vol. 31, pp. 132-133, Jan. 1995.
- [63] M. Okayasu, Y. Suzuki, N. Yoshimoto, R. Iga, H. Sugiura, and J. Jushida, "Bi-directional transmission experiment using as semiconductor optical amplifier transceiver module for WDM-PON and WDM-LAN applications", in *Proceedings of the European Conference on Networks and*

- Optical Communications 1999 (NOC'99)*, (Amsterdam, Netherlands), pp. 278–283, 1999.
- [64] C. Holtmann, R. Dall'Ara, P. Besse, D. Sakellariou, W. Hunziker, and H. Melchior, "Reflective semiconductor optical amplifier at $1.3\mu\text{m}$ wavelength for customer connection in optical access networks.", in *Proceedings of Optical Amplifiers and their Application, TOPS Vol. 5*, (Monterey, CA, USA), pp. 193–196, 1996.
- [65] R. Ben-Michael, U. Koren, B. Miller, M. Young, T. Koch, M. Chien, R. Capik, G. Raybon, and K. Dreyer, "A Bi-Directional Transceiver PIC for Ping-Pong Local Loop Configurations Operating at $1.3\text{-}\mu\text{m}$ Wavelength", *Journal of Lightwave Technology*, vol. 7, pp. 1424–1426, Dec. 1995.
- [66] T. Kurosaki, Y. Tohmori, M. Fukuda, M. Nakamura, H. Kimora, S. Matsumoto, and T. Sugie, "Dynamic properties of $1.3\mu\text{m}$ semi-insulating-BH light-emission-and-detection (LEAD)-diode module for subscriber TCM transmission systems", *Electronics Letters*, vol. 31, pp. 189–191, Feb. 1995.
- [67] Y. Tohmori, M. Fukuda, S. Matsumoto, T. Kurosaki, M. Yamamoto, Y. Itaya, T. Sugie, and H. Tsuchiya, " $1.3\mu\text{m}$ light-emission-and-detection (LEAD) diodes with semi-insulating buried heterostructure", *Electronics Letters*, vol. 30, pp. 1518–1519, Sept. 1994.
- [68] C. Gibassier, J. Abiven, C. Ramus, F. Huet, and J. Saulnier, "Simultaneous two-way light intensity modulation optical transmission at the same bit rate without a light source in the subscriber terminal", *Electronics Letters*, vol. 30, pp. 1162–1163, July 1994.
- [69] J. Hauden, H. Porte, and J. Goedgebuer, "Demonstration of a single source bidirectional fibre link using polarisation insensitive LiNbO_3 integrated coherence modulators", *Electronics Letters*, vol. 32, pp. 751–752, Apr. 1996.
- [70] J.-P. Goedgebuer, A. Hamel, and H. Porte, "Full Bidirectional Fiber Transmission Using Coherence-Modulated Lightwaves", *IEEE Journal of Quantum Electronics*, vol. 28, pp. 2685–2691, Dec. 1992.

- [71] C. Marxer, M. Grétilat, V. Jaecklin, R. Baettig, O. Anthamnten, P. Vogel, and N. de Rooij, "MHz Opto-Mechanical Modulator", in *Proceedings of the 8th International Conference on Solid State Sensors and Actuators and Eurosensors IX*, (Stockholm, Sweden), June 1995.
- [72] O. Kim and W. Bonner, "Infrared reflectance and absorption of n-type InP", *Journal of Electronic Materials*, vol. 12, pp. 827–836, 1983.
- [73] C. Henry, R. Logan, F. Merritt, and J. Lunogo, "The effect of intervalence band absorption on the behaviour of InGaAsP lasers", *IEEE Journal of Quantum Electronics*, vol. 19, pp. 947–952, 1975.
- [74] R.J.Deri, R. Hawkins, and E. Kapon, "Rib profile effects on scattering in semiconductor optical waveguides", *Applied Physics Letters*, vol. 53, pp. 1483–1485, 1988.
- [75] G. Nakagawa, K. Miura, M. Makakiuchi, and M. Yano, "Highly efficient coupling between LD array and optical fibre array using Si microlens array", *IEEE Photonics Technology Letters*, vol. 5, pp. 1056–1058, 1993.
- [76] H. Presby and C. Edwards, "Near 100% efficient fibre microlenses", *Electronics Letters*, vol. 28, pp. 582–583, 1975.
- [77] T. Brenner, M. Bachmann, and H. Melchior, "Low-loss fibre-to-semiconductor waveguide coupling using integrated optical mod expanders", in *IEEE Laser and Electro-Optics Society, Annual Meeting*, (Boston), pp. 267–268, 1994.
- [78] T. Brenner, M. Bachmann, and H. Melchior, "Vertically tapered InGaAsP/InP waveguides for highly efficient coupling to flat end single mode fibres.", *Applied Physics Letters*, vol. 65, pp. 798–800, 1994.
- [79] T. Koch, J. Davis, and D. Wickramasinghe, "Finite element/finite difference propagation algorithm for integrated optical devices.", *Electronics Letters*, vol. 25, no. 8, pp. 514–516, 1989.
- [80] L. Soldano, M. Bachmann, P. Besse, M. Smit, and H. Melchior, "Large optical bandwidth of InGaAsP/InP multimode interference 3dB couplers", in *Proceeding of the European Conference for Integrated Optics (ECIO)*, (Neuchâtel, Switzerland), pp. 14.10–14.11, 1993.

- [81] L. Soldano, F. Veerman, M. Smit, B. Verbeek, A. Dubost, and E. Pennings, "Polanar monomode optical couplers based on multimode interference effects", *Journal of Lightwave Technology*, vol. 10, no. 12, pp. 1843–1849, 1992.
- [82] E. Pennings, R. Deri, A. Scherer, R. Bhat, T. Hayes, N. Andreadakis, M. Smit, L. Soldano, and R. Hawkins, "Ultracompact, low-loss directional couplers on InP based on selfimaging by multimode interference", *Applied Physics Letters*, vol. 59, pp. 1926–1928, 1991.
- [83] J. Zucker, K. Jones, T. Chiu, B. Tell, and K. Brown-Goebeler, "Strained quantum wells for polarisation-independent electro-optic waveguide switches", *Journal of Lightwave Technology*, vol. 10, pp. 1926–1930, 1992.
- [84] M. Bachmann, M. Smit, P. Besse, E. Gini, H. Melchior, and L. Soldano, "Polarisation-insensitive low-voltage optical waveguide switch using InGaAsP/InP four-port Mach-Zehnder interferometer", in *Proceedings of the Conference for Optical Fiber Communication (OFC)*, (San Jose, USA), pp. 32–33, 1993.
- [85] T. Niemeier and R. Ulrich, "Quadrature outputs from fibre interferometer with 4×4 coupler", *Optics Letters*, vol. 11, pp. 677–679, 1986.
- [86] E. Pennings, R. Deri, R. Bhat, T. Hayes, and N. Andradakis, "Ultracompact integrated all-passive optical 90° hybrid using selfimaging", in *Proceeding of the European Conference for Optical Communication (ECOC)*, (Berlin, Germany), pp. 461–464, 1992.
- [87] R. van Roijen, E. Pennings, M. van Stralen, T. van Dongen, B. Verbeek, and J. van der Keijden, "Compact InP-based ring lasers employing multimode interference couplers and combiners", *Applied Physics Letters*, vol. 64, pp. 1753–1755, 1994.
- [88] O. Bryngdahl, "Image formation using self-imaging techniques.", *Journal of the Optical Society of America*, vol. 63, pp. 416–419, 1973.
- [89] R. Ulrich, "Image formation by phase coincidences in optical wavguides", *Optical Communications*, vol. 13, pp. 259–264, 1975.

- [90] M. Bachmann, P. Besse, and H. Melchior, "Overlapping-image multi-mode interference couplers with reduced number of self-images for uniform and non-uniform power splitting", *Applied Optics*, vol. 34, no. 30, pp. 6898-6905, 1995.
- [91] P. Besse, E. Gini, M. Bachmann, and H. Melchior, "New 1×2 multi-mode interference couplers with free selection of power splitting ratios", in *Proceedings of the European Conference of Optical Communications (ECOC)*, (Firenze, Italy), pp. 669-672, 1994.
- [92] M. Erman and et al., "Optical circuits and integrated detectors", *IEEE Proceedings, Special Issue on semiconductor Optoelectronics, Part J*, vol. 138, no. 2, pp. 101-108, 1991.
- [93] R. Deri, W. Doldissen, R. Hawkins, R. Bhat, J. Soole, L. Schiavone, M. Seto, N. Andreadakis, Y. Silberberg, and M. Koza, "Efficient vertical coupling of photodiodes to InGaAsP rib waveguides", *Applied Physics Letters*, vol. 58, no. 24, pp. 2749-2751, 1991.
- [94] J. Vinchant, F. Mallecot, D. Ecocher, and J. Vilcot, "Photodetectors monolithically integrated with optical waveguides: Theoretical and experimental study of absorbing layer effects", *IEEE Proceedings, Part J*, vol. 136, p. 72, 1989.
- [95] M. Erman, P. Jarry, R. Gamonal, J. Gentner, P. Stephan, and C. Guedon, "Monolithic integration of a GaInAs p-i-n photodiode and out optical waveguide: Modeling and realisation using chloride vapour phase epitaxy", *Journal of Lightwave Technology*, vol. 6, no. 3, pp. 399-412, 1988.
- [96] R. Deri and et al., "Integrated waveguide photodiodes using vertical impedance matching", *Applied Physics Letters*, vol. 56, p. 1737, 1999.
- [97] R. Deri, E. Pennings, and R. Hawkins, "Quenching of resonantly enhanced absorption by multimode interference in vertically coupled waveguide photodetectors", *Optics Letters*, no. 9, pp. 667-669, 1992.
- [98] S. Kelso, D. Aspnes, M. Pollack, and R. Nahory, "Optical properties of $\text{In}_{1-x}\text{Ga}_x\text{As}_y\text{P}_{1-y}$ from 1.5 to 6.0 eV determined by spectroscopic ellipsometry", *Physical Review B*, p. 6669, 1982.

ACKNOWLEDGEMENT

First of all I would like to thank my supervisor Professor Dr. Hans Melchior for offering me the chance to work in this interesting field, for his support, his interest in my work and his readiness to let me learn things apart from physics.

I would also like to thank Professor Dr. P. Günter for his readiness to coexamine my thesis.

Dr. Emilio Gini who has grown my wafers and Dr. Werner Vogt for his countless tips concerning technology.

Dr. Christoph Holtmann and Martin Bitter who did all the evaporation processes for my devices.

Dr. Jürg Eckner, Hanspeter Schneibel and Dr. Eberhard Wildermuth for their cooperation and support solving cross-platform and networking problems, their compassion for a colleague from the PC Side and their friendship.

Dr. Christoph Nadler and Dr. Maurus Bachmann who first introduced me into the art of semiconductor technology and their cooperation later on.

Martin Ebnöter, Christoph Graph and Andreas Müller helped to solve all kinds of technical problems and rebellious machines I was responsible for. Thanks also deserve Veronica Bürgisser, Wendy Dekker and Paulette Pfammatter for handling all the administrative tasks.

Roger Krähenbühel, Markus Blaser, Christoph Holtmann for sharing the office with me in earlier times and for their watching over my biological experiments in my absence.

Last but not least I would also thank the other members of the IQE who made life in our institute pleasant. Especially Muriel Caraccia, Markus Dülk, Stefan Fischer, Ramón Guterrez-Castrejon, Lorenzo Occhi, Laurent Schares and all the others not mentioned above.

Special thanks go to my wife Eva who volunteered to proof read this thesis.

CURRICULUM VITAE

Name	Gerhard Hagn
Date of birth	7th February 1971
Place of birth	Bludenz, Republic of Austria
Nationality	Austria
1977–1981	Elementary school in Feldkirch
1981–1989	High school (Bundesgymnasium) in Feldkirch
June 1989	Matura
1989–1994	Study of Physics at the Swiss Federal Institute of Technology, Zürich
1994	Graduation at the Swiss Federal Institute of Technology with a diploma degree in Physics
1994–2000	Research and teaching assistant at the Federal Institute of Technology, Zürich. Ph.D. student at the Institute of Quantum Electronics ETH. Supervisors: Prof. Dr. H. Melchior and Prof. Dr. P. Günter.
December 2001	Ph.D. thesis and examination

LEBENS LAUF

Name	Gerhard Hagn
Geburtsdatum	7. Februar 1971
Geburtsort	Bludenz, Österreich
Nationalität	Österreich
1977-1981	Volksschule in Feldkirch
1981-1989	Bundesgymnasium in Feldkirch
Juni 1989	Matura
1989-1994	Studium der Physik an der Eidgenössisch Technischen Hochschule, Zürich
1994	Abschluss des Studiums mit dem Diplom in Physik
1994-2000	Assistent am Institut für Quantenelektronik an der Eidgenössisch Technischen Hochschule Zürich
1996-2000	Dissertation im Institut für Quantenelektronik Referenten: Prof. Dr. H. Melchior and Prof. Dr. P. Günter.
2000-	Systemspezialist im „Security Engineering“ der Credit-Suisse